Formulation Development of Anti-Cancer Drugs

By

Yunqi Zhao

Submitted to the graduate degree program in Pharmaceutical Chemistry and the Graduate Faculty of the University of Kansas in partial fulfillment of the requirements for the degree of Doctor of Philosophy.

_____

Chairperson M. Laird Forrest

_____

Cory J. Berkland

_____

Jeffrey P. Krise

_____

Zhuo Wang

_____

Xinmai Yang

Date Defended: December 18th, 2013

The Dissertation Committee for Yunqi Zhao

certifies that this is the approved version of the following dissertation:

Formulation Development of Anti-Cancer Drugs

_____

Chairperson M. Laird Forrest

Date approved:

Abstract

Formulation issues, including stability, solubility and bioavailability, have been identified as key concerns in anti-cancer drug development. The challenges in pharmaceutical formulation often arise from the different physicochemical attributes of a molecule and the need to deliver the compound to a desired site. The major problems of small molecule drug formulation development are poor water solubility and off target toxicity. In chapter 2 of this dissertation, a prostate specific membrane antigen (PSMA) targeted micelle was made to deliver a PI3K inhibitor, TGX-221, for prostate cancer treatment. The *in vitro* cell culture based study indicated that the targeted micelle significantly improved cellular uptake by PSMA positive cells. The *in vivo* animal efficacy study showed that the targeted micelle significantly reduced tumor size and progression in a xenograft model. Ridaforolimus, a non-prodrug rapamycin analog, has entered clinical trials for cancer treatment. Formulations of ridaforolimus being evaluated in the clinical trials include intravenous infusion and oral administration. The intravenous bolus formulation of this drug is very limited due to poor water solubility (ca. 200 µg/mL). In chapter 3, we showed that a new formulation of ridaforolimus using DSPE-PEG_{2000} micelle as a carrier greatly improved the drug solubility, increasing it 40 times. In addition, the pharmacokinetic properties examined in rats showed that this formulation significantly increased drug retention in the plasma. In chapter 4, a hyaluronic acid-rapamycin conjugate was synthesized and characterized. The disposition and efficacy of the drug conjugate were studied and demonstrated that the hyaluronic acid drug conjugate could be used for treating localized CD44 positive cancer. In chapter 5, a doxorubicin prodrug was developed for enhancing oral bioavailability. Doxorubicin was chemically conjugated with quercetin, a flavonoid, via a glycine linker. Quercetin is a P-

glycoprotein inhibitor; thus, it prevents doxorubicin efflux by this mechanism. The oral bioavailability of DOX was significantly improved in rats through this prodrug strategy. In the last chapter, an HPLC method was developed for the separation of active compounds from degraded alternol, which could be used for alternol manufacturing and stability studies.

Acknowledgements

I would like to extend my sincerest gratitude to my research advisor, Dr. M. Laird Forrest, for his education, support, patience, encouragement and friendship throughout my graduate study. His intellectual guidance and keen insight in creative research provided me with a solid foundation on which I will build my future scientific career. His mentorship was paramount in providing a well-rounded experience consistent with my long-term career goals. He provided me an excellent atmosphere for doing research and guided me to develop my own individuality. His technical and editorial advices were essential for completion of this dissertation.

My thanks also go to the members of my oral prelim and dissertation committee: Dr. M. Laird Forrest, Dr. Cory Berkland, Dr. Zhuo (Michael) Wang, Dr. Jeffery Krise, Dr. Teruna J. Siahaan, Dr. Sue M. Lunte and Dr. Xinmai Yang for their insightful comments and constructive criticisms at different stages of my graduate study. I appreciated their kindness to serve on this committee and their comments to improve this dissertation. I also would like to thank all faculty members in the Department of Pharmaceutical Chemistry for numerous discussions and lectures that helped me improving my knowledge in the area and holding me to a high research standard.

I would like to thank all my current labmates: Dr. Shuang Cai, Qiuhong Yang, Ti Zhang, Ryan Moulder and previous lab members: Dr. Shaofeng Duan, Dr. Yumei Xie and Dr. Taryn Bagby for their assistance in the lab and understanding throughout my graduate study. Also, I give many thanks to all the collaborators and friends: Dr. Benyi Li, Dr. Neal Davies, Xing Zeng and Casey Sayre for their support with the collaborative researches.

Additionally, I would like to thank Dr. Valentino Stella, Dr. John Stobaugh, Dr. Russell Middaugh, Dr. Christian Schoneich, Dr. Jennifer Laurence, Dr. Stevin Gehrke, Dr. Richard Givens and Dr. Michael Rubin for being such wonderful and responsible teachers.

Last, but not the least, I want my parents and my grandparents to receive my deepest gratitude for their education, dedication, encouragement and endless love in the whole of the past twenty years. Their excellence in career and the pursuit of perfection have been the driving forces of my motivation to be better. Their pride and happiness make this dissertation meaningful.

Yunqi Zhao

December, 2013

Table of Contents

Chapter 1

Formulation Development of Anti-Cancer Drugs

Cancer is a major public health problem in the United States and other countries (1-4). One in four deaths in the United States is due to cancer (5), with lung, stomach, liver, colon and breast cancers contributing the most (GLOBOCAN, 2008). In 2012, a total of 1,660,290 new cancer cases and 580, 350 cancer deaths were projected in the United States (Cancer Statistics, 2013). Compared to 1991, the risk of cancer death in America has decreased by 20 % (6). Two out of three people diagnosed with cancer today in the US survive at least 5 years (American Cancer Society, 2013). However, the deaths from cancer worldwide are estimated to continue rising with a projected 14.1 million deaths in 2030. About 70 % of all cancer deaths in 2008 occurred in low- and middle-income countries (WHO, 2013).

Chemotherapy is an integral component of treatment for most cancers, and it is often combined with surgery, radiation and hormone therapy (7, 8). Even though cancer is no longer considered an incurable disease, the treatments for many cancers often fail due to the adverse side-effects of treatment or inconsistent outcomes from the drugs (9, 10).

Improved formulation development has emerged as a potential avenue for improving the efficacy and safety of chemotherapy (11, 12). The development of new vehicles and drug formulations could enhance drug delivery to the target tissue while minimizing side effects and increasing patient compliance (13). There are at least four known physiological and biological barriers for anti-neoplastic drug delivery. The first barrier is the heterogeneous angiogenesis in tumor tissues (14). Normal cells cannot live if they lack adequate nutrition and oxygen. The dysregulation of angiogenesis in tumor tissue induces heterogeneous blood flow in different regions within the tumor. At the early stages of tumor growth, there are some regions of high blood flow to the tumor for

nutrition transport. However, at advanced stages, increasing areas of the tumor have very little or no blood flow resulting in poor penetration of the anticancer drug (15). The second barrier is the tremendous spatial and temporal heterogeneity permeability of tumor vessels (16). The connections between the tumor cells and the adjacent perivascular/endothelial cells are tightly associated; thus, the vascular permeability of the drug is dramatically reduced (17). The third barrier of anti-cancer drug delivery is the interstitial compartment (18). Larger molecule tends to penetrate through the interstitium slowly, and the movement of the drug in this compartment is driven by diffusion and convection. Furthermore, the remarkably high interstitial tumor pressure results in rapid removal of drugs from tumor extracellular space. The fourth barrier is the cell membrane and the cytoplasm. Many macromolecules and charged compounds are poorly absorbed due to poor partitioning properties. For oral drug delivery, the high acidity in the stomach and the enzymes in digestive tract contribute an additional barrier to systemic absorption (19). Most protein and peptide drugs are degraded in the gastrointestinal compartment before they enter the bloodstream.

Nanoparticles used as drug delivery systems exhibit unique physical, optical, electronic and useful biological properties that can be very helpful for cancer treatment (20). During the last two decades, scores of nanoparticle delivery systems have been developed for chemotherapy, such as lipid-based nanoparticles (21, 22), polymer-based nanoparticles (23, 24), metal-based nanoparticles (25, 26) and biological nanoparticles (27, 28). Nanotechnology has been intensively studied as a novel vector for tumor directed drug delivery.

Nanoparticle formulations have the potential to improve the therapeutic efficacy of anticancer agents, change the pharmacokinetic properties of the compound by their enhanced permeability and retention (EPR) effect (29), alter protein binding and increase plasma retention. The tumor tissue has leaky vasculature and lack of lymphatic drainage (30). Nanoparticles smaller than 200 nm (for extravasculation) (31) and larger than 10 nm (to avoid renal clearance) (32) tend to accumulate in the tumor site and reduce non-specific drug distribution to normal organs. The biggest challenge of passive tumor targeting is the inability to achieve a sufficiently high level of drug concentration at the target spot resulting in low therapeutic efficacy and eliciting undesirable systemic adverse effects. In comparison, active tumor targeting can be achieved by conjugating target molecules to the surface of particles. The targeting moieties can recognize and bind to specific ligands that are expressed uniquely on the cancer cell's surface (33). The combination of active targeting with nanoparticles is particularly useful for the treatment of primary tumors that have not yet metastasized. Molecules can be used for the development of targeted nanoparticles including monoclonal antibodies (34), aptamers (35), oligopeptides (36) and small molecules, such as folate (37).

Nanoparticle technology has several potential benefits over traditional small molecule formulation. Firstly, the aqueous solubility of the drug can be significantly improved (38, 39). For poorly water soluble compounds, the dissolution velocity is the rate limiting step for drug absorption, which is one of the leading causes of low oral bioavailability. Based on the Noyes-Whitney equation, which describes the dissolution rate of the drug in a diffusion controlled process, the dissolution velocity of the drug can be improved by increasing the surface area. Secondly, the particles can deliver the drug molecules specifically to the target site in a sustained and controlled manner (40). The

nanoparticle formulation can prolong drug circulation time, enhance the therapeutic index and decrease drug toxicity. Therefore, a reduction in frequency and dosing is possible during treatment.

Polymeric micelles are spontaneously formed from amphiphilic polymers in aqueous media. The hydrodynamic diameters of the micelles are in the range of 20 – 80 nm. The driving force is the disruption of water molecule by the hydrophobic blocks. A small diffusion coefficient, as low as 10^{-16} to 10^{-18} cm^2/sec, is required for sustained and controlled release of the drug from micelle particles (41). Micelle formulations have been intensively studied for hydrophobic drug delivery. One example of a micelle formulation of doxorubicin that entered a phase II clinical trial is SP1049C. The micelle matrix of SP1049C consists of Pluronic® L61 and F127 (1:8 w/w). After injection, the $t_{1/2}$ of SP1049C was 50 h, which is longer than the doxorubicin alone ($t_{1/2}$ = 30 h) (42).

Poly(ethylene glycol) (PEG) is a bio-compatible and bio-degradable synthetic polymer approved by the FDA for internal use. PEG is widely used in the shell forming block of the micelle. The high hydration and rapid motion properties of PEG prevent particle interaction with proteins and mononuclear phagocytic system clearance in the blood stream. Ishihara et al. studied the biodistribution of a PEGylated polymeric nanoparticle in mice (43). They demonstrated that compared to the conventional nanoparticle, the PEGylated particle significantly prolonged body circulation time and enhanced drug accumulation at the target site. In addition, the functionalized PEG end could be used for conjugating a targeting moiety onto the micelle's surface. Active targeting of the micelles can be achieved by this approach. Farokhzad et al. formulated a prostate specific membrane antigen targeted PEGylated nanoparticle for the delivery of

docetaxel (44). After a single injection of the formulation, complete tumor reduction was observed in 5 out of 7 mice, and 100 % animal survival was achieved.

The toxicity and side effects of an anti-cancer agent can be reduced as well through a micelle formulation. This is due to the minimization of non-specific tissue binding of the drug. For example, in a preclinical study, PEG-b-poly(L-lactic acid) micelles increased the maximum tolerable dose of paclitaxel from 20 to 100 mg/kg after intraperitoneal administration in mice (45).

The core of a polymeric micelle is made of a hydrophobic block of the amphiphilic copolymer. This is the primary site of residence for the hydrophobic drug. The hydrophobic block governs the capacity of a micelle's solubilization. Therefore, a key optimization factor in micelle formulation is the compatibility of the molecule with the hydrophobic core (46). The compatibility is related to the structural and polar similarities between the drug and hydrophobic block of the amphiphilic copolymer. The goal is to minimize the Flory-Huggins interaction parameter between the poorly water soluble drug and the core-forming hydrophobic block. The minimization of Flory-Huggins parameter presents the ideal situation for drug solubilization. The polymer used as drug delivery carrier should be biocompatible and biodegradable (47). The commonly used polymers for micelle cores are poly(esters), such as poly(lactic acid), poly(lactic-co-glycolic acid) and poly(caprolactone); phospholipid.

Over the past decade, polymer-drug conjugates with a variety of structures and chemical properties have been investigated in the clinic (48), and there are more than 10 polymer-anticancer drug conjugates currently under clinical trials. The ongoing clinical trials of polymer drug conjugates includes HMPA copolymer-doxorubicin (PK1),

PEG-poly(aspartic acid)-doxorubicin (NK 911), poly L-glutamic acid-paclitaxel (Xyotax), HMPA copolymer-platinate (AP5346), PEG-camptothecin and PEG-SN38 (49). Pharmacokinetics and bio-distribution of a drug could be changed through chemical conjugation with a highly functionalized polymer molecule (50). However, the toxicities differed in the polymer drug conjugate model, not only are drugs attached to the polymeric carriers, but a targeting moiety is also introduced to the same polymeric carrier to achieve specific targeting (51). The advantages of polymer drug conjugates over their parent drugs includes fewer side effects, improved efficacy and toxicity of the therapeutic agents, increased patient compliance and ease of drug administration. For instance, the clinical safety dose of N-(2-hydroxypropyl) methacrylamide (HPMA) copolymer-doxorubicin conjugate (FCE28068) is approximately 4 - 5 folds higher than doxorubicin hydrochloride solution (52). By administration of HPMA-doxorubicin conjugate containing galactosamine (FCE28068), which presents extra-hepatic galactose receptors, doxorubicin concentration in hepatoma tissue was 12-50 folds higher than the free drug and the maximum tolerate dose was significantly lower than FCE28068(53).

Examples of therapeutic nanoparticle formulations of anti-cancer drugs in clinics and under clinical evaluations are summarized in Table 1.

Table 1: Nanoparticle formulations of anticancer drugs in clinic or under clinical evaluations.

Name	Description	Phase
Doxil®/Caelyx®	Liposome formulation of doxorubicin	FDA approved
PK1 (FCE 28068)	Doxorubicin-HPMA polymer conjugate	Phase II
PK2 (FCE28069)	Doxorubicin-HPMA polymer conjugate with galactosamine	Phase II
Abraxane®	Albumin-bound paclitaxel	FDA approved
NK105	Micelle formulation of paclitaxel (mPEG-polyaspartate)	Phase III
Genexol-PM®	Micelle formulation of paclitaxel (mPEG-PDLLA)	FDA approved
Xyotax®	Paclitaxel-poly L-glutamic acid conjugate	Phase IV
NC-6004	Polymeric micelle of cisplatin (PEG-poly amino acid)	Phase II
Lupron Depot®	GnRH loaded PLGA nanoparticle	FDA approved
CALAA-01	Targeted nanoparticle with the combination of RONDEL^{TM} and a patented siRNA	Phase I

A prodrug is a medication that is an inactive bioreversible derivative form of a drug molecule (54). Prodrugs undergo enzymatic and/or chemical transformation to release the active parent drug in the body. Depending on where the body converts the prodrug back to its active form determines their classification. Prodrugs can be classified into two types. The type I prodrugs are bioactivated inside the cells, such as anti-viral nucleoside analogs. Type I prodrugs that have been tested in clinical trials include: acyclovir, 5-fluorouracil, carbamazepine, captopril, heroin, psilocybin, etc. Type II prodrugs are activated outside the cells, especially in digestive fluids or in the body's circulation system (55). Commercially available type II prodrugs include: lisdexamfetamine, loperamide oxide, oxyphenisatin, bambuterol, acetylsalicylate and fosphenytoin. Using a prodrug strategy, site-specific drug delivery for cancer treatment can be achieved.

The strategy of using enzyme activated prodrugs has been widely used in cancer treatment (56). Prodrugs can be selectively activated in tumor tissues by exogenous enzymes followed by systemic administration. These directed enzyme prodrug therapies include gene-directed enzyme prodrug therapy (GDEPT) (57), virus-directed enzyme prodrug therapy (VDEPT) (58), antibody-directed enzyme prodrug therapy (ADEPT) (59), polymer-directed enzyme prodrug therapy (PDEPT) and clostridia-directed enzyme prodrug therapy (CDEPT).

In this dissertation, different formulations of several potent anticancer agents were developed. Pharmacokinetics, tissue distribution and efficacy of the formulated anticancer drugs showed significant improvement in treated animals. These

investigations could have a significant impact on cancer treatment and address a critical need in the field of cancer research and/or patient care.

References

1. J.L. Kelsey. A review of the epidemiology of human breast cancer. Epidemiologic reviews. 1:74-109 (1979).
2. A. Natori, N. Hayashi, K. Soejima, G.A. Deshpande, O. Takahashi, M. Cristofanilli, N.T. Ueno, and H. Yamauchi. A Comparison of Epidemiology, Biology, and Prognosis of Inflammatory Breast Cancer in Japanese and US Populations. Clinical breast cancer(2013).
3. C.H. Chung, A. Bagheri, and G. D'Souza. Epidemiology of oral human papillomavirus infection. Oral oncology(2013).
4. E.M. Sturgis. International Head and Neck Cancer Epidemiology Consortium: Update no. 12. Head & neck. 35:1371-1372 (2013).
5. J.L. Cresanta. Epidemiology of cancer in the United States. Primary care. 19:419-441 (1992).
6. R. Siegel, D. Naishadham, and A. Jemal. Cancer statistics, 2013. CA: a cancer journal for clinicians. 63:11-30 (2013).
7. F.Z. Chenand X.K. Zhao. Prostate Cancer: Current Treatment and Prevention Strategies. Iranian Red Crescent medical journal. 15:279-284 (2013).
8. A. Mohanand S. Ponnusankar. Newer Therapies for the Treatment of Metastatic Breast Cancer: a Clinical Update. Indian journal of pharmaceutical sciences. 75:251-261 (2013).

9. D. Stindtand M.J. Brown. Chemotherapy-Induced mucositis. Advance for NPs & PAs. 4:27-28 (2013).

10. M.T. Fallon. Neuropathic pain in cancer. British journal of anaesthesia. 111:105-111 (2013).

11. Y. Luoand G.D. Prestwich. Cancer-targeted polymeric drugs. Current cancer drug targets. 2:209-226 (2002).

12. Y. Tomii. Lipid formulation as a drug carrier for drug delivery. Current pharmaceutical design. 8:467-474 (2002).

13. D. Ghateand H.F. Edelhauser. Barriers to glaucoma drug delivery. Journal of glaucoma. 17:147-156 (2008).

14. C. Milsomand J. Rak. Tissue factor and cancer. Pathophysiology of haemostasis and thrombosis. 36:160-176 (2008).

15. K. Hori, M. Suzuki, S. Tanda, S. Saito, and Q. Zhang. Functional-characterization of developing tumor vascular system and drug delivery (review). International journal of oncology. 2:289-296 (1993).

16. D. Ribatti. Vascular normalization: a real benefit? Cancer chemotherapy and pharmacology. 68:275-278 (2011).

17. S. Goel, D.G. Duda, L. Xu, L.L. Munn, Y. Boucher, D. Fukumura, and R.K. Jain. Normalization of the vasculature for treatment of cancer and other diseases. Physiological reviews. 91:1071-1121 (2011).

18. V.P. Chauhan, T. Stylianopoulos, Y. Boucher, and R.K. Jain. Delivery of molecular and nanoscale medicine to tumors: transport barriers and strategies. Annual review of chemical and biomolecular engineering. 2:281-298 (2011).

19. R.M. Reilly, R. Domingo, and J. Sandhu. Oral delivery of antibodies. Future pharmacokinetic trends. Clinical pharmacokinetics. 32:313-323 (1997).
20. G. Zhang, X. Zeng, and P. Li. Nanomaterials in cancer-therapy drug delivery system. Journal of biomedical nanotechnology. 9:741-750 (2013).
21. S. Tan, X. Li, Y. Guo, and Z. Zhang. Lipid-enveloped hybrid nanoparticles for drug delivery. Nanoscale. 5:860-872 (2013).
22. J.L. Arias, B. Clares, M.E. Morales, V. Gallardo, and M.A. Ruiz. Lipid-based drug delivery systems for cancer treatment. Current drug targets. 12:1151-1165 (2011).
23. P. Caoand Y. Bae. Polymer nanoparticulate drug delivery and combination cancer therapy. Future oncology. 8:1471-1480 (2012).
24. M. Stanczyk, A. Dziki, and Z. Morawiec. Dendrimers in therapy for breast and colorectal cancer. Current medicinal chemistry. 19:4896-4902 (2012).
25. S. Akhter, M.Z. Ahmad, F.J. Ahmad, G. Storm, and R.J. Kok. Gold nanoparticles in theranostic oncology: current state-of-the-art. Expert opinion on drug delivery. 9:1225-1243 (2012).
26. J. Klostergaardand C.E. Seeney. Magnetic nanovectors for drug delivery. Maturitas. 73:33-44 (2012).
27. D. Koppers-Lalic, M.M. Hogenboom, J.M. Middeldorp, and D.M. Pegtel. Virus-modified exosomes for targeted RNA delivery; a new approach in nanomedicine. Advanced drug delivery reviews. 65:348-356 (2013).
28. M. Foldvari. HPV infections: can they be eradicated using nanotechnology? Nanomedicine : nanotechnology, biology, and medicine. 8:131-135 (2012).

29. H. Maeda, H. Nakamura, and J. Fang. The EPR effect for macromolecular drug delivery to solid tumors: Improvement of tumor uptake, lowering of systemic toxicity, and distinct tumor imaging in vivo. Advanced drug delivery reviews. 65:71-79 (2013).

30. S.R. MacEwan, D.J. Callahan, and A. Chilkoti. Stimulus-responsive macromolecules and nanoparticles for cancer drug delivery. Nanomedicine (Lond). 5:793-806 (2010).

31. L. Illum, S.S. Davis, C.G. Wilson, N.W. Thomas, M. Frier, and J.G. Hardy. Blood Clearance and Organ Deposition of Intravenously Administered Colloidal Particles - the Effects of Particle-Size, Nature and Shape. International journal of pharmaceutics. 12:135-146 (1982).

32. S.V. Vinogradov, T.K. Bronich, and A.V. Kabanov. Nanosized cationic hydrogels for drug delivery: preparation, properties and interactions with cells. Advanced drug delivery reviews. 54:135-147 (2002).

33. S. Hirsjarvi, C. Passirani, and J.P. Benoit. Passive and active tumour targeting with nanocarriers. Current drug discovery technologies. 8:188-196 (2011).

34. M.M. Cardoso, I.N. Peca, and A.C. Roque. Antibody-conjugated nanoparticles for therapeutic applications. Current medicinal chemistry. 19:3103-3127 (2012).

35. A.S. Barbas, J. Mi, B.M. Clary, and R.R. White. Aptamer applications for targeted cancer therapy. Future oncology. 6:1117-1126 (2010).

36. E. Garanger, D. Boturyn, and P. Dumy. Tumor targeting with RGD peptide ligands-design of new molecular conjugates for imaging and therapy of cancers. Anti-cancer agents in medicinal chemistry. 7:552-558 (2007).

37. L. Juillerat-Jeanneretand F. Schmitt. Chemical modification of therapeutic drugs or drug vector systems to achieve targeted therapy: looking for the grail. Medicinal research reviews. 27:574-590 (2007).

38. L. Zhangand N. Zhang. How nanotechnology can enhance docetaxel therapy. International journal of nanomedicine. 8:2927-2941 (2013).

39. P.H. Tran, T.T. Tran, and B.J. Lee. Enhanced solubility and modified release of poorly water-soluble drugs via self-assembled gelatin-oleic acid nanoparticles. International journal of pharmaceutics. 455:235-240 (2013).

40. W. Huang, J. Zhang, H.C. Dorn, and C. Zhang. Assembly of bio-nanoparticles for double controlled drug release. PloS one. 8:e74679 (2013).

41. Y. Teng, M.E. Morrison, P. Munk, S.E. Webber, and K. Prochazka. Release kinetics studies of aromatic molecules into water from block polymer micelles. Macromolecules. 31:3578-3587 (1998).

42. S. Danson, D. Ferry, V. Alakhov, J. Margison, D. Kerr, D. Jowle, M. Brampton, G. Halbert, and M. Ranson. Phase I dose escalation and pharmacokinetic study of pluronic polymer-bound doxorubicin (SP1049C) in patients with advanced cancer. British journal of cancer. 90:2085-2091 (2004).

43. T. Ishihara, T. Kubota, T. Choi, and M. Higaki. Treatment of experimental arthritis with stealth-type polymeric nanoparticles encapsulating betamethasone phosphate. The Journal of pharmacology and experimental therapeutics. 329:412-417 (2009).

44. O.C. Farokhzad, J. Cheng, B.A. Teply, I. Sherifi, S. Jon, P.W. Kantoff, J.P. Richie, and R. Langer. Targeted nanoparticle-aptamer bioconjugates for cancer

chemotherapy in vivo. Proceedings of the National Academy of Sciences of the United States of America. 103:6315-6320 (2006).

45. X. Zhang, H.M. Burt, D. Von Hoff, D. Dexter, G. Mangold, D. Degen, A.M. Oktaba, and W.L. Hunter. An investigation of the antitumour activity and biodistribution of polymeric micellar paclitaxel. Cancer chemotherapy and pharmacology. 40:81-86 (1997).

46. R. Nagarajan, M. Barry, and E. Ruckenstein. Unusual Selectivity in Solubilization by Block Copolymer Micelles. Langmuir. 2:210-215 (1986).

47. Y. Yang, D. Pan, K. Luo, L. Li, and Z. Gu. Biodegradable and amphiphilic block copolymer-doxorubicin conjugate as polymeric nanoscale drug delivery vehicle for breast cancer therapy. Biomaterials. 34:8430-8443 (2013).

48. X. Pang, H.L. Du, H.Q. Zhang, Y.J. Zhai, and G.X. Zhai. Polymer-drug conjugates: present state of play and future perspectives. Drug discovery today(2013).

49. C. Liand S. Wallace. Polymer-drug conjugates: Recent development in clinical oncology. Advanced drug delivery reviews. 60:886-898 (2008).

50. R. Duncanand F. Spreafico. Polymer conjugates. Pharmacokinetic considerations for design and development. Clinical pharmacokinetics. 27:290-306 (1994).

51. H. Sezakiand M. Hashida. Macromolecule-drug conjugates in targeted cancer chemotherapy. Critical reviews in therapeutic drug carrier systems. 1:1-38 (1984).

52. L.W. Seymour, D.R. Ferry, D.J. Kerr, D. Rea, M. Whitlock, R. Poyner, C. Boivin, S. Hesslewood, C. Twelves, R. Blackie, A. Schatzlein, D. Jodrell, D. Bissett, H. Calvert, M. Lind, A. Robbins, S. Burtles, R. Duncan, and J. Cassidy. Phase II

studies of polymer-doxorubicin (PK1, FCE28068) in the treatment of breast, lung and colorectal cancer. International journal of oncology. 34:1629-1636 (2009).

53. R. Duncan. The dawning era of polymer therapeutics. Nature reviews Drug discovery. 2:347-360 (2003).

54. E. De Clercqand H.J. Field. Antiviral prodrugs - the development of successful prodrug strategies for antiviral chemotherapy. British journal of pharmacology. 147:1-11 (2006).

55. K.-M. Wu. A New Classification of Prodrugs: Regulatory Perspectives. Pharmaceuticals. 2:5 (2009).

56. K. Sharma, K. Sengupta, and H. Chakrapani. Nitroreductase-activated nitric oxide (NO) prodrugs. Bioorganic & medicinal chemistry letters(2013).

57. L.K. Green, S.P. Syddall, K.M. Carlin, G.D. Bell, C.P. Guise, A.M. Mowday, M.P. Hay, J.B. Smaill, A.V. Patterson, and D.F. Ackerley. Pseudomonas aeruginosa NfsB and nitro-CBI-DEI--a promising enzyme/prodrug combination for gene directed enzyme prodrug therapy. Molecular cancer. 12:58 (2013).

58. R.J. Knox, P.J. Burke, S. Chen, and D.J. Kerr. CB 1954: from the Walker tumor to NQO2 and VDEPT. Current pharmaceutical design. 9:2091-2104 (2003).

59. R.J. Francis, S.K. Sharma, C. Springer, A.J. Green, L.D. Hope-Stone, L. Sena, J. Martin, K.L. Adamson, A. Robbins, L. Gumbrell, D. O'Malley, E. Tsiompanou, H. Shahbakhti, S. Webley, D. Hochhauser, A.J. Hilson, D. Blakey, and R.H. Begent. A phase I trial of antibody directed enzyme prodrug therapy (ADEPT) in patients with advanced colorectal carcinoma or other CEA producing tumours. British journal of cancer. 87:600-607 (2002).

Chapter 2

Localized Prostate Cancer Treatment Using PI3K Inhibitor Loaded PSMA-Targeted Nanoparticles

2.1 Introduction

The phosphatidylinositol 3-kinase (PI3K)/ phosphatase and tensin homolog (PTEN)/Akt pathway is highly involved in different types of cancer (1). PI3Ks are a family of enzymes that phosphorylate PI(4,5)P2 (PIP2) to PI(3,4,5)P3 (PIP3). PIP3 is a lipid-signaling second messenger that further activates its downstream effectors, such as Akt, PDK1 and Rac1/cdc42 (2). The activation of Akt stimulates cell growth, proliferation and survival (3). PTEN is a phosphatase that dephosphorylates PIP3 back to PIP2 (4). The missing function of PTEN results in accumulation of PIP3, which mimics the over activation of PI3K and triggers cell growth. PTEN deficiency is found in many types of cancers, such as prostate cancer (LNCaP), brain cancer (U87MG) and breast cancer (BT549) (5-7).

There are three classes of PI3K isoforms. The most commonly studied class I PI3Ks are further divided into classes IA and IB. Only class IA enzymes are clearly implicated in human cancers. Class IA PI3K enzymes consist of a p110 catalytic subunit and a regulatory subunit. There are three highly homologous p110 catalytic isoforms: p110alpha, p110beta and p110delta (8, 9). p110beta is a promising target in cancer therapy (10, 11) and PTEN-deficient tumor cells mainly depend on p110beta for signaling and growth, not p110alpha (9).

The synthetic small molecule TGX-221 (Fig. 1) is a potent, selective and cell membrane permeable inhibitor of PI3K p110 beta catalytic subunit, which is critical for cell growth, proliferation and tumorigenesis of PTEN-deficient tumor cells including prostate cancers (12, 13). Therefore, PI3K p110 beta inhibitors have a great promise as novel chemotherapeutic agents to treat PTEN deficient cancer cells (13). However,

TGX-221 is poorly soluble and requires organic solvents, such as DMSO or propylene glycol, for intravenous injection, which may cause cardiac toxicity, unconsciousness, arrhythmia and cardiac arrest (14).

The therapeutic index of anticancer drugs is often very narrow, and the cytotoxic dose of the drug in the desired tissues can be maintained over an extended period of time with minimal side effects by targeted delivery and controlled drug release (15, 16). Both passive and ligand-targeted nanoparticles have been developed for targeted delivery of cancer therapies (17, 18). Passively targeted nanoparticles can accumulate to a greater extent in tumors compared to healthy tissues due to the enhanced permeability and retention (EPR) effect. The high accumulation of nanoparticles in the tumor tissues is a consequence of the poorly aligned endothelial cells allowing nanoparticles to escape from the blood circulatory system and to pool in the tumor where there is a lack of effective lymphatic drainage (19, 20). Micelles are attractive nanoparticles for the delivery of hydrophobic drugs, since they form spontaneously in water after co-mixing the drug with an amphiphilic polymer. Both polyethylene glycol (PEG) and polycaprolactone (PCL) are FDA approved biocompatible and biodegradable materials. Micelles formed by PEG-PCL block copolymers have been used as an effective drug delivery system for lipophilic molecules (21-23). Upon pooling in the tumor, micelles will slowly release the drug and then dissolve into non-toxic degradation products (24).

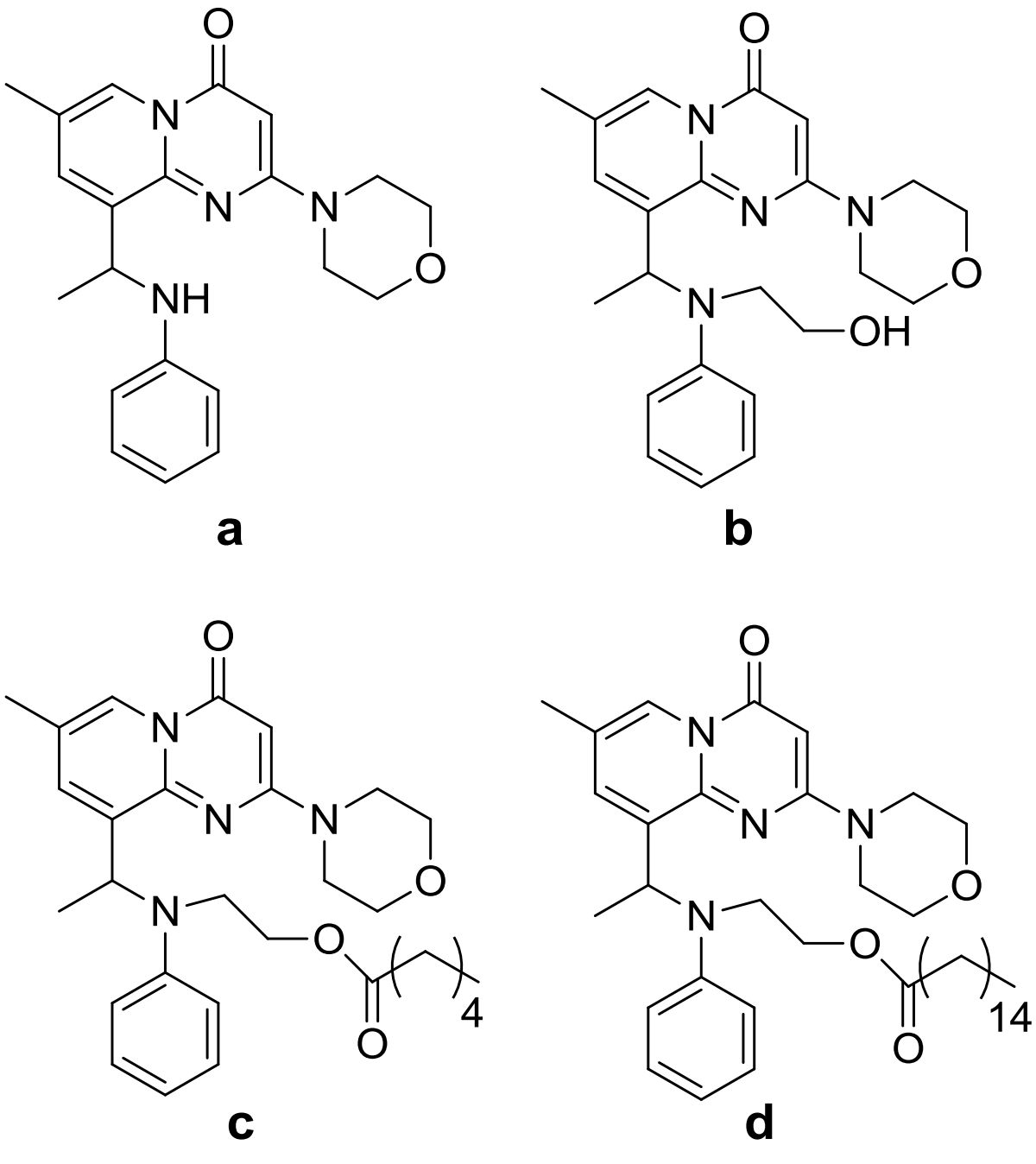

Fig. 1: Structure of (a) TGX-221; (b) BL05; (c) BL05-HA and (d) BL05-PA.

Nanoparticles actively targeted via ligand binding can target cancer cells that over express specific receptors or proteins (16). The ligands, monoclonal antibodies or aptamers, can recognize and bind to complementary molecules expressed on the tumor cells. We hypothesized that the delivery of a TGX-221 analogue to prostate cancer cells may be improved if the drug is encapsulated in targeted-nanoparticles. The cancer-targeted nanoparticles should be effective in suppressing tumor growth and metastasis with reduced or lack of side effects associated with drug toxicities to normal tissues.

Aptamers are single- or double-stranded oligonucleotides that are modified to have high binding affinity and specificity to their targets (25), and they have emerged as a novel class of active targeting moieties for therapeutic and diagnostic applications in cancer treatment. Prostate specific membrane antigen (PSMA) expression is confined primarily to prostate tissues (26, 27). The expression of PSMA in other tissues, such as the brain and small intestines, is approximately 1,000-fold less than that in the prostate (28). Prostate specific membrane aptamer A10 (PSMAa10) has nM affinity to the membrane expressing PSMA, and it can be used to achieve specific targeting of the nanoparticles to prostate cancer cells (29).

Due to the high biocompatibility of PEG-PCL block copolymers and the specific expression of PSMA on prostate cancer cells, the combination of PEG-PCL and PSMAa10 in a nanoparticle delivery system is promising for the targeted therapy of prostate cancer.

2.2 Materials and Methods

2.2.1 Materials

Azide poly(ethylene glycol) (MW: 5,800) was purchased from Polymer Source Inc. (Quebec, Canada). Propargyl-dPEG®1-NHS ester was purchased from Quanta BioDesign Ltd. (Powell, Ohio). PSMAa10 { 5'-[NH_2-$(CH_2)_6$-PEG_{18}-GGG AGG ACG AUG GGG AUC AGC CAU GUU UAC GUC ACU CCU UGU CAA UCC UCA UCG GC *inverted* T]-3', 2'F pyrimidines } was custom synthesized by Integrated DNA Technologies (Coralville, IA). ε-caprolactone, IR-820, pyrene, 1-amino-3-butyne and 1-M HCl in diethyl-ether were purchased from Sigma-Aldrich Co. (St. Louis, MO). Resazurin blue, silica gel and the organic solvents were purchased from Fisher Scientific (Pittsburgh, PA).

2.2.2 TGX-221 and prodrug synthesis

All chemicals were used as received unless stated otherwise. NMR spectra were taken on a 400-MHz Bruker with the solvent peak as an internal reference. Mass spectra were run in the Electrospray Ionization Mass Spectrometry (*ESI-MS*) mode or Atmospheric Pressure Chemical Ionization Mass Spectrometry (*APCI-MS*) mode. Reactions that required an inert atmosphere were carried out under dry argon with flame-dried glassware. Tetrahydrofuran (THF) was freshly distilled over sodium-benzophenone. Dichloromethane (DCM), N, N-dimethylformaldehyde (DMF) and triethylamine (TEA) were freshly distilled over CaH_2. The synthetic scheme of TGX-221 and its analog BL05 are shown in Scheme 1.

Synthesis of compound 1. Malonyl dichloride (3.2 mL, 32.0 mmol) was added dropwise to a solution of 2-amino-3-bromo-5-methylpyridine (5 g, 26.7 mmol) in

dry DCM (50 mL) cooled to 0 ^{o}C. The mixture was stirred at ambient temperature (ca. 22 ^{o}C) for 48 h. The yellow precipitate was collected by filtration, washed with DCM (3 x 50mL), and dried under reduced pressure. The desired compound was obtained with a yield of 86 % (4.88 g), and identity was confirmed by ^{1}H-NMR. The crude compound was used in the next step without any further purification. The filtrate was concentrated by rotary evaporator. The resulting residue was suspended in 100 mL of H_2O, and the suspension was stirred at ambient temperature for 1 h. The suspension was filtered and the filtrate was neutralized with solid Na_2CO_3 to recover the unreacted 2-amino-3-bromo-5-methylpyridine (0.84 g).

Synthesis of compound 2. Compound 1 (4.88 g, 19.13 mmol) was suspended in dry DCM (100 mL), and TEA (5.40 mL, 38.3 mmol) was added dropwise at 0 ^{o}C followed by methanesulfonyl chloride (MsCl) (2.90 mL, 26.8 mmol). The mixture was stirred at ambient temperature for 1 h. Morpholine (5.0 mL, 57.4 mmol) was added and the mixture was refluxed for 24 h. The solvent then was removed under reduced pressure, and the mixture was diluted with H_2O to afford a pale yellow precipitate. The solid was collected by filtration, washed with 2 x 50 mL of H_2O, and dried under reduced pressure. The residue was purified through a silica flash column using EtOAc: hexanes 3:1 as the eluting solvent. The desired compound was obtained as a yellow solid with a yield of 42 % (2.61 g).

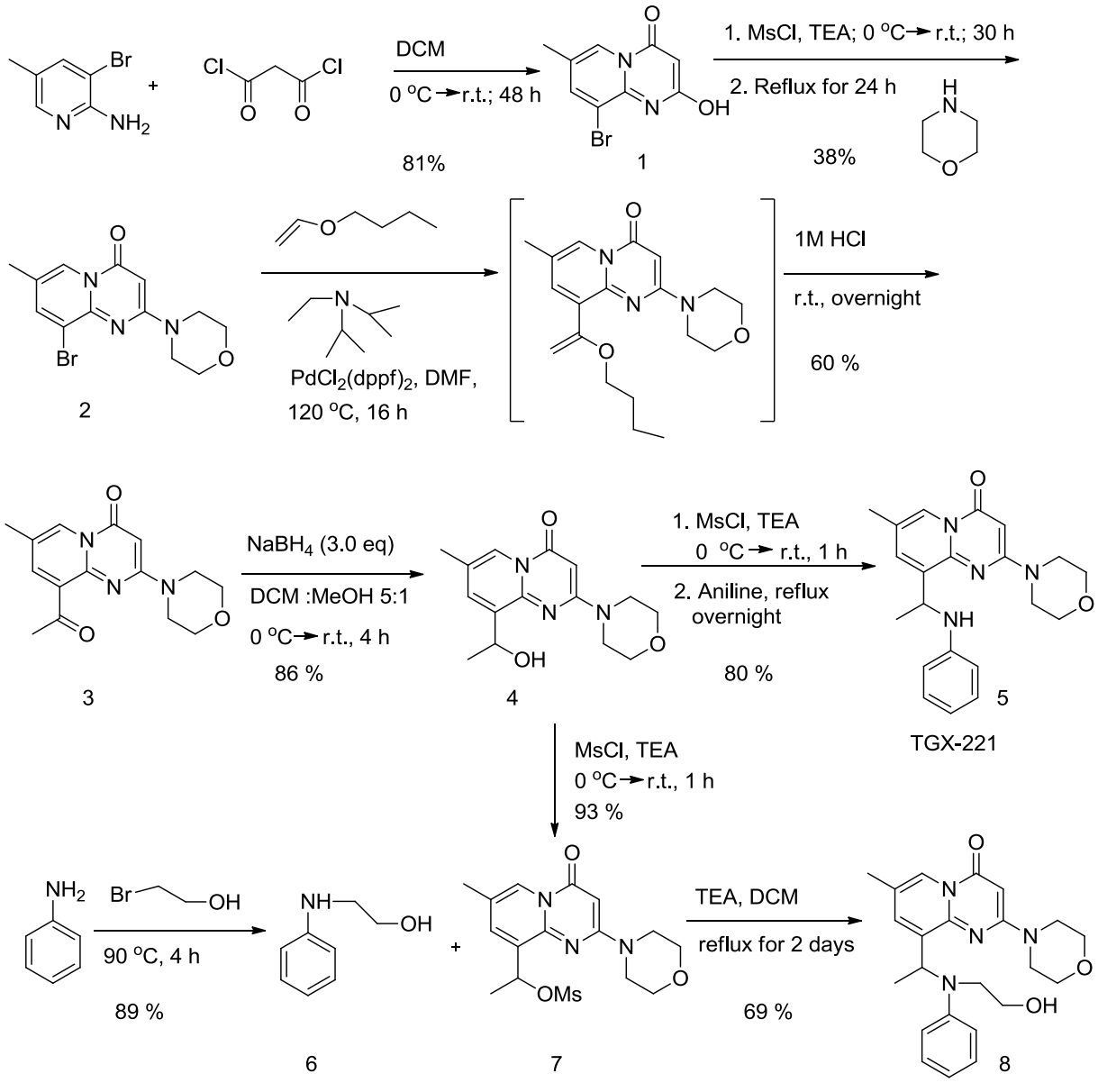

Scheme 1: Synthesis of TGX-221 (Compound 5) and BL05 (Compound 8).

Synthesis of compound 3. Compound 2 (2.53 g, 7.80 mmol) in dry DMF (50 mL) was mixed with N, N-diisopropylethylamine (4.0 mL), butyl vinyl ether (5.0 mL) and dichloro 1,1'-bis(diphenylphosphino)ferrocene palladium (II) (0.25 g, 0.20 mmol) at ambient temperature under argon for ca. 30 min until a homogeneous solution was formed. The solution then was heated to 120 ^{o}C and stirred for another 16 h. After the solution cooled, it was poured into 200 mL of 1-M HCl at 0 ^{o}C. The mixture then was stirred at ambient temperature overnight and extracted with DCM (2 x 100 mL). The combined organic phases were washed with water and dried over Na_2SO_4. Removal of the solvent under reduced pressure followed by purification of the resulting residue through a silica flash column using EtOAc: hexanes 3:1 as the eluting solvent led to the desired compound with a yield of 60 % (1.35 g).

Synthesis of compound 4. Compound 3 (1.35 g, 4.69 mmol) in DCM and methanol (5 : 1, 84 mL) was combined with $NaBH_4$ (0.70 g, 18.5 mmol) in 5 portions at 0 ^{o}C . After 10 min, the cooling bath was removed and the mixture was stirred at ambient temperature for 3 h. Then the mixture was cooled to 0 ^{o}C and 20 mL of H_2O was added slowly. The mixture was extracted with DCM (2 x 50 mL). The combined organic phases were washed with water (2 x 50 mL) and brine (30 mL) and then dried over Na_2SO_4. Removal of the solvent under reduced pressure followed by purification of the resulting residue through a silica flash column using EtOAc: hexanes 3:1 as the eluting solvent led to the desired compound with a yield of 86 % (1.17 g).

Synthesis of compound 7. A solution of compound 4 (1.17 g, 4.05 mmol) in 10 mL of dry DCM was cooled to 0 ^{o}C, and MsCl (1.70 mL, 24.3 mmol) was

added dropwise followed by dry TEA (1.35 mL). After 10 min, the cooling bath was removed, and the reaction proceeded at ambient temperature for ca. 4 h until TLC showed that the starting material was consumed completely. The resulting mixture was washed with water (50 mL), 2-M aqueous NaOH (50 mL) and brine (50 mL), and then dried over Na_2SO_4. Removal of the solvent under reduced pressure followed by purification of the resulting residue through a silica flash column using EtOAc: hexanes 1:2 as the eluting solvent led to the desired compound as a pale yellow solid with a yield of 93 % (1.39 g).

Synthesis of TGX-221 (compound 5). A solution of compound 4 (0.70 g, 1.91 mmol) in 10 mL of dry DCM was cooled to 0 ^{o}C, and aniline (0.5 mL, 16.3 mmol) was added dropwise followed by dry TEA (1 mL). The mixture was refluxed for 4 h and then stirred at ambient temperature overnight. The mixture was washed with water (2 x 50 mL) and brine (50 mL), and then dried over Na_2SO_4. Removal of the solvent under reduced pressure followed by purification of the resulting residue through a silica flash column using EtOAc: hexanes 3:1 as the eluting solvent led to the desired compound as a pale yellow solid with a yield of 80 % (0.56 g).

Synthesis of 2-(Phenylamino)ethanol (compound 6). Following the procedure of Bhanu et al (30), a mixture of aniline (4.66 g, 50 mmol) and 2-bromoethanol (4.34 g, 33 mmol) was heated at 90 ^{o}C under an argon atmosphere for 4 h. The resulting solid was dissolved in ethyl acetate (100 mL), washed with 2-M aqueous NaOH (3 x 20 mL) followed by brine (50 mL), and then dried over Na_2SO_4. Removal of the solvent under reduced pressure followed by purification of the resulting residue through a silica flash column using EtOAc:

hexanes 1:2 as the eluting solvent led to the desired compound with a yield of 89 % (4.03 g).

Synthesis of compound 8 (BL05). A solution of compound 5 (0.47 g, 1.28 mmol) in 10 mL of dry DCM was cooled to 0 ^{o}C, and a solution of 2-(phenylamino)ethanol (0.70 g, 5.12 mmol) in 5 mL of dry DCM was added dropwise followed by dry TEA (1 mL). After 10 min, the mixture was refluxed for ca. 15 h until TLC showed that the starting material was consumed completely. The resulting mixture was washed with 2-M aqueous HCl, water, saturated $NaHCO_3$ aqueous solution and brine, and then dried over Na_2SO_4. Removal of the solvent under reduced pressure followed by purification of the resulting residue through a silica flash column using EtOAc: hexanes 5:1 as eluting solvent led to the desired compound with a yield of 69 % (0.36 g).

Synthesis of BL05-palmitate derivative (BL05-PA). BL05 (compound 8) (0.10 g, 0.24 mmol) and palmatic anhydride (0.24 g, 0.48 mmol) were suspended in 10 mL of dry DCM, and 0.20 mL of dry pyridine was added dropwise. The mixture was stirred overnight at ambient temperature until TLC showed that the starting material was consumed completely. The resulting mixture was washed with 2-M aqueous HCl (30 mL), water, saturated $NaHCO_3$ aqueous solution and brine. Removal of the solvent under reduced pressure followed by purification of the resulting residue through a silica flash column using EtOAc: hexanes 3:1 as the eluting solvent led to the desired compound with a yield of 95 % (0.15 g).

Synthesis of BL05-hexanoate derivative (BL05-HA). A solution of BL05 (compound 8) (0.18 mg, 0.45 mmol) in 5 mL of dry DCM was cooled to 0 ^{o}C, and hexanoyl chloride (0.26 mL, 1.80 mmol) was added followed by dry pyridine (0.38

mL). After 10 min, the cooling bath was removed, and the reaction proceeded at ambient temperature overnight until TLC showed that the starting material was consumed completely. The resulting mixture was washed with 2-M aqueous HCl, water, saturated $NaHCO_3$ aqueous solution and brine. The organic phase was dried over Na_2SO_4. Removal of the solvent under reduced pressure followed by purification of the resulting residue through a silica flash column using EtOAc: hexanes 2:1 as the eluting solvent led to the desired compound as a pale yellow solid with a yield of 91 % (0.266 g).

2.2.3 Synthesis of Azide Poly(ethylene glycol)-block-Poly(ε-caprolactone) Copolymers (N_3-PEG-PCL)

All glassware were flamed dried under vacuum and were handled under a dry argon stream. The N_3-PEG-PCL copolymer was prepared by acid catalyzed ring-opening polymerization reaction of ε-caprolactone in the presence of N_3-PEG-OH as an initiator. The typical process is described as follows. N_3-PEG-OH was azeotropically dried using anhydrous toluene under reduced pressure. ε-caprolactone was dried over CaH_2 overnight and then distilled under vacuum. N_3-PEG-OH (0.375 g, 0.0647 mmol) was dissolved in 8 mL of dry DCM, followed by the addition of 0.75 mL of ε-caprolactone (100 eq). The polymerization was initiated by the addition of 1-M HCl in diethyl ether (0.8 mL, 3 eq) at 25 ℃. After 24 h, the mixture was poured into diethyl ether to precipitate the copolymer. Then, the N_3-PEG-PCL copolymer was further purified by precipitation in cold acetone. The residual solvent was removed under reduced pressure.

2.2.4 Characterization of the polymeric material

The N_3-PEG-PCL was dissolved in $CDCl_3$ for ^{1}H-NMR spectroscopy. Gel

permeation chromatography (GPC) was used to determine the polymer molecular weight distribution. GPC analysis was performed on a Shodex GPC LF-804 column thermostated at 40℃ with DMF and 10-mM LiCl as the mobile phase at a flow rate of 0.8 mL/min. Peaks were detected using a refractive index detector (RID-10A, Shimadzu). Narrow molecular weight distribution polyethylene glycols (Scientific Polymer Products Inc., Ontario, NY) were used as standards for GPC analysis.

2.2.5 Lipid nanoparticle preparation

2.2.5.1 Solid lipid nanoparticle (SLN)

Three formulation methods were used to make SLN: thin film, hot homogenization and solvent precipitation. Particle sizes were measured by dynamic light scattering. Drug release studies were performed in PBS at 37 °C.

2.2.5.1.1 Thin film

In a round bottom flask, 50 mg solid lipid, Compritol® 888 ATO or Dynasan® 114, and 25 % (w/w) surfactant, lecithin, were dissolved in 5 mL chloroform. The mixture was stirred at ambient temperature until all the components were dissolved. Then, the organic solvent was evaporated using a rotary evaporator under reduced pressure. A thin layer of a uniform film was formed on the bottom of the flask. The thin film was then dried overnight under the vacuum. The dried thin film was re-hydrated with 5 mL co-surfactant solution, 2.5 % (w/w) S-40 polyoxyl stearate in ddH_2O. To reduce the particle size, the nanoparticle solution was sonicated on ice for 2 min using a sonic dismembrator (Fisher Scientific, Pittsburgh, PA).

2.2.5.1.2 Hot homogenization

In a glass vial, 0.1 g Dynasan® 114, a low melting point solid lipid, and 0.05 mL Tween 80, the surfactant, were heated and melted. The melted lipid mixture was poured into 10 mL hot ddH_2O with 0.5 % Tween 80 under sonication.

2.2.5.1.3 Solvent precipitation

In a glass vial, 0.05 g solid lipid, Dynasan ® 114, and 0.05 g surfactant, lecithin, were mixed and fully dissolved in 1 mL chloroform. The oil phase was drop-wise added to the co-surfactant solution, 5 % sodium taurocholate in ddH_2O. The organic solvent was removed by dialysis method.

2.2.5.2 Nanostructured lipid carrier

In a round bottom flask, 50 mg Apifil® or Compritol® 888 ATO (solid lipid), 50 mg Stepan® 108 or alpha- tocopherol (oil), 10 mg Phospholipon® 90H (surfactant) and 2.5 mg PEG_{2000}-DSPE were dissolved in 2 mL ethanol. The mixture was stirred at ambient temperature until all the compounds were fully dissolved. The oil phase was drop-wise added to 10 mL co-surfactant solution, 5 % sodium taurocholate in ddH_2O.

2.2.6 Poly(lactide-co-gylcolid) (PLGA) nanoparticle preparation

PLGA polymer with different inherent viscosities (0.23 dl/g, 0.69 dl/g and 1.05 dl/g) were used to make PLGA nanoparticles. PLGA (35 mg) was dissolved in 3 mL acetone. The organic phase was added to 15 mL surfactant solution, 0.1 % Pluronic® F-127 or PVA, using a syringe pump. The nanoparticle solution was purified by dialysis against 0.2 % mannitol for 2 days using 100-kDa cutoff dialysis tubing.

2.2.7 PEG-PCL micelle preparation

The N_3-PEG-PCL (15 mg, 1.3 mmol) was dissolved in 0.5 mL of dimethylacetamide (DMAc) and the organic solution was added dropwise to 2 mL of ddH_2O with mechanical stirring. The organic solvent was removed by overnight dialysis against phosphate buffered saline (PBS) using 10-kDa molecular weight cutoff (MWCO) dialysis tubing (Spectrum Laboratories, Rancho Dominguez, CA). Drug-loaded micelles were prepared by mixing the drugs with the copolymer in DMAc before adding ddH_2O.

The aptamer, PSAMa10, was functionalized by addition of an alkyne group using the following procedure. PSMAa10 (0.2 μmol, 3.7 mg) was dissolved in 500 μl of 0.1-M carbonate buffer (pH 9.0). The alkyne-NHS ester (2.3 mg) was dissolved in 60 μl of DMSO, and 6 μl of the alkyne-modified NHS ester solution was added to the carbonate buffer containing the aptamer. After mixing for 4 h at ambient temperature, the alkyne modified PSMAa10 was purified using a centrifugal filtration device (Amicon® Ultra Centrifugal Filter 10K, Millipore Corp.).

The near infrared dye, IR-820, was modified to include an alkyne by conjugation of 1-amino-3-butyne. Briefly, 150 mg of IR-820 (0.177 mmol) was dissolved in 10 mL of DMF. Then, 61 mg of 1-amino-3-butyne (5 eq) and 123 μL of TEA (5 eq) were added. The solution was stirred at 40 ℃ for 8 h. The final product was purified by silica flash chromatography using EtOAc: methanol 1:2 as the elution solvent.

Both alkyne modified PSMAa10 and IR-820 were conjugated to the micelle's surface by azide alkyne Huisgen cycloaddition (i.e. click reaction). Briefly, 50 μg of alkyne modified PSMAa10 and 100 μg of alkyne modified IR-820 were added

to N_3-PEG-PCL micelles (2.5 mg/mL) prepared in ddH_2O. Copper sulfate (0.6 μmol/mL) and sodium ascorbate (3.0 μmol/mL) were used as a catalyst. The reaction mixture was gently stirred at ambient temperature overnight. The modified micelles were purified by dialysis against PBS using 10,000 MWCO dialysis tubing (SnakeSkin® Pleated Dialysis Tubing, Thermo Scientific) for 24 h. To determine the extent of the reaction, the supernatant was separated from the micelle solution using a Microcon YM-100 centrifugal concentrator (0.5-mL capacity, NMWL 100, 000, Millipore Corp.) at 11,000×g for 15 min. The filtrate was analyzed by high-performance liquid chromatography (HPLC) (LC-2010CHT, Shimadzu).

2.2.8 Micelle characterization

The critical micelle concentration (CMC) of N_3-PEG-PCL micelles was determined by measuring the excitation ratio of pyrene using a fluorophotometer (RF-5301 PC, Shimadzu). For example, solutions of N_3-PEG-PCL micelles were prepared by serial dilution and then incubated with 0.6-μM pyrene for 1 h at 65 ℃ and then 18 h at ambient temperature in the dark. The fluorescent emission of pyrene was measured at 390 nm. The fluorescent excitement ratio of pyrene at 339 and 334 nm changes in response to the probe's microenvironment polarity. A sharp increase in the 339/334 excitation ratio indicates the CMC as the pyrene preferentially partitions into the hydrophobic core of N_3-PEG-PCL micelles.

The formation of micelles was determined by GPC (Shodex OHpak SB-803 HQ, Showa Denko America, Inc.) using a Shimadzu 2010CHT system. GPC was performed using ddH_2O as the mobile phase with a flow rate of 0.8 mL/min, and the GPC column was thermostated at 40 ℃. Elution peaks were detected using

an evaporative light scattering detector (ELSD-LTII, Shimadzu). The size and polydispersity of micelles were measured with a ZetaPALS (Brookhaven Instruments Corp.) using the Gaussian distribution.

The drug loading efficiency (DL %) and encapsulation efficiency (EE %) of BL05-HA in PEG-PCL micelles were calculated according to the following equations:

$$\text{DL } \% = \frac{\text{weight of the drug in micelle}}{\text{weight of the polymer and drug}} \times 100\ \%$$

$$\text{EE } \% = \frac{\text{weight of the drug in micelle}}{\text{weight of the feeding drug}} \times 100\ \%$$

GPC micelle fraction was collected and dried by speed-vap. The dried micelle fraction was weighed to determined weight of the polymer and drug. Then, the dried micelle was redissolved in MeOH and drug weight in micelle was evaluated by HPLC analysis.

2.2.9 Cytotoxicity assay

The prostate cancer cell lines DU145 and LNCaP were maintained in RPMI-1640 medium, and PC3 cells were maintained in F-12K medium (ATCC, Manassas, VA). LNCaP is a PSMA positive cell line, whereas DU145 and PC3 are PSMA negative. Both were supplemented with 10 % fetal bovine serum (Hyclone Laboratory Inc., Logan, Utah). Cells were plated in 96-well flat-bottomed plates at a concentration of 5,000 cells per well in 90 μL of growth medium. After 12 h, TGX-221, BL05, or BL05-HA loaded micelles in PBS were added at concentrations of 0, 0.1, 1, 5, 10, 50 or 100 μM. PBS and 10 μL of trichloroacetic acid (TCA) were added to negative and positive control wells, respectively. After 72 h, 10 μL of 55-μM resazurin blue was added to each well

and incubated at 37 °C for 4 h. After incubation, the resorufin product was measured with a fluorophotometer (SpectraMax Gemini; Molecular Devices, CA) using an excitation wavelength of 560 nm and an emission wavelength of 590 nm. The IC_{50} was determined as the midpoint between positive and negative control groups for each plate using GraphPad Prism 5 software (GraphPad Software Inc., San Diego, CA).

2.2.10 Western blot assay

After serum starvation for 16 h, LNCaP cells were treated with 2-μM TGX-221 or BL05 and 100-ng/mL EGF for 30 min. Then, cells were pelleted and lysed with cell lysis buffer containing protease inhibitors. Protein concentrations were determined by BCA assays, and equal amounts of protein extract were separated on a 10 % SDS-polyacrylamide gel, transferred to a nitrocellulose membrane and immunoblotted with anti-pAkt (Ser-473) and Akt (Cell Signaling Technology, Inc., Danvers, MA) followed HRP-conjugated secondary antibodies (Santa Cruz Biotech, Inc., Santa Cruz, CA). The specific bands were detected using a chemiluminescence luminal reagent (Santa Cruz Biotech, Inc., Santa Cruz, CA).

2.2.11 *In vitro* drug release study

The *in vitro* release of the drug from N_3-PEG-PCL micelles into PBS (pH 7.4) was monitored by a dialysis method (31). Dialysis was carried out at 37 °C under sink condition using 10-kDa MWCO dialysis tubing (SnakeSkin®, Thermo Scientific Inc., Rockford, IL). The initial volume of drug-loaded micelles in the dialysis tubing was 5 mL and the sink solution was 4 L. The PBS was changed several times per day to maintain sink conditions. After pre-determined time intervals, samples were withdrawn from the dialysis tubing and analyzed by

HPLC with a reversed phase column (TSK-GEL ® ODS-100Z, Tosoh Bioscience) at 50 ℃ with UV detection at 280 nm. The chromatography conditions were a mobile phase A of 100 % ddH_2O and B of 100 % methanol at a flow rate of 1 mL/min. The gradient program was i) a linear gradient from 50 % to 90 % solvent B over 5 min; ii) 3.5 min with 90 % solvent B; iii) 6.5 min with 100% solvent B; and iv) 10 min with 50% solvent B. Retention times: TGX-221 6.86 min; BL05 6.93 min; BL05-HA 10.14 min and BL05-PA 17.04 min.

2.2.12 Uptake of PSMA-targeted micelles by prostate cancer cells

Fluorescence microscopy was used to examine cellular uptake of IR-820-labeled PSMA-targeted micelles. PSMA negative PC3 cells and PSMA positive LNCaP cells were seeded at a density of 1×10^6 cells in an 8.6-cm^2 chamber slide system (Thermo Scientific). After cells had attached to the microscope slide's surface, the PC3 and LNCaP cells were incubated with the PSMA-targeted (2.5 % weight compared with polymer concentration) or non-targeted micelles for 6 h at 37 ^{0}C. Unbound micelles were removed by washing 3 times with PBS. Fluorescence images were acquired using a Cy5 filter set on a Nikon Eclipse 80i microscope equipped for epifluorescence and an Orca ER camera (Hamamatsu Inc., Bridgewater, NJ).

The cellular uptake and accumulation of PSMA targeted micelles (2.5 % weight compared with polymer concentration) was quantified in LNCaP and PC3 cells. Cells were seeded in 96-well flat-bottom plates at a concentration of 5,000 cells per well in 90 µL of growth medium. After the cells attached to the surface, 10 µL of targeted or non-targeted IR-820-modified micelles were added at different concentrations. After 6 h of incubation, the growth medium was removed and

each well was washed with PBS. The plate fluorescence was measured using a fluorophotometer at an excitation wavelength of 675 nm and an emission wavelength of 750 nm.

2.2.13 Pharmacokinetic evaluation

Male Balb/c mice were maintained in a temperature-controlled room with a 12 h light/dark cycle for at least one week prior to the study. The animal protocol was approved by the Institutional Animal Care and Use Committee (IACUC) at the University of Kansas Medical Center. Animals were administered BL05-HA loaded PSMA-targeted micelles or BL05-HA prepared in propylene glycol at a dose of 30 mg/kg via tail vein injection (100 µl). Blood samples were withdrawn after 5 min, 1, 2, 4, 6, 12 and 24 h from the saphenous vein. A 20-µL blood sample was added to 50 µL of Alsever's solution, which is an anticoagulant. After gently mixing, the blood sample was centrifuged at 3,000 rpm for 10 min. Plasma was prepared by solid phase extraction (SPE) prior to the HPLC analysis. Briefly, plasma sample diluted with 2% NH_4OH (1:3) was applied to the SPE column (Bond Elut-C18, Agilent Technologies, Lake Forest, CA) that was pretreated with 100% MeOH and equilibrated with 100 % ddH_2O. Sample was washed with 5% MeOH in ddH_2O and eluted twice with 150 µL 100 % MeOH.

2.2.14 Efficacy study in xenograft models

Four prostate cancer cell lines, androgen-responsive, LAPC-4 and LNCaP, and androgen non-responsive, C4-2 and 22RV1, were used to generate the subcutaneous xenografts (n = 8). Once xenografts were palpable (30 mm^3 in size), animals were divided randomly into three groups to receive treatment twice a week. The animals were treated with the solvent PPG (as the control), naked

TGX-221 analog BL05 in PPG (BL05) and PSMAa10 aptamer-conjugated nanocarrier with BL05 (APT-Nano-BL05). The total volume of drug solution was 200 μl for tail vain injection. Tumor growth was monitored twice a week and animals were sacrificed once the xenograft tumor in control groups reached the limit of tumor size set by our IACUC. One hour before sacrifice, animals were injected with BrdU solution to label the newly synthesized DNA for evaluating tumor cell proliferation. After tumor dissection, half of the tumor specimens were stored in -80 °C for further analysis and another half of the specimens were subjected for paraffin processing.

2.2.15 Statistical analysis

GraphPad Prism 5 software was used for statistical analysis. A *t*-test was used to test for differences between two data sets, while a one-way ANOVA and Tukey post test was used to analyze the differences when more than two data sets were compared. In all comparisons, statistical significance was set at $p \leq 0.05$.

2.3 Results

2.3.1 Drug synthesis

We successfully synthesized TGX-221, BL05 and the fatty acid prodrugs. The synthesis of TGX-221 was accomplished with 2-amino-3-bromo-5-methylpyridine and malonyl dichloride as the starting materials through 6 steps with an overall yield of 14 % and BL05 with an overall yield of 12 %. The structure of each compound was determined by ^{1}H-NMR, ^{13}C-NMR or together with high resolution APCI-MS or ESI-MS.

Compound 1: ^{1}H-NMR (DMSO-d_6, 400 MHz): δ = 8.74 (s, 1H), 8.29 (s, 1H), 5.55 (s, 1H), 2.34 (s, 3H), which was consistent with the reported data.

Compound 2: ^{1}H-NMR ($CDCl_3$, 400 MHz): δ = 8.72 (s, 1H), 7.87 (d, *J* = 1.9 Hz, 1H), 5.61 (s, 1H), 3.84-3.80 (m, 4H), 3.74-3.69 (m, 4H), 2.35 (s, 3H), which was consistent with the reported data.

Compound 3: ^{1}H-NMR ($CDCl_3$, 400 MHz): δ = 8.88 (s, 1H), 7.86 (d, *J* = 2.2 Hz, 1H), 5.66 (s, 1H), 3.84-3.79 (m, 4H), 3.67-3.62 (m, 4H), 2.79 (s, 3H), 2.38 (d, *J* = 1.0 Hz, 3H), which was consistent with the reported data.

Compound 4: ^{1}H-NMR ($CDCl_3$, 400 MHz): δ = 8.67 (s, 1H), 7.50 (d, *J* = 1.9 Hz, 1H), 5.63 (s, 1H), 5.25-5.18 (m, 1H), 4.63 (d, *J* = 5.0 Hz, 1H), 3.82 (t, *J* = 2.9 Hz, 4H), 3.61 (t, *J* = 4.2 Hz, 4H), 2.35 (d, *J* = 1.0 Hz, 3H), 1.63 (d, *J* = 6.6 Hz, 3H); ^{13}C-NMR ($CDCl_3$, 100 MHz): δ = 18.1, 22.1, 44.5 (x2), 49.1, 66.4 (x2), 81.1, 117.4, 122.3, 135.3, 137.3, 147.5, 159.0, 160.2; HRMS (ESI) Calc'd for $C_{15}H_{19}N_3NaO_3$ $(M + Na)^+$: 312.1324; Found: 312.1329.

Compound 5 (TGX-221): ^{1}H-NMR ($CDCl_3$, 400 MHz): δ = 8.67 (s, 1H), 7.60 (d, *J* = 2.0 Hz, 1H), 7.13 (d, *J* = 7.4 Hz, 1H), 7.12 (d, *J* = 6.6 Hz, 1H), 6.68 (t, *J* = 7.3 Hz, 1H), 6.48 (d, *J* = 7.6 Hz, 2H), 5.68 (s, 1H), 5.15 (d, *J* = 5.6 Hz, 1H), 4.39 (bs, 1H), 3.81 (t, *J* = 5.0 Hz, 4H), 3.72-3.62 (m, 4H), 2.26 (d, *J* = 1.0 Hz, 3H), 1.59 (d, *J* = 6.8 Hz, 3H); ^{13}C-NMR ($CDCl_3$, 100 MHz): δ = 18.3, 22.1, 44.6 (x2), 49.1, 66.6 (x2), 81.3, 113.2 (x2), 117.6, 122.5, 123.8, 129.2 (x2), 135.4, 137.3, 146.8, 147.5, 159.1, 160.2; HRMS (ESI) Calc'd for $C_{21}H_{25}N_4O_2$ $(M + H)^+$: 365.1978; Found: 365.1975.

Compound 6: ^{1}H-NMR ($CDCl_3$, 400 MHz): δ = 7.22 (dd, *J* = 7.4, 7.3 Hz, 2H), 6.78 (d, *J* = 7.3 Hz, 1H), 6.69 (d, *J* = 7.7 Hz, 2H), 3.84 (t, *J* = 5.1 Hz, 2H), 3.32 (t, *J* = 4.9 Hz, 2H), 3.03 (bs, 2H).

Compound 7: ^{1}H-NMR ($CDCl_3$, 400 MHz): δ = 8.89 (dd, *J* = 2.1, 1.1 Hz, 1H),

7.87 (d, *J* = 2.2 Hz, 1H), 5.88 (q, *J* = 6.8 Hz, 1H), 5.68 (s, 1H), 3.82 (t, *J* = 5.2 Hz, 4H), 3.65 (t, *J* = 5.1 Hz, 4H), 3.16 (s, 3H), 2.39 (d, *J* = 0.9 Hz, 3H), 1.88 (d, *J* = 6.8 Hz, 3H); HRMS (ESI) Calc'd for $C_{16}H_{22}N_3O_5$ S $(M + H)^+$: 368.1280; Found: 368.1276.

Compound 8 (BL05): ^{1}H-NMR ($CDCl_3$, 400 MHz): δ = 8.70 (s, 1H), 7.45 (s, 1H), 7.22 (d, *J* = 8.6 Hz, 1H), 7.20 (d, *J* = 8.5 Hz, 1H), 6.86 (d, *J* = 8.2 Hz, 2H), 6.76 (t, *J* = 6.9 Hz, 1H), 5.64-5.60 (m, 1H), 5.59 (s, 1H), 3.63-3.57 (m, 4H), 3.54 (t, *J* = 6.0 Hz, 2H), 3.44 (t, *J* = 5.6 Hz, 2H), 3.41-3.35 (m, 4H), 2.34 (s, 3H), 1.62 (d, *J* = 7.0 Hz, 3H); ^{13}C-NMR ($CDCl_3$, 100 MHz): δ = 16.9, 18.4, 44.4 (x2), 47.3, 52.3, 60.0, 66.5 (x2), 81.3, 114.2 (x2), 117.8, 121.7, 124.3, 129.2 (x2), 135.5, 136.5, 148.0, 148.2, 159.0, 160.1; HRMS (ESI) Calc'd for $C_{23}H_{29}N_4O_3$ $(M + H)^+$: 409.2240; Found: 409.2229.

BL05-PA: ^{1}H-NMR ($CDCl_3$, 400 MHz): δ = 8.71 (s, 1H), 7.42 (d, *J* = 1.8 Hz, 1H), 7.23 (d, *J* = 8.7 Hz, 1H), 7.21 (d, *J* = 8.7 Hz, 1H), 6.81 (d, *J* = 8.2 Hz, 2H), 6.74 (t, *J* = 7.2 Hz, 1H), 5.61 (s, 1H), 5.60-5.57 (m, 1H), 4.16-4.09 (m, 1H), 4.00-3.93 (m, 1H), 3.67-3.59 (m, 5H), 3.58-3.49 (m, 1H), 3.41 (t, *J* = 4.9 Hz, 4H), 2.34 (d, *J* = 0.9 Hz, 3H), 2.28 (t, *J* = 7.5 Hz, 2H), 1.66 (d, *J* = 7.2 Hz, 4H), 1.61 (t, *J* = 7.2 Hz, 2H), 1.35-1.22 (bs, 23H), 0.90 (t, *J* = 7.0 Hz, 3H); ^{13}C-NMR ($CDCl_3$, 100 MHz): δ = 14.1, 17.5, 18.4, 22.7, 24.9, 29.2, 29.3, 29.4 (x2), 29.5 (x2), 29.6 (x2), 29.7(x2), 31.9, 34.2, 44.0, 44.4 (x2), 51.8, 61.8, 66.5 (x2), 81.3, 113.1 (x2), 117.4, 121.7, 124.2, 129.3 (x2), 135.7, 136.0, 147.7, 147.9, 159.0, 160.1, 173.7; HRMS (ESI) Calc'd for $C_{39}H_{59}N_4O_4$ $(M +H)^+$: 647.4536; Found: 647.4528.

BL05-HA: ^{1}H-NMR ($CDCl_3$, 400 MHz): δ = 8.71 (s, 1H), 7.42 (d, *J* = 1.8 Hz, 1H), 7.23 (d, *J* = 8.8 Hz, 1H), 7.22 (d, *J* = 8.7 Hz, 1H), 7.21 (d, *J* = 8.7 Hz, 1H),

6.81 (d, *J* = 8.2 Hz, 2H), 6.74 (t, *J* = 7.2 Hz, 1H), 5.61 (s, 1H), 5.60-5.57 (m, 1H), 4.17-4.09 (m, 1H), 4.00-3.93 (m, 1H), 3.70-3.58 (m, 5H), 3.41 (t, *J* = 4.9 Hz, 4H), 2.34 (d, *J* = 0.9 Hz, 3H), 2.28 (t, *J* = 7.4 Hz, 2H), 1.66 (d, *J* = 7.0 Hz, 3H), 1.64-1.58 (m, 1H), 1.38-1.26 (m, 5H), 0.91 (t, *J* = 6.8 Hz, 3H); ^{13}C-NMR ($CDCl_3$, 100 MHz): δ = 13.9, 17.4, 18.4, 22.3, 24.6, 31.3, 34.1, 44.0, 44.4 (x2), 51.8, 61.8, 66.5 (x2), 81.3, 113.1 (x2), 117.4, 121.7, 124.2, 129.3 (x2), 135.7, 136.0, 147.7, 147.9, 159.0, 160.1, 173.7; HRMS (ESI) Calc'd for $C_{29}H_{39}N_4O_4$ $(M + H)^+$: 507.2971; Found: 507.2955.

2.3.2 SLN characterization

SLN prepared by thin film, hot homogenization and solvent precipitation methods were compared. The solid lipid Compritol® 888 ATO, a glycerol behenate, was used. Particle sizes were measured by dynamic light scattering (Table 1). We found that the solvent precipitation method gave the smallest particle. In addition, the particle size also can be reduced by increasing surfactant ratio.

The influence of the lipid was also studied, using the solvent precipitation method. The melting point of Compritol® 888 ATO and Dynasan® 114 are 69 - 74 °C and 56 -57 °C, respectively. The average particle size of SLN dispersion can be reduced to 87.5 ± 2.3 nm by using a lower melting point lipid. For 20 % (w/w) TGX-221 loaded Compritol® 888 ATO SLN, encapsulation efficiency was approximately 95 % (Table 2).

Table 1. Particle sizes of empty SLN prepared by different formulation methods and different lipid/surfactant ratios.

Formulation		Size (nm) (mean ± SD)
Thin Film	Lipid : Surfactant (3:1)	475.3 ± 59
	Lipid : Surfactant (2:1)	414.5 ± 12.6
Hot Homogenization	Lipid : Surfactant (3:1)	312.5 ± 12.5
	Lipid : Surfactant (2:1)	235.2 ± 13.6
Solvent Precipitation	Lipid : Surfactant (2:1)	107.8 ± 0.5

Table 2. Encapsulation efficiencies of TGX-221 loaded nanoparticles prepared by different formulation methods.

Formulations	Encapsulation Efficiency
SLN Compritol® 888 ATO w/ 10 % TGX-221	95.3 %
SLN Compritol® 888 ATO w/ 20 % TGX-221	92.5 %
SLN Dynasan 114 w/ 10 % TGX-221	89.9 %
SLN Dynasan 114 w/ 10 % TGX-221	86.2 %
NLC Comprotol® 888 ATO w/ 10 % TGX-221	95.4 %
NLC Apifil® w/ 10 % TGX-221	91.2 %
PEG-PCL Micelle w/ 10 % TGX-221	87.5 %
PLGA (0.24 dl/g) F-127 w/ 5 % TGX-221	39.1 %
PLGA (0.69 dl/g) F-127 w/ 5 % TGX-221	51.7 %

The release kinetics of SLNs prepared by solvent precipitation method with different lipid and drug loading degrees were evaluated (Fig. 2). We found that different lipid showed similar release profiles and the drug loading degree did not affect the release half-lives.

2.3.3 NLC characterization

Particle sizes and zeta potentials of NLCs prepared by different combinations are shown in Table 3. We showed that the particle made by Compritol® 888 ATO was more stable compared to that of Apifil®. However, the particle sizes of different lipid matrix NLCs were approximately the same. In addition, the particle sizes and zeta potentials were not significantly changed between empty and drug loaded particles.

The *in vitro* release study indicated that different lipid and surfactant combinations did not show significantly influence on TGX-221 release (Fig. 3). However, compared to SLN, NLC improved drug release half-lives from 2-3 h to 5-6 h.

2.3.4 PLGA nanoparticle characterization

The particle sizes of PLGA nanoparticles made with PLGAs of different inherent viscosities are shown in Table 4. We found that the surfactant type significantly influenced on particle size. The particle size was also sensitive to the inherent viscosity of PLGA. The PLGA nanoparticles stabilized by PVA were the smallest. In addition, PVA stabilized particles showed a longer *in vitro* release half-life compared to the particles stabilized by Pluronic® F-127 (Fig. 4).

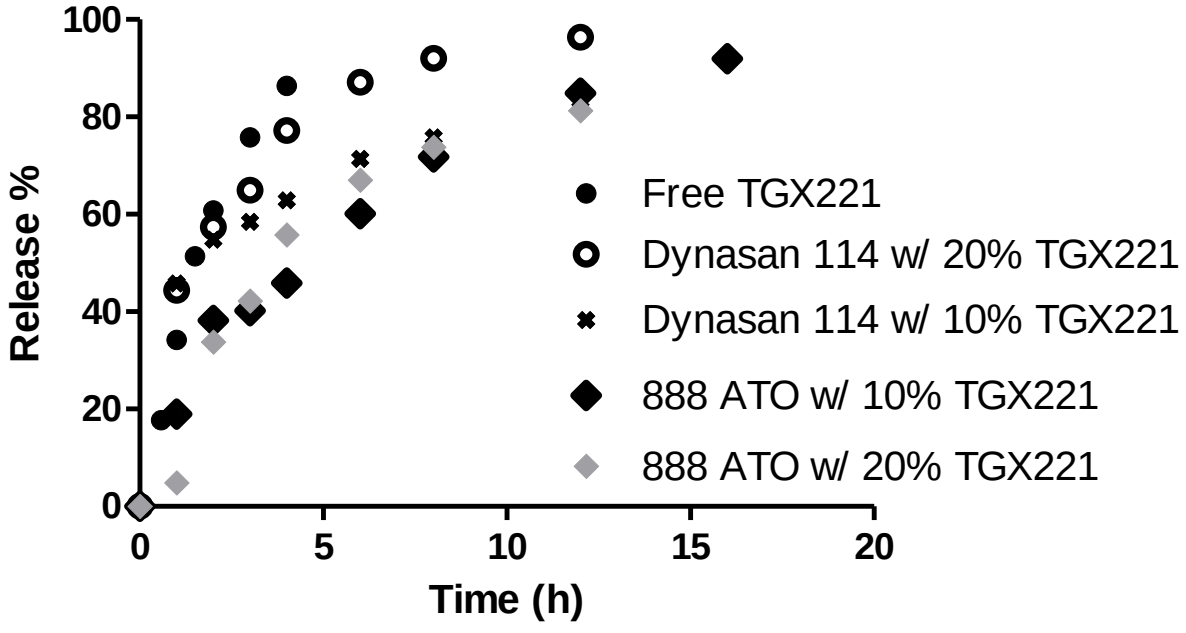

Fig. 2: *In vitro* release profiles of TGX-221 loaded SLNs made with different lipids and different drug loading degree.

Table 3: Particle sizes and zeta potentials of empty and drug loaded NLCs (mean ± SD).

	Formulation	Size (nm)	Zata Potential (mV)
Empty particle	888 ATO + S108	150.6 ± 1.7	-48.97 ± 2.72
	888 ATO + α-tocopherol	171.3 ± 11.4	-42.97 ± 2.05
	Apifil + S108	150.6 ± 4.7	-28.2 ± 4.43
w/ 10% TGX221	888 ATO + S108	169.7 ± 3.6	-50.48 ± 3.89
	Apifil + S108	165.6 ± 2.3	-33.5 ± 0.91
	Apifil + 90H	129.3 ± 0.1	-20.77 ± 0.31

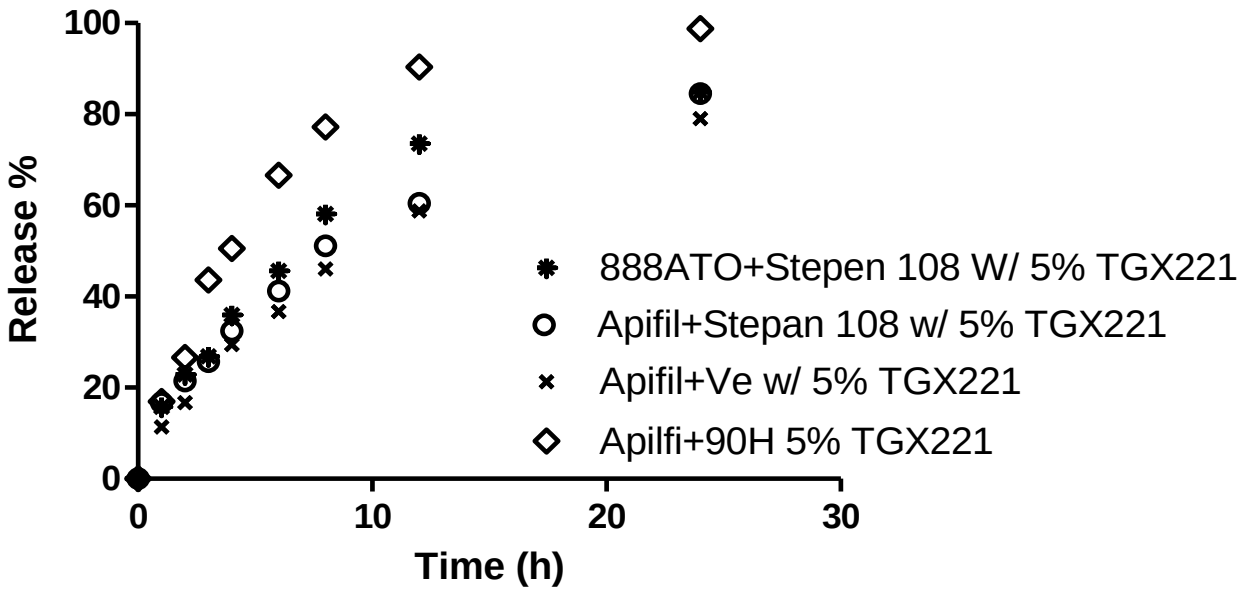

Fig. 3: *In vitro* release profiles of NLC prepared by different lipid and surfactant combinations.

Table 4: Particle sizes measurements of NLC stabilized by different surfactants.

Formulation		Size (nm) (mean ± SE)
PLGA (1.05 dl/g)	Pluronic® F-127	168.5 ± 1.5
PLGA (0.69 dl/g)	Pluronic® F-127	181.2 ± 2.7
PLGA (0.23 dl/g)	Pluronic® F-127	171.7 ± 2.6
	Polyvinyl alcohol (PVA)	119.1 ± 1.9
	Poly (acrylic acid) (PAA)	212.5 ± 5.6
	PVA: PAA (50:50)	180.4 ± 3.1

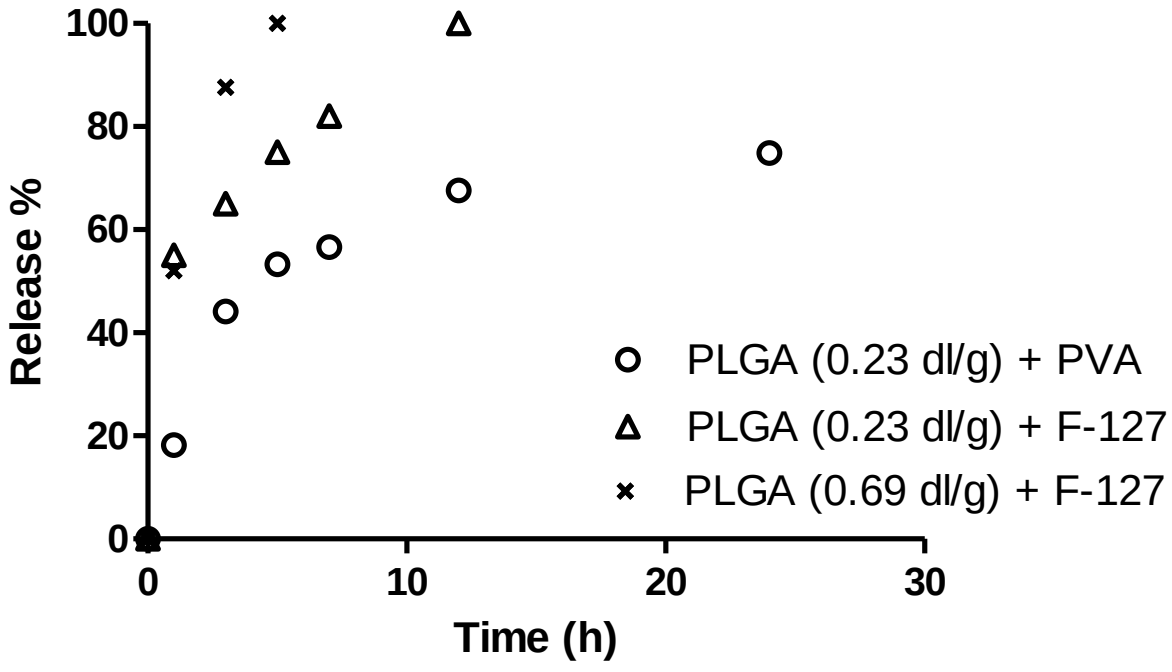

Fig. 4: *In vitro* release profiles of different PLGA nanoparticles.

2.3.5 PEG-PCL micelle preparation and characterization

The N_3-PEG-PCL block copolymer was synthesized by a ring opening reaction. ^{1}H-NMR spectra showed two main peaks at 3.67 (-O***CH2CH2***) and 4.08 (-O***CH2***CH2CH2CH2CH2CH2CO-) that correspond to PEG and PCL, respectively. The molecular weight of N_3-PEG-PCL copolymer determined by ^{1}H-NMR was 5,800:5,800 and the polydispersity of this polymer measured by GPC was 1.10. The CMC was determined to be 300 nM using the pyrene incorporation assay. Based on Gibb's free energy of micellization, the nanomolar CMC of PEG-PCL copolymer indicated that the micelle had high thermodynamic stability. For 10 % (w/w) BL05-HA loaded PEG-PCL micelles, the encapsulation efficiency was 74.5 ± 4.6 %.

The N_3-PEG-PCL micelles were prepared using a solvent displacement method. The PCL block served as a hydrophobic core of the micelle and physically entrapped the poorly water soluble anticancer drug into the micelle. GPC was used to confirm the formation of PEG-PCL micelles. PEG-PCL micelles are known to be stable when diluted below the CMC during GPC analysis, which reflects a high kinetic stability against dissociation (32). The micelles' hydrodynamic diameter from DLS with Gaussian volume weighting was approximately 50 nm (Table 1), which is suitable for intravenous administration and extravasation in tumors (33).

2.3.6 Conjugation of PSMAa10 to PEG-PCL micelles

The alkyne modified aptamer, PSMAa10, was confirmed by ESI-MS ($[M+Na]^+$ = 18,928.0). The alkyne modified PSMAa10, was conjugated to the azide end group of the PEG-PCL copolymer by the Huisgen cycloaddition click reaction.

The conjugation efficiency was determined by quantifying the unconjugated ligand remaining in the supernatant. The amount of PSMAa10 conjugated to the N_3-PEG-PCL micelle surface increased with increasing reaction time: 1 h, 0.017 ± 0.005 (yield: 14.2 %); 3 h, 0.103 ± 0.010 (yield: 20.6%); 5 h, 0.123 ± 0.015 (yield: 24.6 %) mg PSMAa10 / mg N_3-PEG-PCL. Since precipitation occurred after 5-h, the Click reaction time was controlled at 3 h. The conjugation of PSMAa10 to the micelle's surface was examined by agarose gel electrophoresis (data not shown). The near infrared fluorophore IR-820 was functionalized with an alkyne by TEA buffered condensation with 1-amino-3-butyne. The successful conjugation was confirmed by ESI-MS. The micelle surface also was modified with IR-820 by click reaction. The IR-820 conjugated micelles had a maximum absorption wavelength of 675 nm and an emission wavelength of 745 nm.

2.3.7 Characterization of conjugated PEG-PCL micelles

Particle sizes of different micelle formulations were determined by dynamic light scattering (Table 5). All of the formulations had particle sizes that were smaller than 100 nm and the *in vitro* release half-lives were improved by encapsulating more hydrophobic prodrugs. The sizes of all of the nanoparticle formulations were smaller than 100 nm, which is suitable for intravenous application. The *in vitro* release half-lives of TGX-221, BL05, BL05-HA and BL05-PA were investigated at simulated *in vivo* conditions using a bath at pH 7.4 and 37 °C (Table 5). In addition, the release half-lives of TGX-221 and its analog, BL05, from PEG-PCL micelles were identical, which is likely due to the similar lipophilicity of the two compounds. TGX-221 had a calculated $\log P_{o/w}$ of 2.14 ± 0.68 and BL05 was 1.81 ± 0.67 (ALogPS 2.1, http://www.vcclab.org). The more

hydrophobic ester prodrugs, BL05-HA ($logP_{o/w}$ 4.15 ± 0.31) and BL05-PA ($logP_{o/w}$ 8.42 ± 0.83), had much longer release half-lives of 5 and 6.5 days in PEG-PCL micelles, respectively. The prodrugs tended to stay in the hydrophobic PCL core of the micelle, and they were protected from hydrolysis in the hydrophobic core due to limited penetration of water. The aptamer conjugated micelle was larger than the non-targeted micelle, and the conjugation of IR-820 was confirmed by observing the increased Stokes shift of fluorescent dye. The Stokes shift of IR-820 increased after conjugation to the micelle surface due to electromagnetic retardation (34).

Table 5: Characterization of different drug loaded PEG-PCL micelles.

	Size (nm) (Mean ± SD)	***In vitro* Release Half-life**
Empty Micelle	27.6 ± 0.2	-
PSMA-targeted Micelle	40.5 ± 0.8	-
TGX-221 Loaded Micelle (5% w/w)	54.5 ± 0.3	<1h
BL05 Loaded Micelle (5% w/w)	59.8 ± 2.2	< 1 h
BL05-HA Loaded Micelle (5% w/w)	49.9 ± 0.5	5 days
BL05-PA Loaded Micelle (5% w/w)	29.9 ± 0.1	6.5 days
BL05-HA Loaded PSMA-targeted Micelle	58.8 ± 0.9	-

2.3.8 *In vitro* cytotoxicity studies

The IC_{50}s of TGX-221, BL05 and BL05-HA were determined in DU145, PC3 and LNCaP cells (Table 6). BL05-PA was not soluble in PBS with 1 % DMSO, and it was not tested further. TGX-221, BL05 and BL05-HA showed selective cytotoxicity to LNCaP cells, which may be due to the deficiency of PTEN in this cell line and the accumulation of PIP3 in the cells. A Western blot was performed to determine if both TGX-221 and BL05 are involved in the same cell signaling pathway that contributes to the selective cytotoxicity. As demonstrated by Western blot, TGX-221 and BL05 inhibited phosphorylation of Akt (Fig. 5), which in turn indicated the inhibitor of PI3K activity.

The cytotoxicity of empty micelles, PSMA-targeted empty micelles, IR-820-labeled empty micelles and IR-820-labeled PSMA-targeted micelles was examined in DU145 prostate cancer cells (Fig. 6). The drug free targeted micelles did not inhibit cell growth. However, the dye-labeled micelles did inhibit cell growth, so they were not characterized further *in vivo*.

Table 6: IC50s of TGX-221, BL05 and BL05-HA in different prostate cancer cell lines. All of the drugs showed selective cytotoxicity to PSMA-positive LNCaP cells (*: $p < 0.05$; **: $p < 0.01$).

	TGX-221 (μM) (Mean ± SE)	**BL05 (μM) (Mean ± SE)**	**BL05-HA (μM) (Mean ± SE)**
DU145	35.6 ± 0.12	32.4 ± 0.67**	52.5 ± 0.15**
PC3	18.2 ± 0.85	23.4 ± 0.74**	21.8 ± 0.66**
LNCaP	3.98 ± 0.18	4.036 ± 0.11	3.19 ± 0.12*

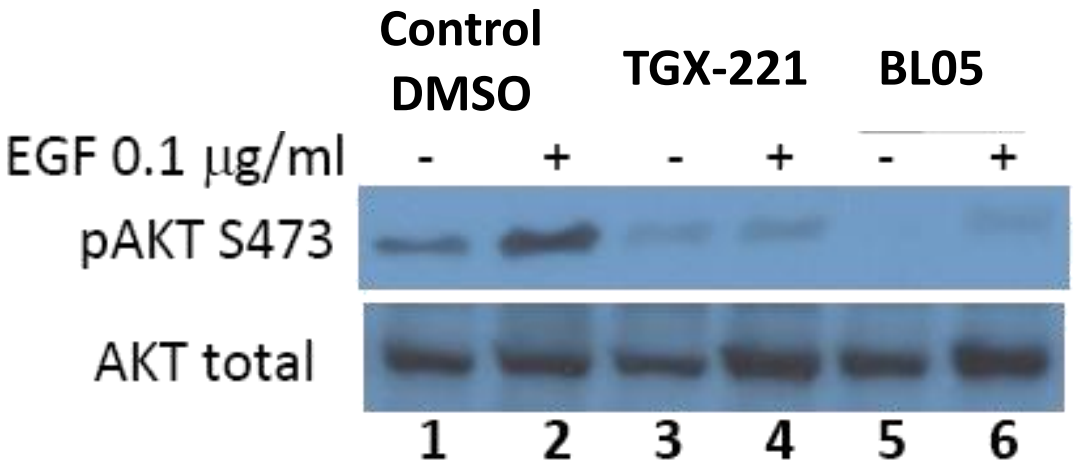

Fig. 5: Western blot analysis of Akt phosphorylation on Ser473 and total Akt protein levels with different treatments. Both TGX-221 and BL05 showed inhibitory effects on the phosphorylation of Akt.

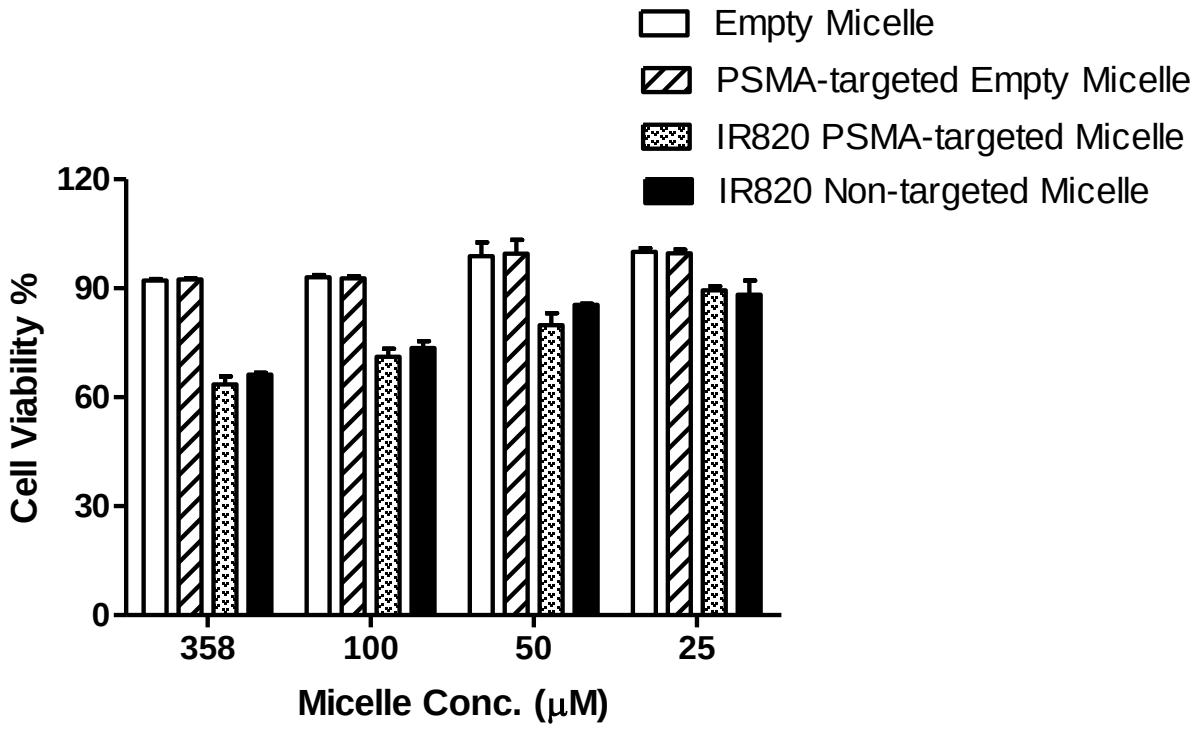

Fig. 6: Cytotoxicity of empty micelles in DU145 cells (Mean ± SD).

2.3.9 Micelle formulation effects on cellular uptake of the drug

The DU145 cells were treated with BL05-HA in DMSO and BL05-HA loaded in non-targeted micelles. The solubility of BL05-HA in 5 % DMSO was determined to be 32.35 μg/mL (49.86 μM). After a 12-h treatment, the cell culture medium was analyzed for extracellular drug content by HPLC, and the drug uptaken by the cells was quantified (Fig. 7). Micelle formulations significantly improved the cellular uptake at all concentrations, also DMSO was not required to solubilize BL05-HA in the micelle formulation.

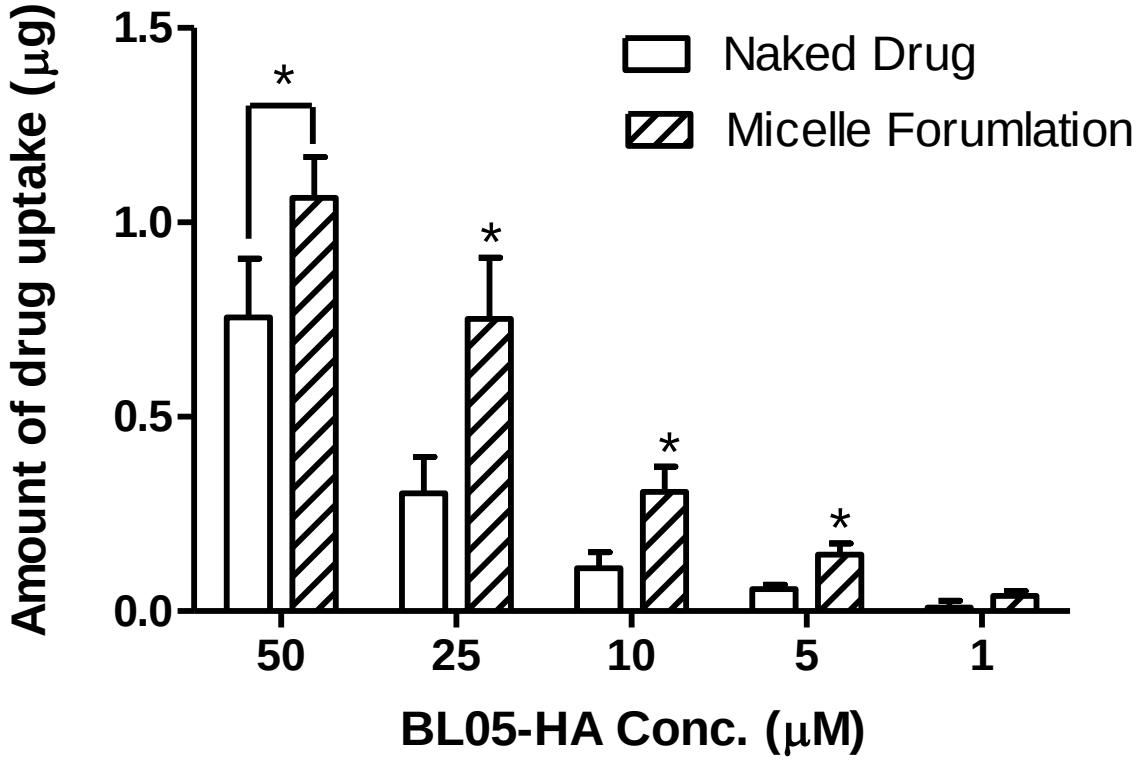

Fig. 7: The micelle formulation improved DU145's uptake of BL05-HA (Mean ± SD). (*: $p < 0.001$)

2.3.10 PSMAa10 targeting improved cellular uptake of both micelles and drug by PSMA-positive cells

LNCaP cells (PSMA +) were treated with PSMA-targeted and IR-820-labeled micelles with increasing substitutions of the aptamer. The micelle uptake was estimated by the relative fluorescence intensity of the IR-820. The fluorescence increased with increasing aptamer substitution: 1 %, 325 ± 103.410; 2.5 %, 574.554 ± 33.614; 5 %, 704.055 ± 73.235 and 10 %, 945.311 ± 145.445 RFU.

Confocal microscopy was used to examine if PSMA targeting can improve the micelle uptake by PSMA presenting cells. The aptamer did not improve the micelle uptake in the PSMA-negative PC3 cells. However, in the PSMA-positive LNCaP cells, we detected more fluorescence signal in cells treated with PSMA-targeted micelles (Fig. 8). The uptake was then quantified with a fluorescence plate reader. The fluorescence signal was significantly higher in PSMA-positive cells (LNCaP) treated with PSMA-targeted micelles. However, in PSMA-negative PC3 cells, the fluorescence was not enhanced by addition of PSMA to the micelles (Fig. 9).

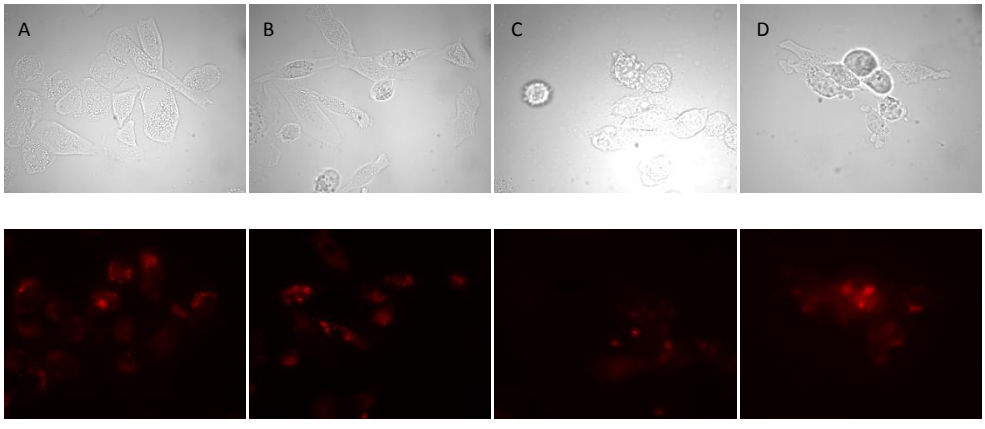

Fig. 8: Fluorescence imaging study of cell uptake of fluorescent PSMA-targeted micelles in PSMA-positive LNCaP cells. (A) PC3 cells treated with non-targeted micelles; (B) PC3 cells treated with PSMA-targeted micelles; (C) LNCaP cells treated with non-targeted micelles; (D) LNCaP cells treated with PSMA-targeted micelles.

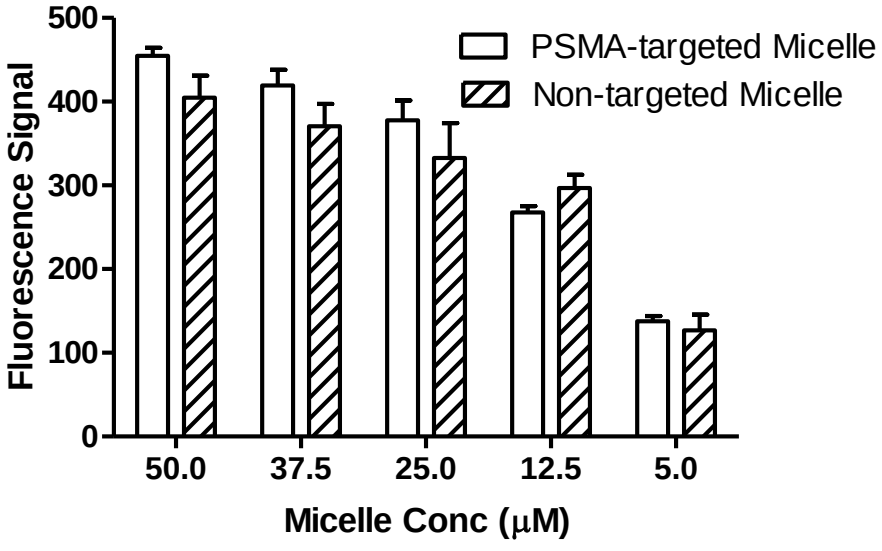

a

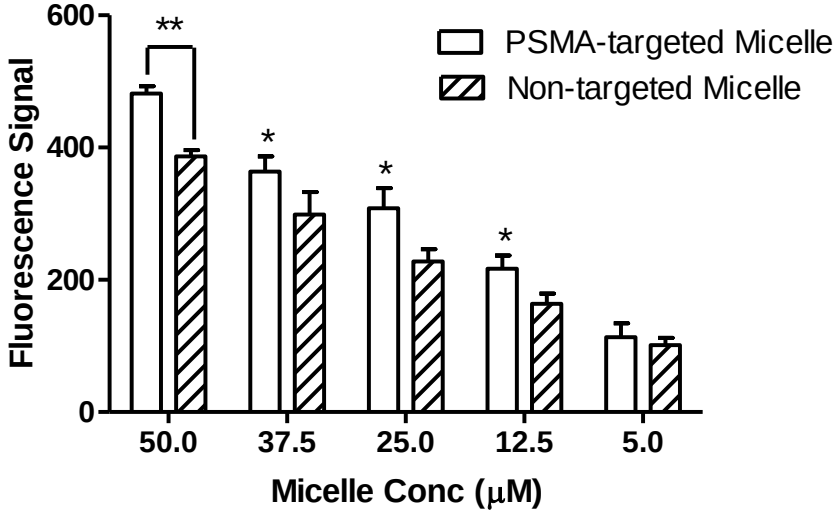

b

Fig. 9: Uptake of micelles by (a) PC3 cells; and (b) DU145 cells (Mean ± SD). (*: $p < 0.05$; **: $p < 0.01$)

The effect of PSMA-targeting of micelles on the cellular uptake of BL05-HA was examined in both DU145 (PSMA -) and LNCaP (PSMA +) cells (Fig. 7). PSMA-targeted micelles significantly improved the drug uptake in PSMA-positive LNCaP cells but not PSMA-negative DU145. In addition, BL05-HA formulated in PSMA-targeted micelles significantly reduced LNCaP cell viability compared to the naked drug, whereas BL05-HA in non-targeted micelles was no more effective than the naked drug. In PSMA negative cells, this significant effect was not observed (Fig. 11) ($p > 0.05$).

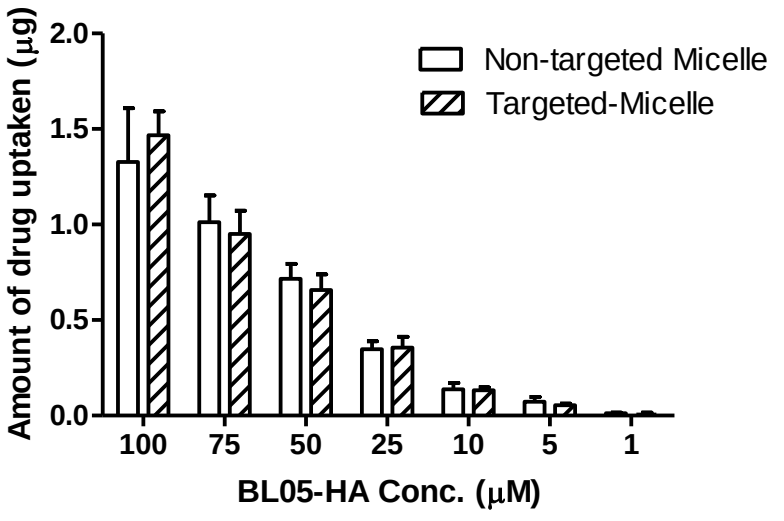

a

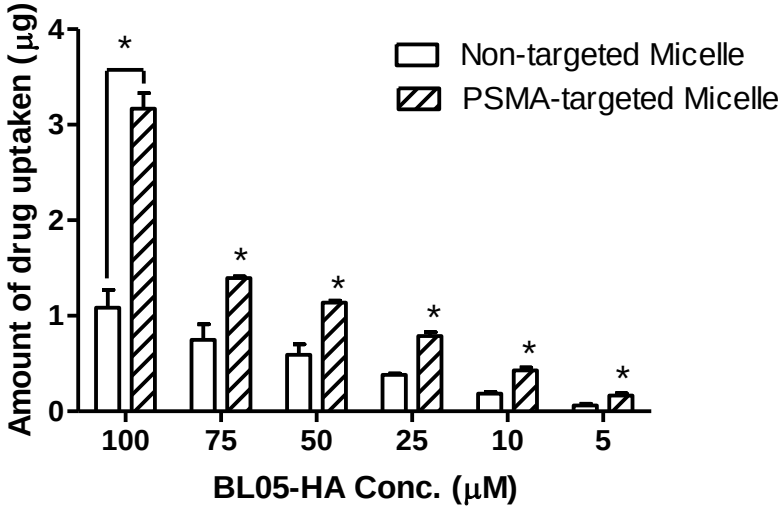

b

Fig. 10: PSMA-targeted micelles improved drug uptake by PSMA positive cells. Drug uptake by (a) PSMA-negative DU145 cells and (b) PSMA-positive LNCaP cells treated with targeted or non-targeted formulations (Mean ± SD). (*: $p < 0.001$)

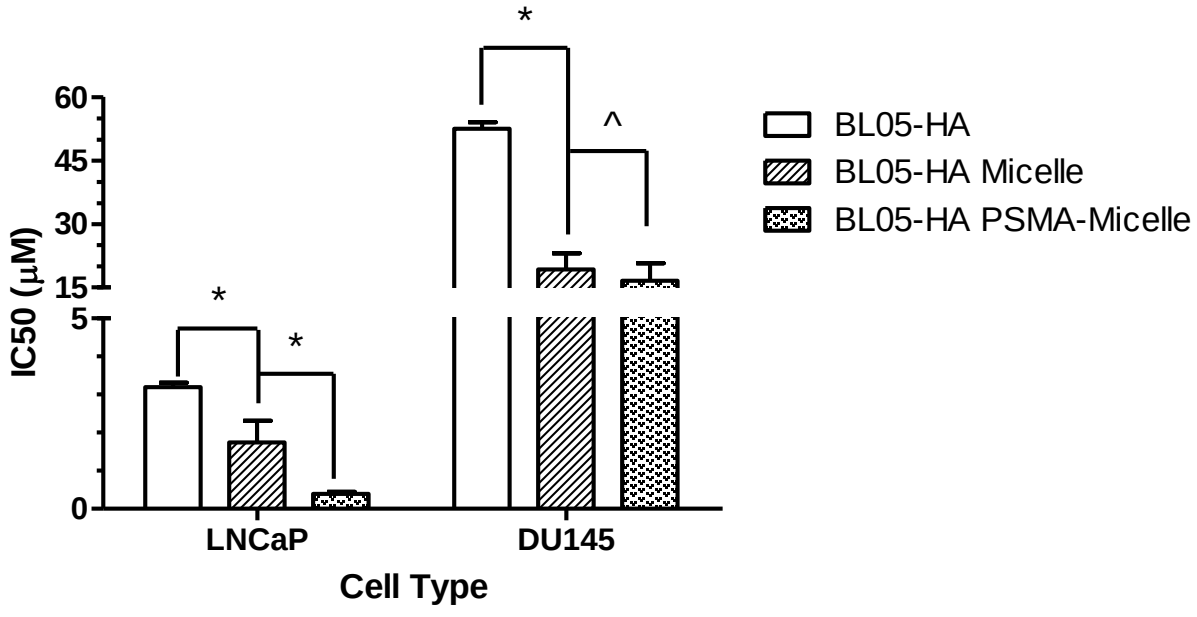

Fig. 11: IC50s of different formulations of BL05-HA in LNCaP and DU145 cells (Mean ± SE). (*: $p < 0.01$; ^: $p > 0.05$)

2.3.11 Pharmacokinetic evaluation

The pharmacokinetics of naked BL05-HA and BL05-HA formulated in PSMA-targeted micelles were compared in male Balb/c mice (n = 3). The initial drug plasma concentration (C_0) of the micelle formulation was 1.42-fold greater than the naked drug (Fig. 12). The plasma concentration of BL05 delivered by PSMA-targeted micelles was higher than the naked drug at all time points. A two-compartment pharmacokinetic model was selected to describe the biexponential nature of the pharmacokinetics disposition of PEG-PCL micelle formulation; whereas one-compartment model was used in BL05-HA naked drug and the related pharmacokinetic parameters are listed in Table 7. The area under the plasma concentration time curve ($AUC_{0\text{-}24h}$) of the micelle formulation was 2.27-fold greater than that of the naked drug and the concomitant total body clearance was 6.2-fold lower.

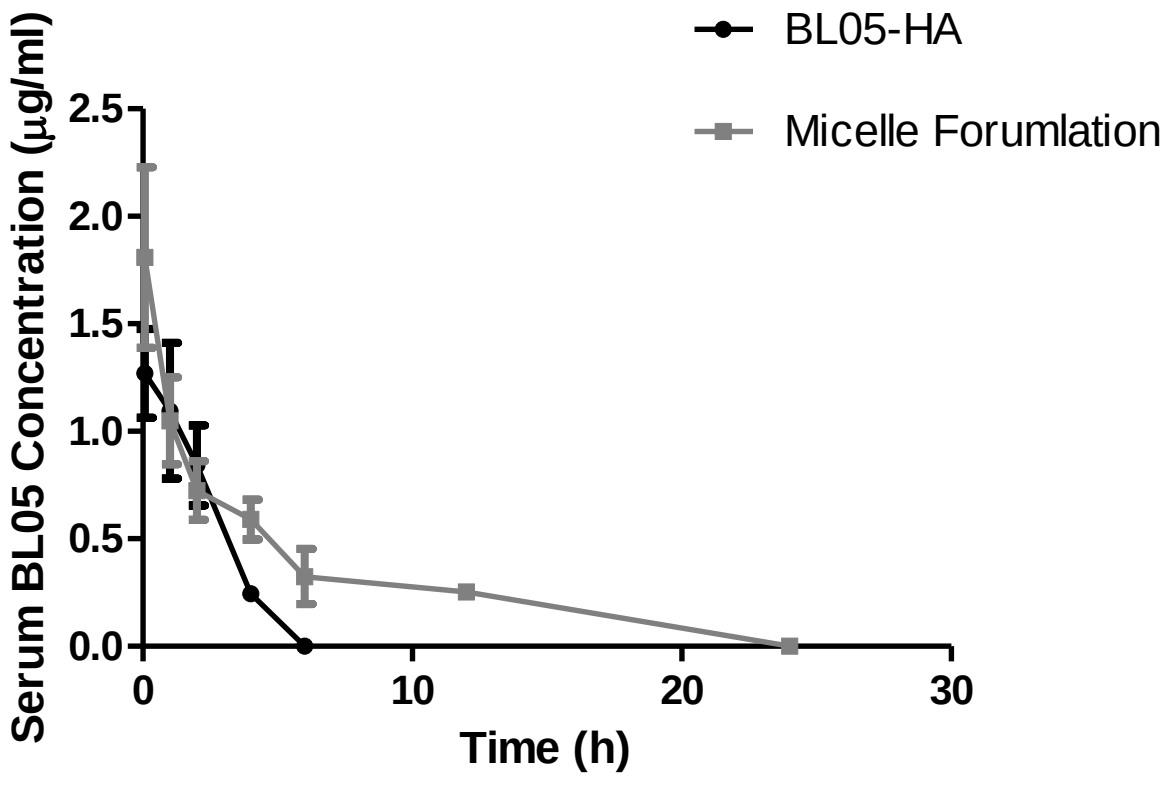

Fig. 12: Plasma BL05 concentration versus time disposition (Mean ± SD) (n = 3).

Table 7: Pharmacokinetic parameters after i.v. administration of BL05-HA loaded PSMA-targeted micelles and naked BL05-HA (Mean ± SD) (n = 3). (*: $p < 0.05$; **: $p < 0.01$; ***: $p < 0.001$)

Parameters	Unit	PSMA-targeted Micelle	Naked BL05-HA
V_d	$L \cdot kg^{-1}$	15.76 ± 2.01**	21.71 ± 2.42
C_0	$\mu g \cdot mL^{-1}$	1.95 ± 0.27*	1.41 ± 0.17
AUC_{0-24h}	$\mu g \cdot h \cdot mL^{-1}$	7.93 ± 0.45***	3.60 ± 0.21
k	h^{-1}	0.22 ± 0.02	0.337 ± 0.03
k_{12}	h^{-1}	0.71 ± 0.21	-
k_{21}	h^{-1}	0.98 ± 0.79	-
Cl	$mL \cdot min^{-1} \cdot kg^{-1}$	3.41 ± 0.25*	7.22 ± 0.38
$t_{1/2}$	h	7.84 ± 2.13**	2.08 ± 0.20
MRT	h	9.89 ± 1.89**	3.01 ± 0.29

2.3.12 Efficacy study in xenograft models

Tumor volume was calculated by length × width × 0.5 and tumor growth curves were generated by plotting the relative fold value of tumor volume at each time point comparing to their initial volume (set to value 1). As shown in Fig. 13, compared to the control, both PEG-PCL micelle-delivered TGX-221 analog BL05 and the naked BL05 significantly suppressed tumor growth in four cell lines-derived xenografts. The asterisk indicates a significant difference compared to the control (ANOVA analysis, $p < 0.01$).

Paraffin-embeded tumor sections from 22RV1 xenografts were subjected to immune-fluorescent staining with anti BrdU antibody followed by FITC-conjugated secondary antibody. Tumor sections were counter-stained with nuclear acid dye DAPI. Microscopic images were taken using Olympus fluorescent microscope (magnficaiton, 200×). As shown in Fig. 14, a dramatic decrease of immunofluorescent positive cells compared to the control group, indicating PEG-PCL micelle delivered BL05 suppressed tumor cell proliferation in xenograft models.

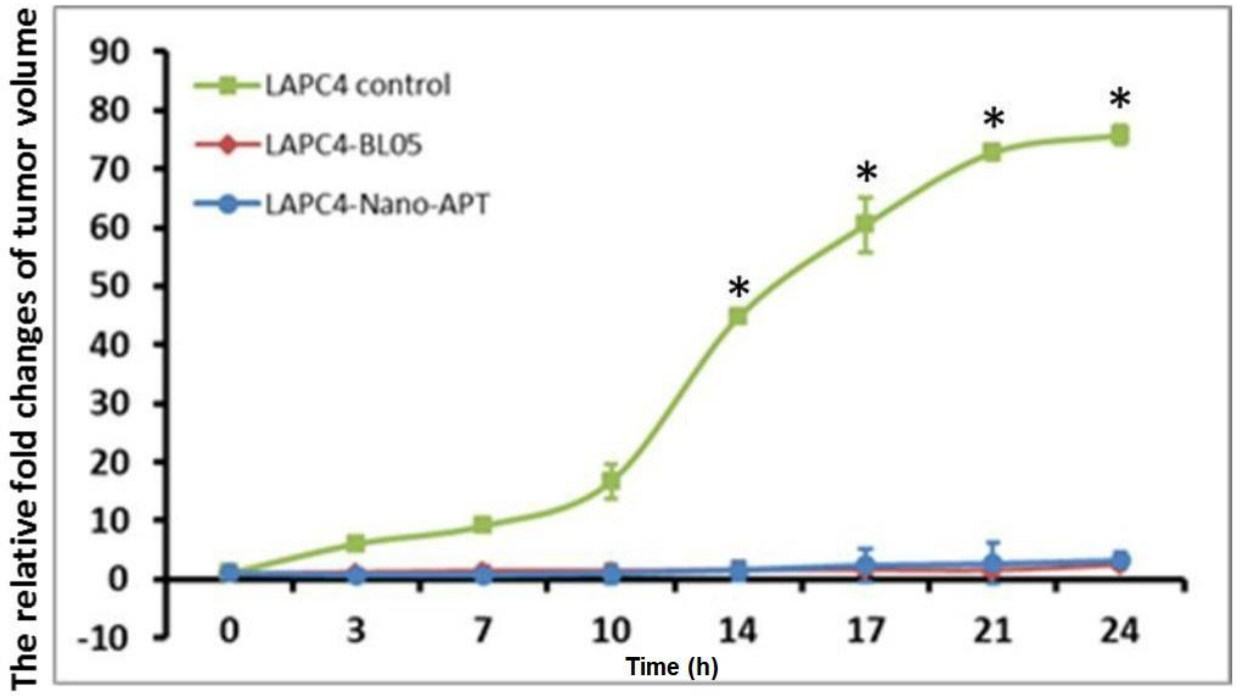
The relative fold changes of tumor volume
90
80
70
60
50
40
30
20
10
0
-10
0
3
7
10
14
17
21
24
Time (h)
LAPC4 control
LAPC4-BL05
LAPC4-Nano-APT
*
*
*
*

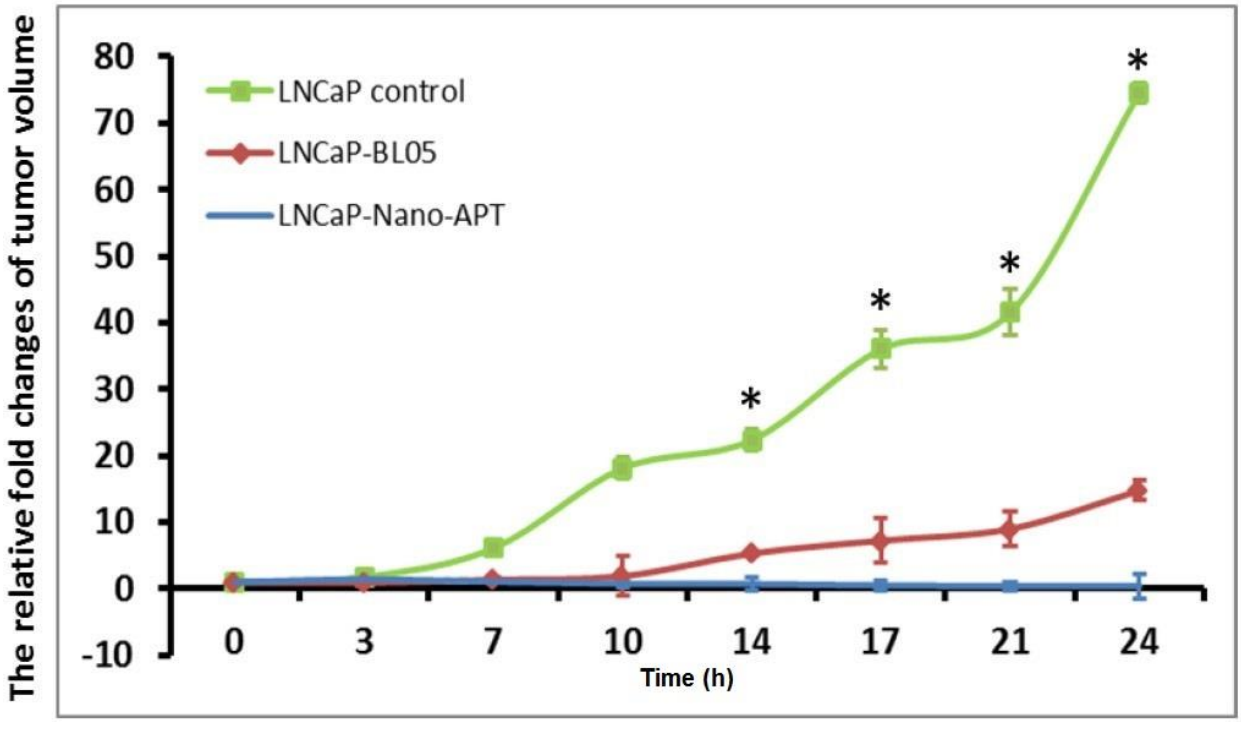
The relative fold changes of tumor volume
80
70
60
50
40
30
20
10
0
-10
0
3
7
10
14
17
21
24
Time (h)
LNCaP control
LNCaP-BL05
LNCaP-Nano-APT
*
*
*
*

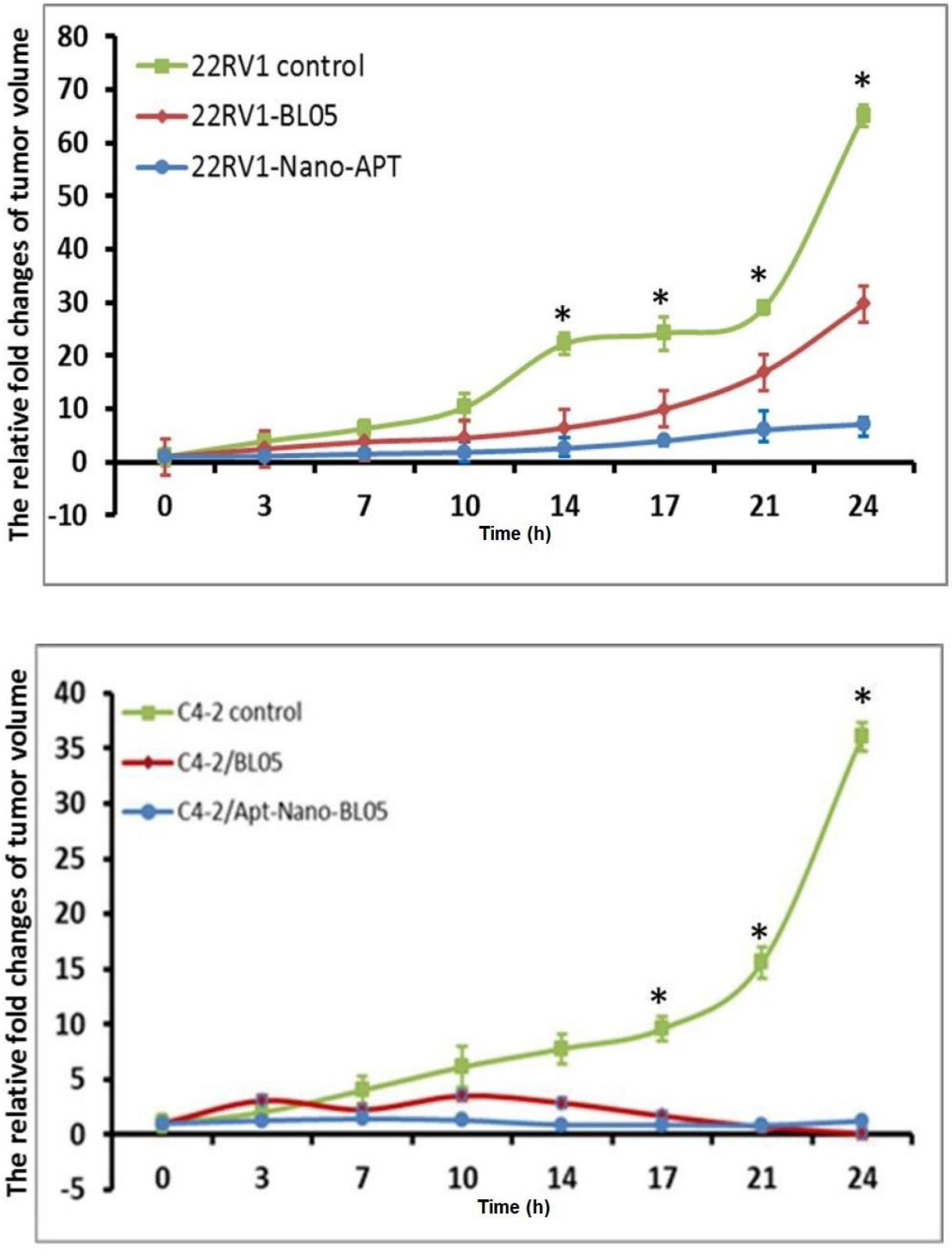

Fig. 13: PSMAa10-conjugated BL05-loaded PEG-PCL-micelles abolish tumor growth in prostate cancer xenograft models.

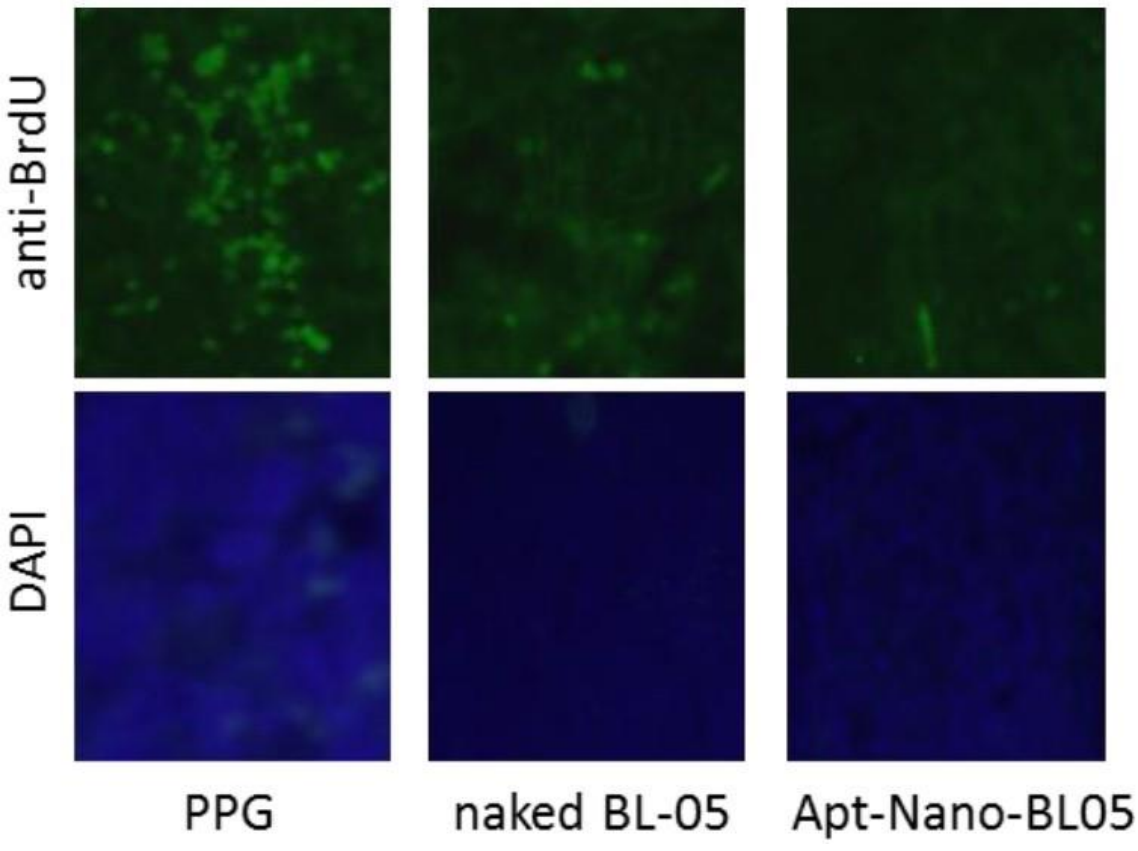

Fig. 14: BL05 loaded micelle reduced BrdU labeling in xenograft tumors.

2.4 Discussion

Prostate cancer is by far the most commonly diagnosed cancer among western males. Most anticancer drugs are administered intravenously or orally to achieve systemic distribution and the non-specific uptake of anticancer drugs may cause damage to healthy, rapidly dividing cells such as bone marrow and hair (35, 36). Nanoparticles can passively or actively target tumor tissue and minimize the side effects of conventional chemotherapies such as sexual dysfunction, cardiac toxicity, gastrointestinal damage, and neurotoxicity (37). The leaky endothelial vasculature of tumor tissues and the size properties of nanoparticles play a significant role in their passive targeting (38), due to the EPR effect. Improved targeting can be achieved by decorating the nanoparticle surface with a tumor specific targeting molecule such as a monoclonal antibody or nucleic acid (39). The tumor specific targeting molecules can bind to tumor cells and increase the intracellular concentration of the drug by receptor-mediated endocytosis. In this study, we formulated a prostate cancer cell-targeted nanocarrier that can enhance the efficacy of an encapsulated anticancer drug against prostate cancer cells and also optimize the pharmacokinetic disposition of the drug in a mouse model because of the encapsulated carrier. We targeted the carriers to prostate cells with the PSMA aptamer because this small ligand has nM affinities for the PSMA receptor, which is ubiquitous to clinical prostate cancers (40). We conjugated the ligand to pre-formed micelles. This approach is expected to result in a more homogenous distribution of the ligands among the nanoparticles than other approaches such as attaching ligands to the monomers before formation or drug encapsulation. The resulting triazole linker is also more resistant to hydrolytic and enzymatic cleavage than

esters or amides formed by carbodiimide chemistries.

TGX-221 showed selective cytotoxicity against LNCaP cells, which was consistent with a previous report (13). TGX-221 and its analog, BL05, showed similar toxicity in different prostate cancer cell lines, and Western blotting confirmed their inhibitory effects on phosphorylation of Akt in LNCaP cells. The modification of the aniline nitrogen did not affect the drug activity significantly, which is possible if only the morpholinechromone ring system and aniline structure contribute to the binding to PI3K beta subunit (41).

SLN is a novel approach to oral and parenteral drug delivery systems. Biological lipids have minimum carrier cytotoxicity, and the solid state of the lipid core permit better controlled drug release due to increase mass transfer resistance. SLN possess a solid lipid core matrix that can solubilize lipophilic molecules. The lipid core has to be stabilized by surfactants to reduce surface tension. This approach holds great promise for attaining bioavailability enhancement along with site specific drug delivery. In this study, a burst release of the drug was observed. This indicated that TGX-221 didn't incorporate to the lipid core very well. There are also some limitations of using SLN as a drug delivery carrier such as relatively low loading capacity and potential expulsion of the drug during storage. In addition, the highly purified lipid can crystallize in a more perfect crystalline lattice that leaves little room for the incorporation of the drugs.

To overcome the limitations of SLN, the concept of NLC was introduced. NLC possess many imperfections, thus increasing drug loading capacity and minimizing or avoiding drug expulsion during storage. In general, a solid lipid is mixed with a liquid lipid (oil). This blend is used to produce the lipid particles that are still solid at

temperatures up to about 40 °C. Our study showed that by using NLC, the *in vitro* release of the drug was partially improved. Nevertheless, the formulation was still not good enough for being used as a sustained and controlled release drug delivery carrier for TGX-221.

Synthetic polymers have been extensively researched as colloidal materials for nanoparticle production designed for drug delivery. PLGA polymer has been approved by FDA for human therapy. One commercially available drug delivery device using PLGA is Lupron Depot® for the treatment of advance prostate cancer. We tried to encapsulate TGX-221 to PLGA nanoparticles and we found that TGX-221 still could not be retained in this drug delivery carrier; therefore, a prodrug strategy was pursued.

Drug interaction and association with the hydrophobic core of the micelle can influence a drug's release rate (42). Both TGX-221 and BL05 did not stay in the hydrophobic core of PEG-PCL micelles, which may be due to the amphiphilic nature of these molecules. Therefore, the hydrophobic character of the drug was modified by the addition of hydrophobic fatty esters. The fatty acid prodrugs are susceptible to intra- and extra-cellular esterases and hydrolysis, so the parent drug is expected to reform rapidly after the drug is released from micelles. This addition increased the encapsulation efficiency leading to the postulation that the long carbon chain may also decrease the release rate due to the drug's more favorable interaction to the hydrophobic core (43, 44).

The *in vitro* cytotoxicity study showed that both PSMA-targeted and non-targeted empty micelles were not toxic to DU145 cells. This was expected since both PEG and PCL polymers are already FDA approved for use in humans and PSMAa10 is

made of a single stranded oligonucleotide. However, inhibitory effects were observed with IR-820 labeled PEG-PCL micelles. The toxic effect came from the dye, IR-820, which was reported to significantly inhibit cell growth at concentrations greater than 5 μM (34). Therefore, the IR-820 labeled non-targeted and targeted micelles were only used for examining delivery efficiency and not for further *in vivo* characterization.

Due to the change of partition and diffusion coefficients, BL05-HA may have lower membrane permeability compared to its parent drug, BL05, and TGX-221. Thus, the passive diffusion rate of the BL05-HA naked drug to the cells could be lower. The micelle formulation significantly improved cellular uptake of BL05-HA, which is consistent with the enhanced cellular uptake of drugs internalized witin PEG-PCL micelles (45).

We found that encapsulating BL05-HA within PSMA targeted PEG-PCL micelles increased cytotoxicity in LNCaP cells (PSMA positive) but not in PC3 cells (PSMA negative). This can be explained by the enhanced cellular uptake of the carrier by PSMA-positive cells through a receptor-mediated pathway. Cellular uptake of the naked drug is driven by a concentration gradient. After equilibrium is established, no more drugs can enter into the cells. The PEGylated surface of the micelles reduces interaction with the cell surface. Therefore, the cytotoxicities of naked drug and the untargeted drug-loaded micelles in LNCaP and PC3 cells were not significantly different. In PSMA positive cells, the receptor mediated transport of PSMA-targeted micelles improved drug delivery into cells, significantly enhancing cytotoxicity. Since the expression of PSMA on PSMA-negative cells was extremely low, the effect of PSMA-targeting was not significant ($p > 0.05$).

A two-compartment model was used to describe the pharmacokinetic (PK) disposition of the PEG-PCL micelle formulation. The PK profile showed that the plasma drug concentration declines biexponentially as the sum of distribution and elimination processes. The rapid drug concentration decrease in the initial phase was due to the drug's distribution from the central compartment into the peripheral compartments. Drug metabolism and excretion contributed to the gradual decrease in the plasma concentration during the beta phase. In the pharmacokinetics study, we have shown that the PEGylated micelles can increase the plasma AUC and detectable systemic circulation of the drug by avoiding clearance by the reticuloendothelial system (RES) and kidneys. The RES consists primarily of monocytes and macrophages in the spleen and liver that are responsible for clearing molecules bound with serum proteins. The kidneys clear unbound drugs, by glomerular filtration, below the renal exclusion limit of ca. 20-60 kDa. Stealth nanoparticles surface-modified with PEG can avoid clearance by the RES and kidneys, thus they have prolonged circulation half-lives in the plasma (46). This approach has been used to optimize pharmacokinetic disposition of nanoparticles and enhance drug delivery (46, 47). In this study, the high V_d value of naked BL05-HA may be due to its high tissue distribution. A rapid total body clearance rate is also apparent. The micelle formulation significantly reduced the V_d by minimizing non-specific tissue distribution and the drug was consequently retained within the vascular system. This could also reduce toxicity to normal tissues by reducing their exposure to the drug through non-specific distribution.

The combination of androgen ablation (hormone therapy) along with early detection and surgery has made prostate cancer highly treatable at the initial stage.

However, this cancer remains the second leading cause of cancer death among American men. Our collaborator has demonstrated that the PI3K p110beta isoform, a major cellular signaling molecule, is critical for prostate cancer progression in cell culture models and mouse xenograft models (48).

In animal subcutaneous xenograft experiments, the solvent PPG, naked TGX-221 analog BL05 and BL05 prodrug (BL05-HA) loaded micelles were used. The maximum tolerable dose of BL05 as a naked drug in PPG or encapsulated in a PSMAa10-conjugated micelles were given twice a week by tail vein injection. Our data revealed that PSMAa10 conjugation of the BL05-HA completely abolished tumor growth of prostate xenograft tumors derived from all four prostate cancer cell lines, both androgen-responsive and non-responsive cell lines. Similarly, naked BL05 treatment also blocked tumor growth in LAPC-4 and C4-2-derived xenografts, although in animals with LNCap or 22RV1-derived xenografts, a slight increase of tumor volume was noticed after 3 weeks. The immunofluorescent staining revealed a reduced anti-BrdU labeling in PEG-PCL micelle treated xenografts compared to tumors in the control or naked BL05 groups. These data strongly suggested that TGX-221 and its analog possess a potent anti-tumor effect and PSMA-mediated targeting greatly enhances its potency over naked drugs.

2.5 Conclusions

The synthesis of TGX-221, the analog BL05, and the BL05-HA and BL05-PA prodrugs were successfully accomplished. Both TGX-221 and its analog BL05 had an inhibitory effect on the phosphatation of PIP3 in PTEN-deficient LNCaP cells. Compared to SLN, NLC and PLGA nanoparticles, micelle formulation gave the smallest particle size, which is better for intravenous administration. Encapsulation

of BL05-HA in PEG-PCL micelles resulted in sustained release over several days. *In vitro*, we have shown that micelles targeted with PSMAa10 and loaded with BL05-HA significantly inhibits the growth of PSMA-positive prostate cancer cells, but not PSMA-negative cells. *In vivo* pharmacokinetics demonstrated that PSMA-targeted micelles significantly increased the AUC and decreased the total body clearance rate of the drug. Moreover, the PSMA-targeted micelle formulation of TGX-221 analog, BL05, significantly suppressed tumor growth in all four cell lines'-derived xenografts. These findings suggested that PSMA-targeted micelles are a promising drug delivery vehicle for developing PI3-kinase inhibitor treatments of PSMA positive prostate cancers.

2.6 References

1. L.S. Steelman, W.H. Chappell, S.L. Abrams, R.C. Kempf, J. Long, P. Laidler, S. Mijatovic, D. Maksimovic-Ivanic, F. Stivala, M.C. Mazzarino, M. Donia, P. Fagone, G. Malaponte, F. Nicoletti, M. Libra, M. Milella, A. Tafuri, A. Bonati, J. Basecke, L. Cocco, C. Evangelisti, A.M. Martelli, G. Montalto, M. Cervello, and J.A. McCubrey. Roles of the Raf/MEK/ERK and PI3K/PTEN/Akt/mTOR pathways in controlling growth and sensitivity to therapy-implications for cancer and aging. Aging. 3:192-222 (2011).
2. H.A. Dboukand J.M. Backer. A beta version of life: p110beta takes center stage. Oncotarget. 1:729-733 (2010).
3. M. Qiao, S. Sheng, and A.B. Pardee. Metastasis and AKT activation. Cell Cycle. 7:2991-2996 (2008).
4. S. Zhangand D. Yu. PI(3)king apart PTEN's role in cancer. Clin Cancer Res. 16:4325-4330 (2010).

5. P.W. van Duijn, A.C. Ziel-van der Made, J.A. van der Korput, and J. Trapman. PTEN-mediated G1 cell-cycle arrest in LNCaP prostate cancer cells is associated with altered expression of cell-cycle regulators. The Prostate. 70:135-146 (2010).

6. N. Pore, S. Liu, D.A. Haas-Kogan, D.M. O'Rourke, and A. Maity. PTEN mutation and epidermal growth factor receptor activation regulate vascular endothelial growth factor (VEGF) mRNA expression in human glioblastoma cells by transactivating the proximal VEGF promoter. Cancer research. 63:236-241 (2003).

7. L.E. Ramehand L.C. Cantley. The role of phosphoinositide 3-kinase lipid products in cell function. J Biol Chem. 274:8347-8350 (1999).

8. S. Jia, T.M. Roberts, and J.J. Zhao. Should individual PI3 kinase isoforms be targeted in cancer? Current opinion in cell biology. 21:199-208 (2009).

9. S. Jia, Z. Liu, S. Zhang, P. Liu, L. Zhang, S.H. Lee, J. Zhang, S. Signoretti, M. Loda, T.M. Roberts, and J.J. Zhao. Essential roles of PI(3)K-p110beta in cell growth, metabolism and tumorigenesis. Nature. 454:776-779 (2008).

10. L.C. Foukas, I.M. Berenjeno, A. Gray, A. Khwaja, and B. Vanhaesebroeck. Activity of any class IA PI3K isoform can sustain cell proliferation and survival. Proc Natl Acad Sci U S A. 107:11381-11386 (2010).

11. C. Billottet, L. Banerjee, B. Vanhaesebroeck, and A. Khwaja. Inhibition of class I phosphoinositide 3-kinase activity impairs proliferation and triggers apoptosis in acute promyelocytic leukemia without affecting atra-induced differentiation. Cancer research. 69:1027-1036 (2009).

12. S.P. Jackson, S.M. Schoenwaelder, I. Goncalves, W.S. Nesbitt, C.L. Yap, C.E. Wright, V. Kenche, K.E. Anderson, S.M. Dopheide, Y. Yuan, S.A. Sturgeon, H. Prabaharan, P.E. Thompson, G.D. Smith, P.R. Shepherd, N. Daniele, S. Kulkarni, B. Abbott, D. Saylik, C. Jones, L. Lu, S. Giuliano, S.C. Hughan, J.A. Angus, A.D. Robertson, and H.H. Salem. PI 3-kinase p110beta: a new target for antithrombotic therapy. Nat Med. 11:507-514 (2005).

13. W. Tai, R.S. Shukla, B. Qin, B. Li, and K. Cheng. Development of a peptide-drug conjugate for prostate cancer therapy. Mol Pharm. 8:901-912 (2011).

14. A. Laurent, F. Mottu, R. Chapot, J.Q. Zhang, O. Jordan, D.A. Rufenacht, E. Doelker, and J.J. Merland. Cardiovascular effects of selected water-miscible solvents for pharmaceutical injections and embolization materials: a comparative hemodynamic study using a sheep model. PDA J Pharm Sci Technol. 61:64-74 (2007).

15. P. Sampathand H. Brem. Implantable Slow-Release Chemotherapeutic Polymers for the Treatment of Malignant Brain Tumors. Cancer Control. 5:130-137 (1998).

16. M.E. Davis, Z.G. Chen, and D.M. Shin. Nanoparticle therapeutics: an emerging treatment modality for cancer. Nat Rev Drug Discov. 7:771-782 (2008).

17. A.K. Jain, M. Das, N.K. Swarnakar, and S. Jain. Engineered PLGA nanoparticles: an emerging delivery tool in cancer therapeutics. Crit Rev Ther Drug Carrier Syst. 28:1-45 (2011).

18. J. Grimmand D.A. Scheinberg. Will nanotechnology influence targeted cancer therapy? Semin Radiat Oncol. 21:80-87 (2011).

19. J.L. Arias. Drug targeting strategies in cancer treatment: an overview. Mini Rev Med Chem. 11:1-17 (2011).

20. R.N. Saha, S. Vasanthakumar, G. Bende, and M. Snehalatha. Nanoparticulate drug delivery systems for cancer chemotherapy. Mol Membr Biol. 27:215-231 (2010).

21. C. Gong, X. Wei, X. Wang, Y. Wang, G. Guo, Y. Mao, F. Luo, and Z. Qian. Biodegradable self-assembled PEG-PCL-PEG micelles for hydrophobic honokiol delivery: I. Preparation and characterization. Nanotechnology. 21:215103 (2010).

22. A.M. Master, M.E. Rodriguez, M.E. Kenney, N.L. Oleinick, and A.S. Gupta. Delivery of the photosensitizer Pc 4 in PEG-PCL micelles for in vitro PDT studies. J Pharm Sci. 99:2386-2398 (2010).

23. R. Li, X. Li, L. Xie, D. Ding, Y. Hu, X. Qian, L. Yu, Y. Ding, X. Jiang, and B. Liu. Preparation and evaluation of PEG-PCL nanoparticles for local tetradrine delivery. Int J Pharm. 379:158-166 (2009).

24. H. Bramfeldt, P. Sarazin, and P. Vermette. Characterization, degradation, and mechanical strength of poly(D,L-lactide-co-epsilon-caprolactone)-poly(ethylene glycol)-poly(D,L-lactide-co-epsilon-caprolactone). J Biomed Mater Res A. 83:503-511 (2007).

25. H. Zhang. Quantum dot-A10 RNA aptamer-doxorubicin conjugate. Molecular Imaging and Contrast Agent Database (MICAD), Bethesda (MD), 2004.

26. A. Chaux, J. Eifler, S. Karram, T. Al-Hussain, S. Faraj, M. Pomper, R. Rodriguez, and G.J. Netto. Focal positive prostate-specific membrane antigen (PSMA) expression in ganglionic tissues associated with prostate neurovascular bundle: Implications for novel intraoperative PSMA-based fluorescent imaging techniques. Urol Oncol (2011).

27. A. Baccala, L. Sercia, J. Li, W. Heston, and M. Zhou. Expression of prostate-specific membrane antigen in tumor-associated neovasculature of renal neoplasms. Urology. 70:385-390 (2007).

28. J.L. Gala, S. Loric, Y. Guiot, S.R. Denmeade, A. Gady, F. Brasseur, M. Heusterspreute, P. Eschwege, P. De Nayer, P. Van Cangh, and B. Tombal. Expression of prostate-specific membrane antigen in transitional cell carcinoma of the bladder: prognostic value? Clin Cancer Res. 6:4049-4054 (2000).

29. K.W. Thieland P.H. Giangrande. Intracellular delivery of RNA-based therapeutics using aptamers. Ther Deliv. 1:849-861 (2010).

30. B.A. Prasadand S.R. Gilbertson. One-pot synthesis of unsymmetrical N-heterocyclic carbene ligands from N-(2-iodoethyl)arylamine salts. Org Lett. 11:3710-3713 (2009).

31. E. Pierriand K. Avgoustakis. Poly(lactide)-poly(ethylene glycol) micelles as a carrier for griseofulvin. J Biomed Mater Res A. 75:639-647 (2005).

32. K.K. Jette, D. Law, E.A. Schmitt, and G.S. Kwon. Preparation and drug loading of poly(ethylene glycol)-block-poly(epsilon-caprolactone) micelles through the evaporation of a cosolvent azeotrope. Pharm Res. 21:1184-1191 (2004).

33. P. Decuzzi, R. Pasqualini, W. Arap, and M. Ferrari. Intravascular delivery of particulate systems: does geometry really matter? Pharm Res. 26:235-243 (2009).

34. V.V. Mody, R. Siwale, A. Singh, and H.R. Mody. Introduction to metallic nanoparticles. J Pharm Bioallied Sci. 2:282-289 (2010).

35. J. Sitzia, C. North, J. Stanley, and N. Winterberg. Side effects of CHOP in the treatment of non-hodgkin's lymphoma. Cancer Nurs. 20:430-439 (1997).

36. J.N. Yuan, Y. Chao, W.P. Lee, C.P. Li, R.C. Lee, F.Y. Chang, S.H. Yen, S.D. Lee, and J. Whang-Peng. Chemotherapy with etoposide, doxorubicin, cisplatin, 5-fluorouracil, and leucovorin for patients with advanced hepatocellular carcinoma. Med Oncol. 25:201-206 (2008).

37. M. Chidambaram, R. Manavalan, and K. Kathiresan. Nanotherapeutics to overcome conventional cancer chemotherapy limitations. J Pharm Pharm Sci. 14:67-77 (2011).

38. K. Cho, X. Wang, S. Nie, Z.G. Chen, and D.M. Shin. Therapeutic nanoparticles for drug delivery in cancer. Clin Cancer Res. 14:1310-1316 (2008).

39. D. Peer, J.M. Karp, S. Hong, O.C. Farokhzad, R. Margalit, and R. Langer. Nanocarriers as an emerging platform for cancer therapy. Nat Nanotechnol. 2:751-760 (2007).

40. C. Marchal, M. Redondo, M. Padilla, J. Caballero, I. Rodrigo, J. Garcia, J. Quian, and D.G. Boswick. Expression of prostate specific membrane antigen (PSMA) in prostatic adenocarcinoma and prostatic intraepithelial neoplasia. Histology and histopathology. 19:715-718 (2004).

41. M. Frazzetto, C. Suphioglu, J. Zhu, O. Schmidt-Kittler, I.G. Jennings, S.L. Cranmer, S.P. Jackson, K.W. Kinzler, B. Vogelstein, and P.E. Thompson. Dissecting isoform selectivity of PI3K inhibitors: the role of non-conserved residues in the catalytic pocket. Biochem J. 414:383-390 (2008).

42. L.L. Patrick Lim Soo, Dusica Maysinger, Adi Eisenberg. Incorporation and Release of Hydrophobic Probes in Biocompatible Polycaprolactone-block-poly(ethylene oxide) Micelles: Implications for Drug Delivery. Langmuir. 18:9996-10004 (2002).

43. M.L. Forrest, C.Y. Won, A.W. Malick, and G.S. Kwon. In vitro release of the mTOR inhibitor rapamycin from poly(ethylene glycol)-b-poly(epsilon-caprolactone) micelles. J Control Release. 110:370-377 (2006).

44. M.L. Forrest, A. Zhao, C.Y. Won, A.W. Malick, and G.S. Kwon. Lipophilic prodrugs of Hsp90 inhibitor geldanamycin for nanoencapsulation in poly(ethylene glycol)-b-poly(epsilon-caprolactone) micelles. J Control Release. 116:139-149 (2006).

45. Y.Y. Diao, H.Y. Li, Y.H. Fu, M. Han, Y.L. Hu, H.L. Jiang, Y. Tsutsumi, Q.C. Wei, D.W. Chen, and J.Q. Gao. Doxorubicin-loaded PEG-PCL copolymer micelles enhance cytotoxicity and intracellular accumulation of doxorubicin in adriamycin-resistant tumor cells. Int J Nanomedicine. 6:1955-1962 (2011).

46. S.D. Liand L. Huang. Nanoparticles evading the reticuloendothelial system: role of the supported bilayer. Biochim Biophys Acta. 1788:2259-2266 (2009).

47. I. Ozcan, F. Segura-Sanchez, K. Bouchemal, M. Sezak, O. Ozer, T. Guneri, and G. Ponchel. Pegylation of poly(gamma-benzyl-L-glutamate) nanoparticles is efficient for avoiding mononuclear phagocyte system capture in rats. Int J Nanomedicine. 5:1103-1111 (2010).

48. Q. Zhu, H. Youn, J. Tang, O. Tawfik, K. Dennis, P.F. Terranova, J. Du, P. Raynal, J.B. Thrasher, and B. Li. Phosphoinositide 3-OH kinase p85alpha and p110beta are essential for androgen receptor transactivation and tumor progression in prostate cancers. Oncogene. 27:4569-4579 (2008).

Chapter 3

Pharmacokinetic Evaluation of a DSPE-PEG$_{2000}$ Micellar Formulation of Ridaforolimus in Rat

3.1 Introduction

Ridaforolimus, also known as deforolimus, AP-23573, and MK8669, is a non-prodrug rapamycin analog (Fig. 1A). It is a large lipophilic (MW: 990 g/mol; XlogP: 5.9) carboxylic lactone-lactam macrolide antibiotic with potent anti-proliferative and immunosuppressive effects. Ridaforolimus inhibits the mammalian target of rapamycin (mTOR), a serine/threonine kinase that is expressed throughout most mammalian cells and that is involved in a variety of cell signaling cascades (1). Inappropriate activation of mTOR has been implicated in the pathogenesis of a range of cancers and can account for tumor proliferation and growth (1). Ridaforolimus has been shown to inhibit mTOR and has demonstrated anti-proliferative activity against several cancer types *in vitro* and *in vivo* (2).

Ridaforolimus is currently undergoing numerous clinical trials for a range of cancers both as a monotherapy and in combination with other chemotherapeutics including a Phase III clinical trial for metastatic soft-tissue and bone sarcoma. Formulations being evaluated in these clinical trials include an intravenous formulation given as an infusion and an oral formulation. The pharmacokinetic results from these studies suggest ridaforolimus follows non-linear kinetics following oral and intravenous administration as indicated by non-linear increases in area under the curve (AUC) and concentration maximum (C_{max}) with increases in dose (3). Changes in clearance (Cl) and volume of distribution at steady state (V_{ss}) are also reported to change with dose (3). It has been suggested that this nonlinearity is consistent with saturation of the red blood cell compartment which contains a substantial amount of FKBP-12, the binding protein of ridaforolimus and other

A

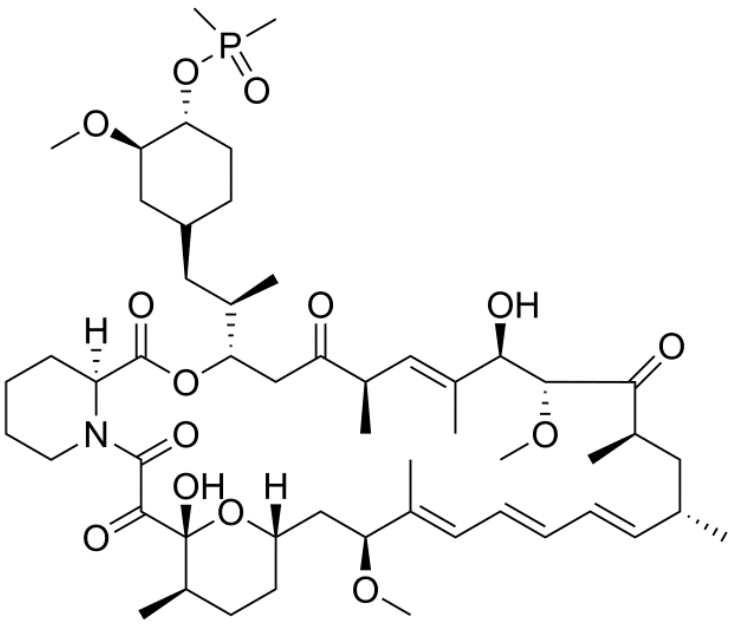

B

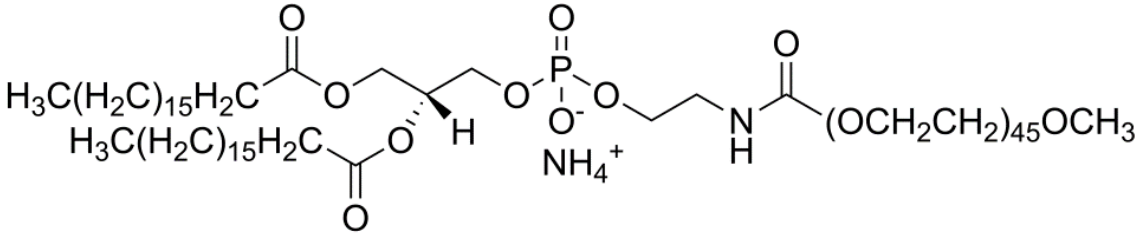

Fig. 1: Chemical structure of (A) ridaforolimus and (B) DSPE-PEG$_{2000}$

rapamycin analogs (4). This strong partitioning of ridaforolimus to the red blood cell compartment may hinder the accessibility of ridaforolimus into solid tumor sites (5).

Ridaforolimus and other derivatives of rapamycin including temsirolimus and everolimus differ from rapamycin at the C-42 position. In the case of ridaforolimus, the C-42 position consists of a dimethylphosphinate substitution, which increases the aqueous solubility of ridaforolimus (ca. 200 µg/mL) in comparison to rapamycin (ca. 2.6 µg/mL). Although improved in relation to rapamycin, the solubility of ridaforolimus is still poor and has likely hindered development of clinical intravenous formulations. This cannot be verified, however, as the only formulation information published to our knowledge includes that of animal studies where ridaforolimus was solubilized in a complicated vehicle of dimethyl acetamide/polysorbate 80/polyethylene glycol-400/water (10/10/40/40 v/v/v/v) (6).

Further increasing the solubility of ridaforolimus through the use of nanocarrier technology may decrease the amount of ridaforolimus that partitions to the erythrocyte compartment and thereby allow for easier prediction of pharmacokinetic parameters. A specific class of nanocarriers that has a large solubilization capacity for poorly water soluble molecules are the pegylated phospholipid (PPL) micelles (7). These self-assembled micelles are capable of solubilizing a wide range of hydrophobic molecules, and they are a potential tool for the safe formulation and delivery of antitumor agents to tumors without the inclusion of potentially harmful surfactants and excipients (5, 7, 8). Due to their nanoscopic dimensions (typically < 70 nm), PPL micelles can leave leaky vasculature, accumulating in tumors via the enhanced permeability and retention effect (EPR), where they remain due to poor

lymphatic clearance (7). An outer coat of poly(ethylene glycol) (PEG) imparts "stealth" characteristics to micelles, allowing them to circulate for long periods of time and avoid the mononuclear phagocyte system (MPS). These effects potentially reduce non-specific toxicities of the chemotherapeutic. Therefore, encapsulation of ridaforolimus in a micelle nanocarrier may limit its systemic toxicities specifically its dose-limiting toxicity of mucositis (3).

Previous investigations have confirmed that micelle formulations of poly(ethylene glycol)-block-poly(caprolactone) (PEG-b-PCL) can substantially increase the solubility and circulation time of rapamycin, while also greatly reducing the non-specific toxicity (5). We hypothesize that encapsulation of ridaforolimus in the PPL micelle polymer 1,2-distearoyl-*sn*-glycero-3-phosphoethanolamine-*N*-methoxy-poly(ethylene glycol 2000) (DSPE-PEG_{2000}) may allow for improved solubility while limiting the partition to erythrocytes. DSPE-PEG_{2000} (Fig. 1B); was chosen due to its promising kinetic and thermodynamic stability and biocompatibility DSPE-PEG_{2000} has received regulatory approval in the US and/or Europe in three formulations of doxorubicin (Doxil, LipoDox and Thermodox). Herein, we report the pharmacokinetics of a DSPE-PEG_{2000} formulation of ridaforolimus in rats. To our knowledge, this is the first report of the pharmacokinetics of ridaforolimus in rats and the first attempt to solubilize ridaforolimus in any type of nanocarrier.

3.2 Materials and Methods

3.2.1 Chemical and reagents

Ridaforolimus was purchased from LC Labs (Woburn, WA, USA). 1,2-distearoyl-sn-glycero-3-phosphoethanolamine-N-[methoxy(polyethylene glycol)-2000] (DSPE-PEG_{2000}) copolymer was purchased from Avanti Polar Lipids (Alabaster, Alabama, USA). HPLC-grade methanol and water were purchased from J.T. Baker (Philipsburg, NJ, USA). Other chemicals were of analytical grade. Healthy male Sprague-Dawley rats were obtained from Simonsen Labs (Gilroy, CA, USA). Ethical approval for animal experiments was obtained from Institutional Animal Care and Use Committee of Washington State University.

3.2.2 Preparation of drug formulations

Ridaforolimus loaded micelles were prepared by solvent evaporation technique. Specifically, ridaforolimus and DSPE-PEG_{2000} (Avanti Polar Lipids, Inc.) were solubilized in 1:1 acetone and methanol. The solution was then added in a drop-wise fashion to vigorously stirred ddH_2O using a syringe pump. The organic solvent was removed by stirring under an air purge. Solutions were then filtered through a 0.22-μm polyestersulfone filter to sterilize and remove unincorporated drug. Solutions were protected from light and stored at 4 °C until administered.

A control formulation for intravenous administration of ridaforolimus was made by dissolving ridaforolimus in ethanol followed by addition to PEG_{400} to form a

final formulation of 1:1 ethanol:PEG. The resulting mixture was vortexed until clear and passed through a 0.22-µm polyestersulfone filter.

Formulation concentrations were determined using a Shimadzu LC-2010A (Kyoto, Japan). A Phenomenex® Luna C_{18} (2) analytical column (250 x 4.6 mm; 5 µm) was used with UV detection at 290 nm (CA, USA). The mobile phase consisted of acetonitrile, water and formic acid (30:70:0.04, v/v/v) that was filtered and degassed prior to use with isocratic separation carried out at a flow rate of 0.3 mL/min. Hydrodynamic diameters of DSPE-PEG_{2000} micelles were performed using Dynamic Light Scattering (DLS) with a Malvern Nano ZS instrument and DTS software (Malvern Instruments Ltd, Malvern, Worcestershire, UK).

3.2.3 Micelle characterization

The formation of DSPE-PEG_{2000} micelles was determined by gel permeation chromatography (GPC) using a Shimadzu 2010CHT system with 0.8 ml/min ddH_2O as the mobile phase on a Shodex OHpak-803 HQ column (Showa Denko America, NY) thermostated at 40 °C. An evaporative light scattering detector (ELSD-LTII, Shimadzu, Lenexa, KS) was used to detect the particles. Narrow molecular weight distribution polyethylene glycols (Scientific Polymer Products, Ontario, NY) were used as standards for GPC analysis. To confirm the drug was encapsulated in the micelles, GPC peak fractions were collected and dried by Speed-Vap. The dried micelle fractions were re-dissolved in methanol and then analyzed by reversed-phase HPLC.

The drug loading efficiency (DL %) and encapsulation efficiency (EE %) of ridaforolimus in DSPE-PEG_{2000} micelles were calculated according to the following equations:

$$\text{DL}\ \% = \frac{\text{weight of the drug in micelle}}{\text{weight of the polymer and drug}} \times 100\ \% \quad (1)$$

$$\text{EE}\ \% = \frac{\text{weight of the drug in micelle}}{\text{weight of the feed drug}} \times 100\ \% \quad (2)$$

The *in vitro* release of the drug from DSPE-PEG_{2000} micelles into PBS (pH 7.4) was done by a dialysis method. Dialysis was carried out at 37 °C under sink condition using a 10-kDa MWCO dialysis tubing (SnakeSkin®, Thermo Scientific Inc., Rockford, IL). The initial volume of drug-loaded micelles in the dialysis tubing was 2 mL and the sink solution was 4 L. The PBS was changed several times per day to maintain sink conditions. After pre-determined time intervals, samples were withdrawn from the dialysis bag and analyzed by a reversed phase HPLC column (TSK-GEL ® ODS-100Z, Tosoh Bioscience) at 50 °C with UV detection at 290 nm.

3.2.4 Cellular uptake of DSPE-PEG_{2000} micelles

Prostate cancer cell line, DU145, was maintained in RPMI-1640 medium and head and neck cancer cell line, MDA-1986, was kept in Dulbecco Modified Eagle Medium (DMEM). Both medium were supplemented with 10 % fetal bovine serum (Hyclone Laboratory Inc., Logan, Utah). Cells were plated in 96-well flat-bottomed plates at a concentration of 10,000 cells per 90 µL of growth medium.

After the cells attached to the surface, ridaforolimus dissolved in DMSO or encapsulated in DSPE-PEG_{2000} micelles was added at concentrations of 0, 5, 10, 25, 50 μM. After a 6-h treatment, the cell culture medium was removed and analyzed for extracellular drug content by HPLC.

3.2.5 LC/MS analysis of Ridaforolimus

The LC/MS system was a Shimadzu LCMS-2010 EV liquid chromatograph mass spectrometer system (Kyoto, Japan) connected to the LC portion consisting of two LC-10AD pumps, a SIL-10AD VP auto injector, a SPD-10A VP UV detector, and a SCL-10A VP system controller was used. Data analysis was accomplished using Shimadzu LCMS Solutions Version 3 software. A Phenomenex® Luna C_{18} (2) analytical column (250 x 4.6 mm; 5 μm) was used with a mobile phase of methanol, water, and formic acid (90:10:0.1, v/v/v) modified with 2 mM ammonium acetate at a flow rate of 0.5 mL/min. Pterostilbene was used as an internal standard. Positive selective ion monitoring (SIM) was used for detection of ridaforolimus at m/z 1012.60 (sodium adduct) and pterostilbene at m/z 257. Sodium adduct formation of other immunosuppressants have been reported (13, 14). This LC/MS method was linear over 0.05 - 10 μg/mL concentration range with a lower limit of quantitation (LLOQ) of 0.05 μg/mL. Interday precision and accuracy for the method were within the acceptance criteria of < 15%.

3.2.6 Surgical Procedures

Male Sprague-Dawley rats (~ 250 g) were obtained from Simonsen Labs (Gilroy, CA, USA) and given food (Purina Rat Chow 5001) and water *ad libitum* in our animal facility for at least 3 days before use. Rats were housed in temperature-controlled rooms with a 12 h light/dark cycle. The day before the pharmacokinetic experiment, the right jugular veins of the rats were catheterized with sterile silastic cannula (Dow Corning, Midland, MI, USA) under isoflurane anesthesia. After cannulation, the Intramedic PE-50 polyethylene tubing (Becton, Dickinson and Company, Franklin Lakes, NJ, USA) connected to the cannula was exteriorized through the dorsal skin. The cannula was flushed with 0.9 % saline. The animals were transferred to metabolic cages and fasted overnight. Animal use protocols were approved by The Institutional Animal Care and Use Committee at Washington State University.

3.2.7 Pharmacokinetic study

On the days of the experiment, animals were intravenously administered a single bolus injection of either ridaforolimus in ethanol/PEG 400 (10 mg/kg, n = 7) or the ridaforolimus in DSPE-PEG_{2000} (10 mg/kg, n = 7). These dosages were based on dose varying studies previously conducted in our laboratory with the structurally similar compound, rapamycin, and is in accordance with animal studies of ridaforolimus (5, 6).

After dosing, serial blood samples (~0.30 mL) were collected from the cannula at 0, 1 min, and 30 min, then 1, 2, 4, 6, 12, 24, and 48 h after intravenous

administration, and the cannula flushed with 0.9 % saline. After dosing and after each serial blood sampling, blinded observers were present to record any visible behavior, bleeding, or change in overall appearance of the animal as signs of acute tolerability. Each blood sample was collected and following centrifugation, the serum was collected and stored at –70 °C until analyzed.

3.2.8 Sample preparation

To extract ridaforolimus from serum samples, an ethyl acetate extraction was used. To 100 µL of serum sample, 10 µL of IS (100 µg/mL), 200 µL HPLC-grade water, and 1 mL of ethyl acetate were added. Samples were vortexed for 30 s, centrifuged at 5000 rpm for 5 min, and the organic phase transferred to a new sample tube and dried under a stream of nitrogen gas. Dried samples were reconstituted with 100 µL of mobile phase and 10 µL injected into the LC/MS system.

3.2.9 Pharmacokinetic analysis

Pharmacokinetic analysis was completed using data from individual rats for which the mean and standard error of the mean (SEM) were calculated for each group except for T_{max} which was represented as median and range. Pharmacokinetic parameters were estimated through noncompartmental analysis by the methods of Gibaldi *et al.* (15). The apparent terminal elimination rate constant (k_e) was estimated from the slope of the log–linear phase of declining serum concentration vs. time plot. The half-life ($t_{1/2}$) was calculated using the following equation: $t_{1/2} = 0.693/k_e$. The area under the concentration time curve

($AUC_{0\text{-}Clast}$) was calculated using the linear/logarithmic trapezoidal method. Summation of $AUC_{0–Clast}$ and the concentration at the last measured point divided by k_e yielded $AUC_{0–\infty}$. Mean residence time (MRT) was calculated by dividing $AUMC_{0\text{-}\infty}$ by $AUC_{0\text{-}\infty}$, clearance (Cl) by dividing dose by $AUC_{0\text{-}\infty}$, and volume of distribution (V_{ss}) by multiplying MRT by Cl.

3.2.10 Statistical analysis

Quantification was based on calibration curves constructed using peak area ratio (PAR) of ridaforolimus to internal standard, against ridaforolimus concentrations using unweighted least squares linear regression. Pharmacokinetic analysis was performed using data from individual rats for which the mean and standard error of the mean (SEM) were calculated for each group. The data were analyzed for statistical significance in Microsoft Excel® using student's t-test with a value of $p < 0.05$ being considered statistically significant.

3.3 Results and Discussion

3.3.1 Formulation of ridaforolimus in DSPE-PEG_{2000} micelles

The formation of drug loaded DSPE-PEG2000 was confirmed by GPC study (Fig. 2A). Loading of ridaforolimus into DSPE-PEG_{2000} micelles greatly improved the aqueous solubility of ridaforolimus by approximately 40 times from 200 µg/mL to 8.9 mg/mL (6). The diameters of the drug-loaded micelles as determined by DLS were 33 ± 15 nm (Fig. 2B). This size range has been shown appropriate for

extended circulation time *in vivo* and accumulation within the tumor through the EPR effect (9).

3.3.2 Micelle characterization

Micelles appeared as a distinct peak on SEC, with a retention time of 6.966 min for the DSPE-PEG_{2000} micelles (873,000 Da using PEG standards) (Fig. 2A). The micelle fractions were collected and assayed for drug content by HPLC with UV detection. Ridaforolimus was found in the micelle GPC peak, and the HPLC retention time was identical to the standard with no additional peaks. The drug loading efficiency (DL %) for 10 % (w/w) drug loaded micelles was 7.194 ± 0.143 % and the encapsulation efficiency (EE %) was 77.519 ± 1.658%.

The *in vitro* release profiles of free drug and micelle formulation of ridaforolimus were investigated at simulated *in vivo* conditions using a PBS bath at pH 7.4 and 37 °C (Fig. 3). The *in vitro* $t_{50\%}$ was improved from less than 20 min to 1.5 d and $t_{90\%}$ was increased from 1 h to 6.5 d (Fig. 3).

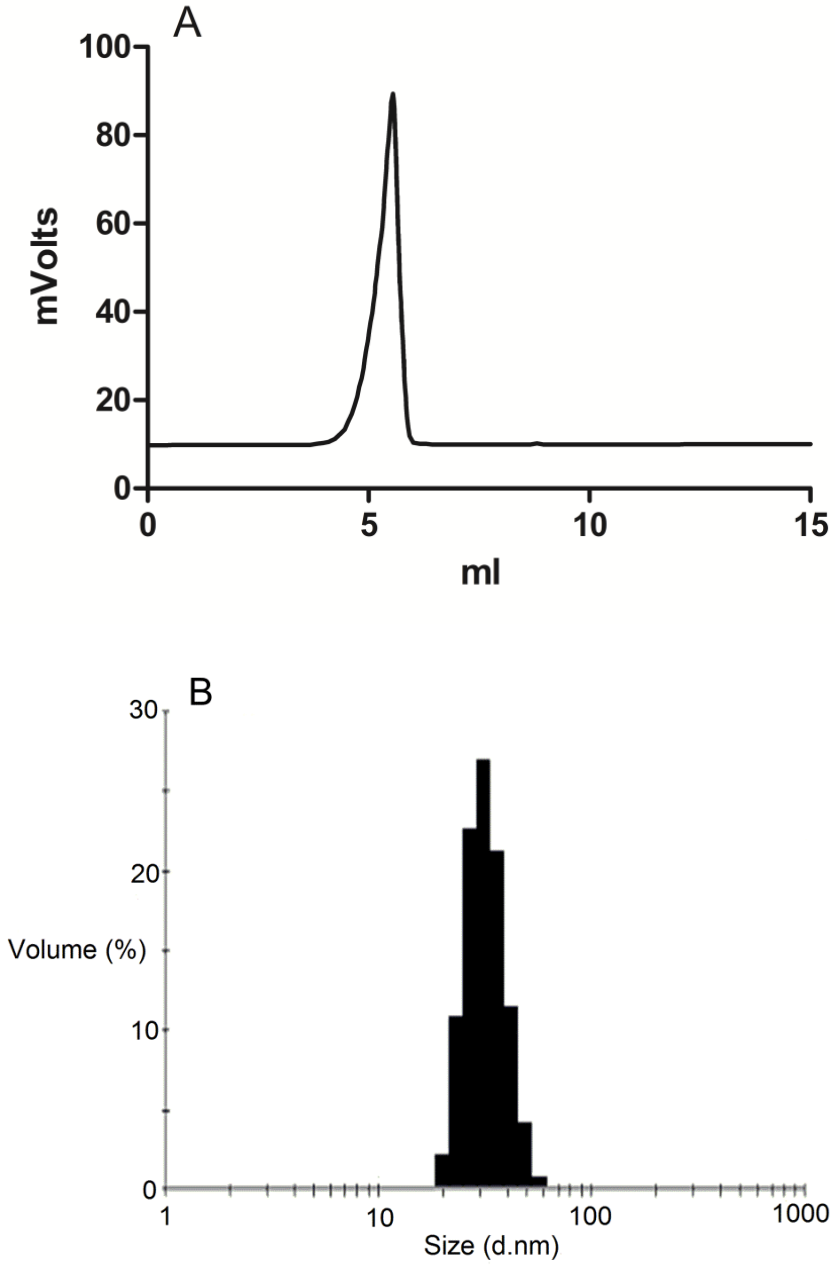

Fig. 2: (A) GPC chromatography of ridaforolimus loaded DSPE-PEG_{2000} micelles in water mobile phase at 0.8 mL/min with ELSD detection. (B) Size distribution of ridaforolimus loaded DSPE-PEG_{2000} micelles indicating an average diameter of 33 nm.

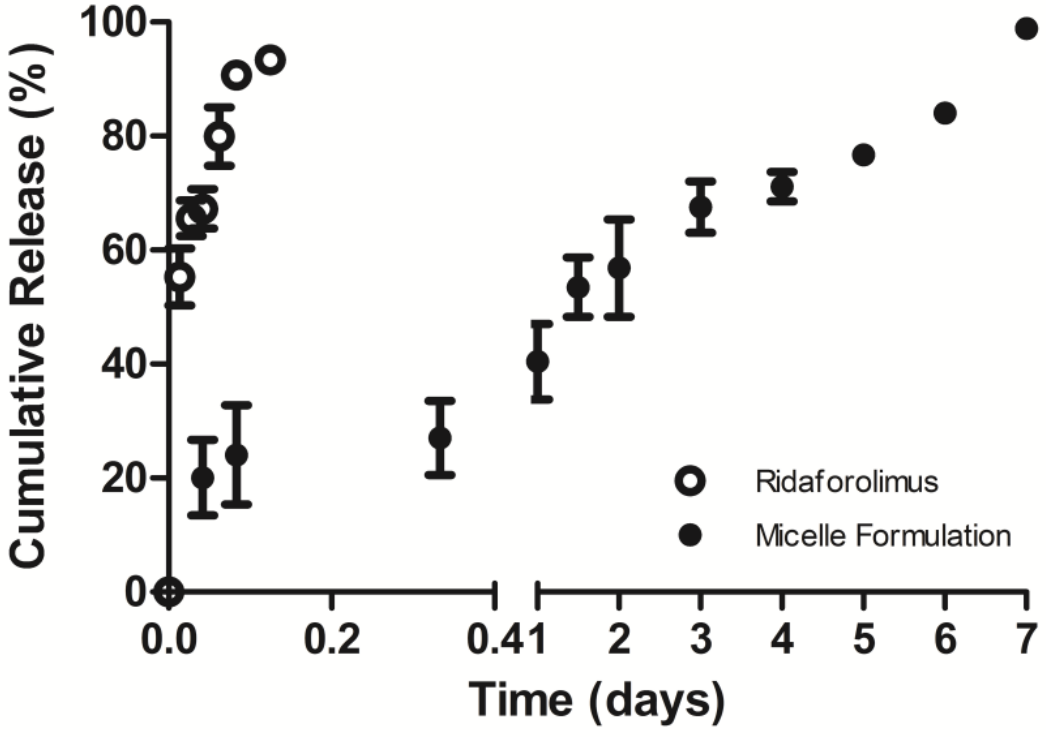

Fig. 3: Release profile of ridaforolimus in PEG-DSPE$_{2000}$ micelles (●) compared to free drug in PBS (○) (mean ± SD) (n=3).

3.3.3 Micelle formulation effects on cellular uptake of the drug

The DU145 and MDA-1986 cells were treated with naked ridaforolimus and ridaforolimus loaded DSPE-PEG_{2000} micelles. After a 6-h treatment, the drug uptaken by the cells was quantified by HPLC (Fig. 4). Micelle formulation significantly improved the cellular uptake at all concentrations in both DU145 and MDA-1986 cells. In addition, DMSO was not required to solubilize ridaforolimus in the micelle formulation.

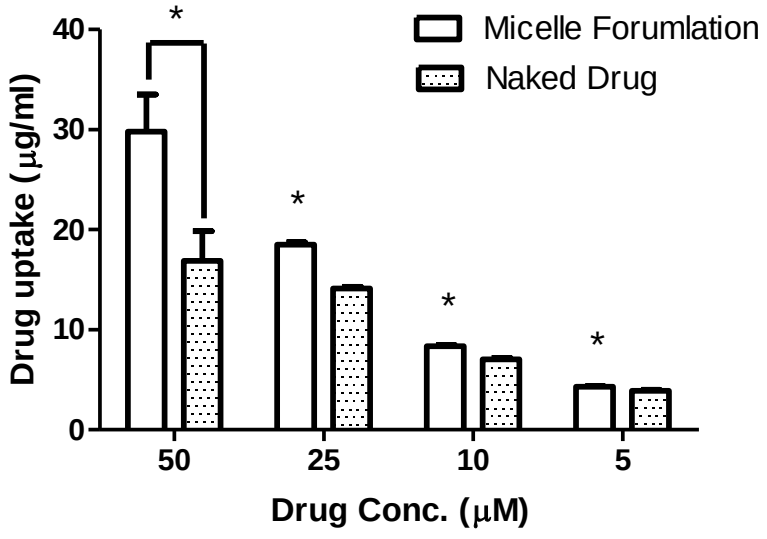

A

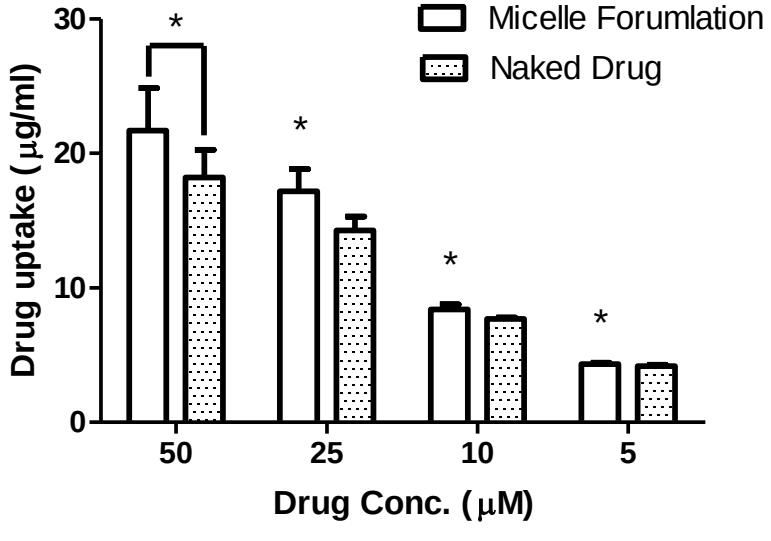

B

Fig. 4: The micelle formulation improved ridaforolimus uptake by DU145 cells (A) and MDA-1986 cells (B) (mean ± SD). (*: $p < 0.01$ between formulations the same concentration)

3.3.4 Pharmacokinetic evaluation of a DSPE-PEG_{2000} formulation of Ridaforolimus

Tolerability and the pharmacokinetic disposition of two ridaforolimus formulations were assessed. No observable differences were seen in the tolerability of the ethanol/PEG_{400} formulation and DSPE-PEG_{2000} micelle formulation among blinded observers. No tolerability differences were expected as the appearance of the toxicities associated with mTOR inhibitors are most often delayed (e.g. mucositis).

Pharmacokinetic differences between the micellar and ethanol/PEG 400 formulations of ridaforolimus following intravenous administration are illustrated in Fig. 5. Ridaforolimus in the control formulation of ethanol/PEG400 exhibited a rapid distribution and elimination from the body where concentrations fell below detectable limits after 4 h post-dose. Solubilization of ridaforolimus in DSPE-PEG_{2000} micelles provided a slightly more sustained release and quantifiable presence of ridaforolimus in serum up to 12 h. Non-compartmental analysis of the pharmacokinetic parameters of these formulations are reported in Table 1. The micelle nanocarrier formulation increased elimination half-life ($t_{1/2}$) by 1.7-fold and decreased the clearance by 0.6 fold. This may indicate that the micelle formulation increases the serum circulation time of ridaforolimus *in vivo*. The micelle formulation also increased the AUC by 3.7-fold and decreased the V_{ss} by 1.8-fold, but these were not statistically significant ($p < 0.05$).

Table 1: Pharmacokinetics of ridaforolimus after IV administration of control ridaforolimus in ethanol/PEG_{400} and ridaforolimus in DSPE-PEG_{2000} micelles. The intravenous dose for all the formulations was 10 mg/kg to rats (mean ± SEM, n = 7 per group). *Significantly different from formulation in ethanol/PEG 400 ($p < 0.05$).

PK Parameters	Ridaforolimus in ethanol/PEG_{400} (mean ± SEM)	Ridaforolimus in DSPE-PEG_{2000} micelles (mean ± SEM)
$AUC_{0\rightarrow\infty}$ (h×µg/ml)	1.40 ± 0.23	5.16 ± 2.13
V_{ss} (l/kg)	10.82 ± 2.10	6.05 ± 2.10
Cl_{total} (l/h/kg)	8.31 ± 1.58	3.45 ± 0.79*
$t_{1/2}$ (h)	1.20 ± 0.11	3.18 ± 0.64*
MRT (h)	1.34 ± 0.15	1.57 ± 0.51

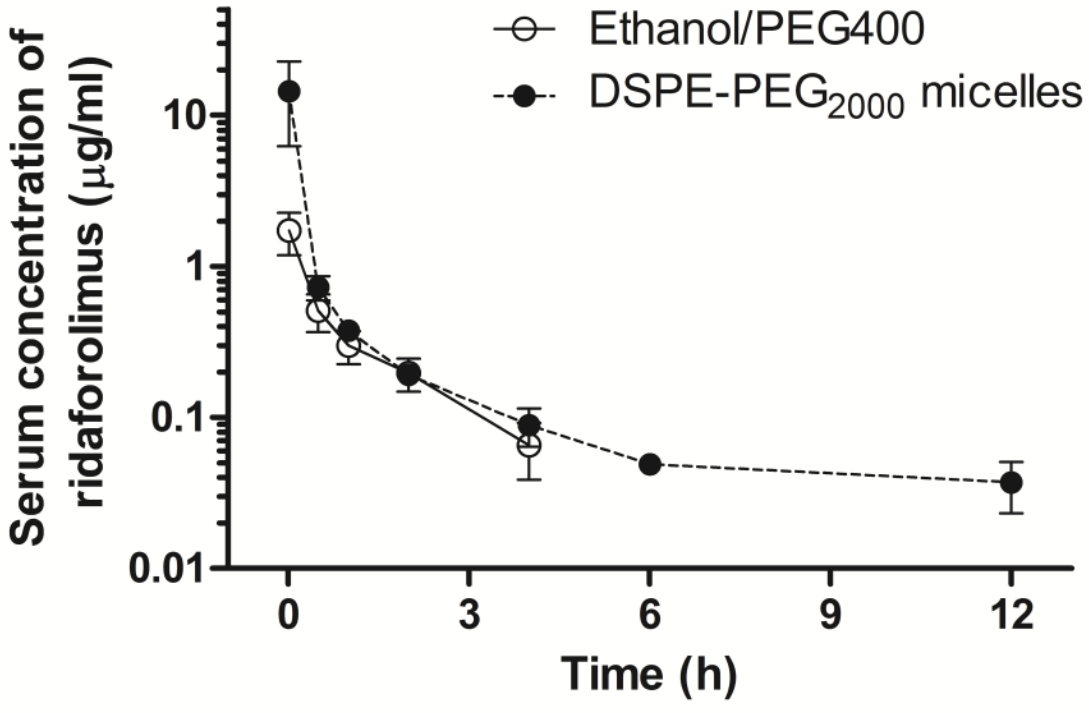

Fig. 5: Concentration-time profile in serum of ridaforolimus after intravenous administration of control ridaforolimus formulation in ethanol/PEG_{400} and ridaforolimus in DSPE-PEG_{2000} micelles. The dose for all the formulations was 10 mg/kg to rats (mean ± SEM, n = 7 per group).

Previous attempts to solubilize highly lipophilic compounds with polymeric micelles have showed dramatic alteration in the pharmacokinetics and biodistribution of these compounds. For instance, encapsulation of paclitaxel prodrugs into PEG-b-PCL micelles increased the $AUC_{0-\infty}$ of the prodrug 54-fold in comparison to control while improving tolerability and altering paclitaxel's biodistribution (11). For unclear reasons, solubilization of ridaforolimus in DSPE-PEG_{2000} micelles did not dramatically increase the residence time or the overall systemic exposure of ridaforolimus. This may be indicative of a lack of *in vivo* stability or an inability to evade the mononuclear phagocyte system. DSPE-PEG is well established to have detergent-like properties that may disrupt the balance of hydrophobicity and hydrophilicity of the nanocarrier. This is most well known in liposomes where DSPE-PEG is a common PEGylate choice yet can also be responsible for disrupting the lipid membrane (10).

No other reports of solubilization of ridaforolimus in micelles or other forms of nanocarriers are available in the biomedical literature. However, there are reports of the encapsulation of rapamycin, the parent drug of ridaforolimus, using PEG-b-PCL and DSPE-PEG_{2000} micelles (5, 11, 12). The pharmacokinetics of rapamycin in these micelles has only been evaluated with the PEG-b-PCL formulation. The PEG-b-PCL greatly improved the tolerability of rapamycin with decreased distribution of rapamycin into brain tissue (5). The formulation, however, had no significant effect of the pharmacokinetic disposition of rapamycin with only a longer $t_{1/2}$ being

significant (5). These results appear to be in accordance with the results found in this study.

To our knowledge, this is the first report of the pharmacokinetics of ridaforolimus in rats. The results reported herein vary greatly from those reported in clinical Phase I trials of ridaforolimus in humans suggesting species dependent pharmacokinetics. Within these human trials, a much long half-life of 45-52 h is reported (3). Possible differences may stem from limits reached analytically as the LC/MS method reported here could detect ridaforolimus only to 50 ng/mL while LC/MS/MS used in clinical studies allowed detection to 0.5 ng/mL (3). This may have prevented accurate estimation of the terminal phase of elimination. Additionally, data reported within were collected from rat serum rather than whole blood. The concentrations of ridaforolimus in the serum component may have simply been too low for proper analytical quantitation.

It was hypothesized at the beginning of this study that encapsulation within DSPE-PEG_{2000} micelles would greatly alter the pharmacokinetic parameters of ridaforolimus. A decrease in volume of distribution was anticipated due to an expected decrease in partitioning of ridaforolimus to the red blood cell compartment. Limiting red blood cell partitioning could have theoretically limited saturation of the substantial amount of FKBP-12 binding protein within erythrocytes. This saturation has been suggested as a possible reason for the lack of dose proportionality with ridaforolimus and other rapamycin analogs. Taken together, it can be speculated that it may have been possible

to improve the dose proportionality of ridaforolimus by solubilizing in a nanocarrier system. However, no significant changes in volume of distribution were seen, but there were trends for a decrease in volume.

These are the first of results in the literature describing the pharmacokinetics of ridaforolimus in rats as well as the first results presenting its formulation via nanocarriers. Other work in our laboratory continues to explore solubilizing lipophilic drugs in nanocarriers and the effects these formulations have on disposition of these drugs.

3.4 Conclusions

The DSPE-PEG_{2000} micellar formulation dramatically improved the solubility of ridaforolimus and provided optimum sizing of the micelle particles. Upon intravenous administration of ridaforolimus loaded DSPE-PEG_{2000} micelles to rats, alterations in the pharmacokinetics of ridaforolimus could be detected. This included a significant increase in half life and decrease in clearance, and non-significant changes in AUC and volume of distribution. These results suggest that the micelle formulation may increase the retention of drug, but the micelle formulation may have limited stability *in vivo*. Since the micelle formulation significantly enhances the drug's aqueous solubility and eliminates harmful excipients, the toxicity profile may be improved. The toxicity and efficacy in xenografts will be reported in a future study.

3.5 References

1. R. Yuan, A. Kay, W.J. Berg, and D. Lebwohl. Targeting tumorigenesis: development and use of mTOR inhibitors in cancer therapy. Journal of hematology & oncology. 2:45 (2009).
2. M. Mita, K. Sankhala, I. Abdel-Karim, A. Mita, and F. Giles. Deforolimus (AP23573) a novel mTOR inhibitor in clinical development. Expert opinion on investigational drugs. 17:1947-1954 (2008).
3. C.M. Hartford, A.A. Desai, L. Janisch, T. Karrison, V.M. Rivera, L. Berk, J.W. Loewy, H. Kindler, W.M. Stadler, H.L. Knowles, C. Bedrosian, and M.J. Ratain. A phase I trial to determine the safety, tolerability, and maximum tolerated dose of deforolimus in patients with advanced malignancies. Clinical cancer research : an official journal of the American Association for Cancer Research. 15:1428-1434 (2009).
4. J.E. Dancey. Therapeutic targets: MTOR and related pathways. Cancer biology & therapy. 5:1065-1073 (2006).
5. J.A. Yanez, M.L. Forrest, Y. Ohgami, G.S. Kwon, and N.M. Davies. Pharmacometrics and delivery of novel nanoformulated PEG-b-poly(epsilon-caprolactone) micelles of rapamycin. Cancer chemotherapy and pharmacology. 61:133-144 (2008).
6. V.M. Rivera, R.M. Squillace, D. Miller, L. Berk, S.D. Wardwell, Y. Ning, R. Pollock, N.I. Narasimhan, J.D. Iuliucci, F. Wang, and T. Clackson. Ridaforolimus (AP23573; MK-8669), a potent mTOR inhibitor, has broad antitumor activity and can be optimally administered using intermittent dosing regimens. Molecular cancer therapeutics. 10:1059-1071 (2011).

7. S.R. Croyand G.S. Kwon. Polymeric micelles for drug delivery. Current pharmaceutical design. 12:4669-4684 (2006).
8. M.P. Xiong, J.A. Yanez, C.M. Remsberg, Y. Ohgami, G.S. Kwon, N.M. Davies, and M.L. Forrest. Formulation of a geldanamycin prodrug in mPEG-b-PCL micelles greatly enhances tolerability and pharmacokinetics in rats. Journal of controlled release : official journal of the Controlled Release Society. 129:33-40 (2008).
9. M.L. Adams, A. Lavasanifar, and G.S. Kwon. Amphiphilic block copolymers for drug delivery. Journal of pharmaceutical sciences. 92:1343-1355 (2003).
10. S.D. Liand L. Huang. Pharmacokinetics and biodistribution of nanoparticles. Molecular pharmaceutics. 5:496-504 (2008).
11. R. Vakil, K. Knilans, D. Andes, and G.S. Kwon. Combination antifungal therapy involving amphotericin B, rapamycin and 5-fluorocytosine using PEG-phospholipid micelles. Pharmaceutical research. 25:2056-2064 (2008).
12. M.L. Forrest, C.Y. Won, A.W. Malick, and G.S. Kwon. In vitro release of the mTOR inhibitor rapamycin from poly(ethylene glycol)-b-poly(epsilon-caprolactone) micelles. Journal of controlled release : official journal of the Controlled Release Society. 110:370-377 (2006).
13. M.J. Bogusz, E.A. Enazi, H. Hassan, J. Abdel-Jawaad, J.A. Ruwaily, and M.A. Tufail. Simultaneous LC-MS-MS determination of cyclosporine A, tacrolimus, and sirolimus in whole blood as well as mycophenolic acid in plasma using common pretreatment procedure. Journal of chromatography B, Analytical technologies in the biomedical and life sciences. 850:471-480 (2007).

14. M.A. Poquette, G.L. Lensmeyer, and T.C. Doran. Effective use of liquid chromatography-mass spectrometry (LC/MS) in the routine clinical laboratory for monitoring sirolimus, tacrolimus, and cyclosporine. Therapeutic drug monitoring. 27:144-150 (2005).

15. M. Gibaldi, Perrier, D. Pharmacokinetics, Informa Healthcare USA, Inc.

Chapter 4

Pharmaceutical Characterization, Disposition and Efficacy of Hyaluronic acid-Rapamycin Conjugates

4.1 Introduction

CD44 is a cell surface molecule involved in proliferation, differentiation and migration, etc (1). The CD44 receptor is one of the most widely accepted cell surface markers of variety types of cancer cells, such as breast cancer cell lines MCF-7, MDA-MB-468 and MDA-MB-231 (2); prostate cancer cell lines PC-3 and TSU-Pr1 (3); and head and neck cancer Gun-1. The expression of specific CD44 isoforms is also associated with various cancer biomarkers and tumor subtypes (4). The ligands of CD44 include hyaluronic acid (HA), osteopontin, collagens and matrix metalloproteinases. CD44 receptor mediates cell-cell and cell-matrix interactions through its affinity with HA and the adhesion with HA molecule plays an important role in tumor growth and progression. Therefore, the interaction of CD44 and HA was reported as a potential target for cancer therapy (5, 6).

The usage of HA as a polymer for drug delivery could provide specific cancer targeting and the benefits associated with polymer-drug conjugates. The polymer-drug conjugates are designed to increase therapeutic index by drug specific targeting of disease, tissues, reducing systemic drug exposure (7, 8), and increased plasma circulation time. Polymer-drug conjugate based anticancer agents have entered routine clinical use, such as Cimzia® (certolizumab-polyethylene $glycol_{40k}$), Xyotax® (paclitaxel-poly-L-glutamic acid) and Macugen® (polyethylene glycol-conjugated RNA aptamer) (9-11). The polymer-drug conjugates can be bio-activated to provide their own therapeutic benefits, and they also can improve release kinetics of the drug and prevent carrier accumulation in the body (12). Moreover, the polymer based drug delivery platform has demonstrated prolonged *in vivo* half-life, is less prone to enzyme degradation with less immunogenicity compared to the

conventional chemotherapy (13-15). It also provides an effective and promising way for neoplastic treatment due to the changing of cellular uptake mechanisms, pharmacokinetic disposition and ultimately targeting of the drug (16).

Rapamycin is a selective inhibitor of mammalian target of rapamycin (mTOR) and blocks the subsequent activation of p70 S6 kinase (17). The mTOR pathway regulates a variety of cellular signals and development processes, including mitogenic growth factors, hormones, nutrients, cellular energy levels and stress conditions (18). It is frequently activated in certain human cancers, such as breast cancer (19) and gastric cancer (20). The mTOR pathway is also widely involved in both apoptotic and autophagic pathways during oxidative stress (21, 22). Therefore, inhibiting the mTOR pathway is extensively considered as an effective approach for targeted cancer therapy (23). A 2-year clinical trial of rapamycin on renal angiomyolipoma in tuberous sclerosis showed that mTOR inhibitors are relatively safe, efficacious and less aggressive (24). However, systemic toxicity was observed after administration of rapamycin, inducing fevers, anemia and capillary leak syndrome (25). To lower the systemic toxicities, localized delivery of rapamycin using biodegradable bead (35:65 ratio of caprolactone and glycolide) for the treatment of malignant glioma was reported. In an animal study it was demonstrated that a significantly longer survival with targeted rapamycin therapy was possible compared to the free drug and the placebo groups (26).

In this study, HA-rapamycin conjugates prepared with different linkers were synthesized. Sustained and controlled release of the drug was achieved. Both chemical and physical properties of the polymer-drug conjugate were fully characterized. *In vitro* studies were performed to examine CD44-mediated cancer

cell uptake. Efficacy of the drug conjugate was evaluated in BALB/c mice and pharmacokinetics studies were completed in Sprague-Dawley rats.

4.2 Materials and Methods

4.2.1 Materials

Hyaluronic acid (35 kDa) and rapamycin were purchased from Lifecore Biomedical, Inc. (Chaska, MN) and LC Laboratories (Woburn, MA), respectively. Fmoc-3-amino-4-methoxy-benzoic acid was purchased from AnaSpec, Inc. (Fremont, CA). Other materials and solvents, of their highest grade, were purchased from Fisher Scientific (Lenexa, KS) or Sigma Aldrich (St. Louis, MO), and they were used as received unless stated otherwise. NMR spectra were collected with a 400-MHa Bruker and the mass spectra were obtained by electrospray ionization mass spectrometry (ESI-MS).

4.2.2 Synthesis of rapamycin 42-hemisuccinate

The synthetic scheme is shown in Fig. 1A. A mixture of rapamycin (0.20 g, 0.22 mmol), succinic anhydride (0.10 g, 1.0 mmol) and Novozym SP 435 (0.45 g) in toluene (10 mL) was stirred at 45 ^{o}C under argon for 40 h. The enzyme was filtered off and washed with toluene, and the combined organic phases were concentrated under reduced pressure. The residue was purified by silica gel column chromatography and eluted with EtOAc-hexane (1:4) to furnish the title compound as a white solid (0.2 g, 90%) (27).

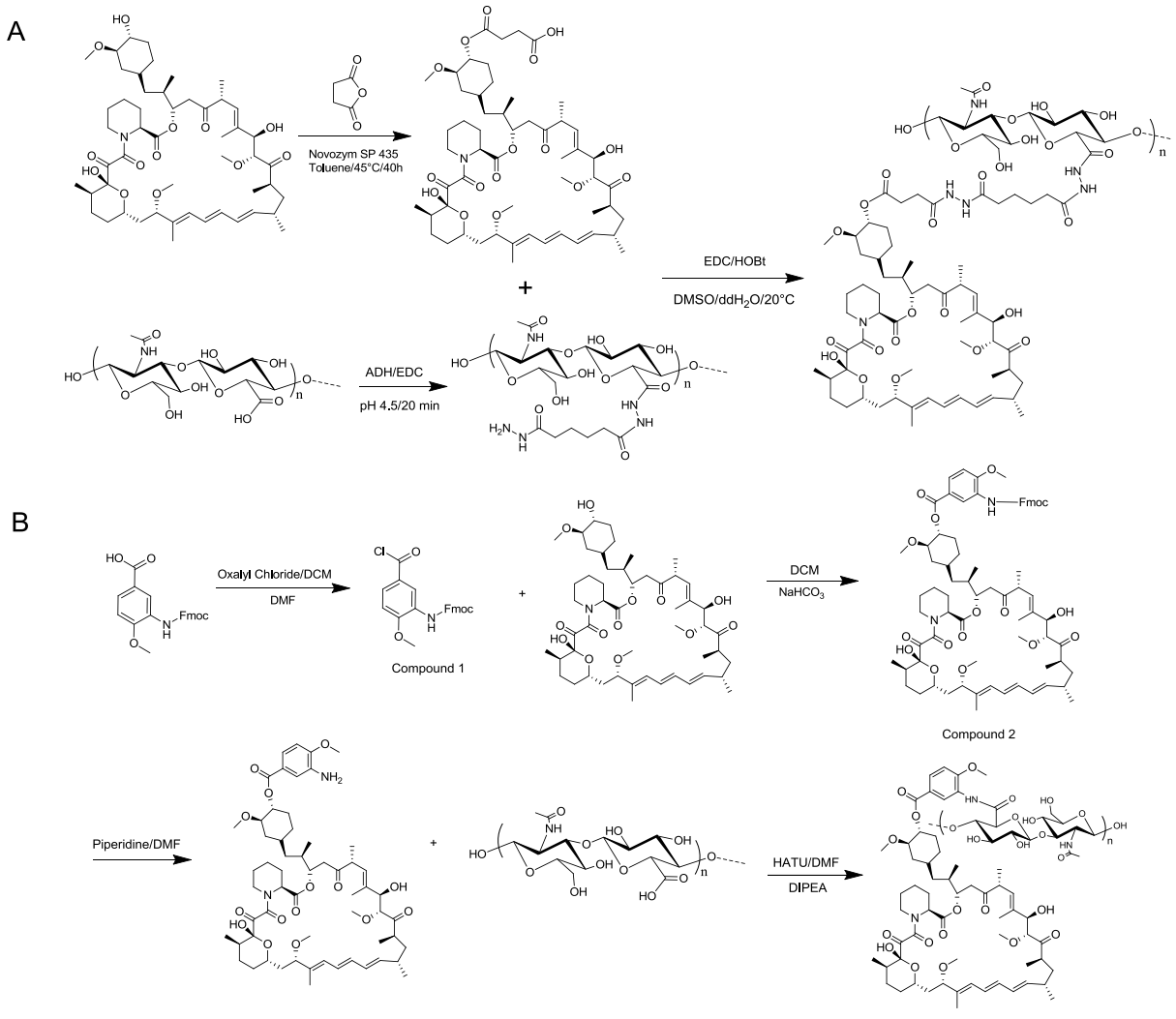

Fig. 1: Synthesis of Hyaluronic Acid (HA)-Temsirolimus (A) and Hyaluronic Acid-Rapamycin-42-(3'-amino-4'-methoxy)benzoate (HA-L-Rapa) (B).

4.2.3 Synthesis of Hyaluronic Acid (HA)-Temsirolimus

The 42-hemisuccinated rapamycin (0.150 g, 0.15 mmol) was dissolved in 4 mL of dimethyl sulfoxide (DMSO), and 1-ethyl-3-(3-dimethylaminopropyl) carbodiimide hydrochloride (EDC·HCl) (0.057 g, 0.30 mmol) and 1-hydrocybenzotriazole hydrate (HOBt·H_2O) (0.046 g, 0.30 mmol) were added to the solution. After 20 min, this solution was added drop wise to HA-adipic acid dihydrazide (ADH) (0.120 g, 22 % ADH) in 10 mL of double distilled water (ddH_2O) cooled on ice. HA-ADH was synthesized as previously described (27). After the addition, the mixture was stirred at ambient temperature (ca. 20°C) overnight. Then, the solution was poured into 100 mL of 95 % ethanol (EtOH), and the white precipitate was collected by centrifugation. This procedure was repeated another two times. The collected solid was dried under vacuum overnight and 0.085 g of the product was obtained (yield: 31.48 %). The loading degree of rapamycin on the conjugate was verified by ^{1}H-NMR.

4.2.4 Synthesis of Hyaluronic Acid-Rapamycin-42-(3'-amino-4'-methoxy)benzoate (HA-L-Rapamycin)

The synthetic scheme of HA-L-rapamycin is shown in Fig. 1B.

Five milliliters of oxalyl chloride in dry methylene chloride (2.0 M in DCM) was added to 150 mg of Fmoc-3-amino-4-methoxy-benzoic acid along with one drop of dry dimethylformamide (DMF) as a catalyst. The mixture was stirred at ambient temperature (ca. 22 °C) under dry argon for 2 h. The white suspension turned into a light yellow, clear solution as the reaction neared completion. The organic solvent was removed under reduced pressure.

Compound 1 was suspended in 5 mL of dry DCM and 100 mg of rapamycin and 200 mg of $NaHCO_3$ were added to the solution. The mixture was stirred at ambient temperature for 2 h under dry argon and protected from light. The suspension was filtered, and the filtrate was washed with bicarbonate water and brine. The organic solvent was dried with Na_2SO_4 and then removed under reduced pressure.

Compound 2 was suspended in 20 % (v/v) piperidine in DMF. The solution was stirred at ambient temperature for 1 h. The organic solvent was removed under reduced pressure and the pale yellow solid was washed several times with ddH_2O.

O-(7-azabenzotriazol-1-yl)-*N*,*N*,*N*′,*N*′-tetramethyluronium hexafluorophosphate (HATU) (100 mg, 0.26 mmol) in 1 mL of DMF and N,N-Diisopropylethylamine (DIPEA) (47 µL, 0.27 mmol) were added to 100 mg HA in 5 mL of ddH_2O. After 30 min, rapamycin-42-(3'-amino-4'-methoxy) benzoate in 5 mL of DMF was added. The mixture was stirred at ambient temperature overnight. Then, the organic solvent was removed by dialysis (10k MWCO snake skin pleated dialysis tubing, Thermo Scientific, Rockford, IL) against ddH_2O. The unbound drug produced a light yellow precipitate that was removed by centrifugation. The drug conjugate was further purified by tangential flow filtration (TFF) using a MicroKros mPEG filter (3.5k MWCO, Spectrum Labs, Rancho Dominguez, CA). Briefly, the mPES MicroKrosMix® Hollow Fiber Filter module was flushed by ddH_2O under a pressure of 10 psi provided by a Manostat Varistaltic dispenser and pump. After the filter membrane was fully hydrated and washed with ddH_2O, the filter module was fed with the HA-L-Rapa solution maintaining a pressure of less than 10 psi,

and the drug conjugate solution was concentrated by maintaining the pump pressure at less than 20 psi. The rapamycin loading degree on HA was determined by ^{1}H-NMR.

4.2.5 *In Vitro* Drug Release Study

The *in vitro* release of the rapamycin from HA-drug conjugates into PBS or PBS supplemented with 10 % fetal bovine serum (FBS) at 37 ^{0}C was monitored by a dialysis method using a SnakeSkin® pleated dialysis tubing (3,500 MWCO) (28). To prevent bacteria growth, 0.05 % sodium azide was added to the serum release medium, and the medium was changed several times a day to maintain sink conditions. After the predetermined time intervals, samples were withdrawn from the dialysis tubing and analyzed using a Spectra MaxM2 microplate spectrophotometer with UV detection of rapamycin at 260 nm.

4.2.6 HA-Rapamycin Conjugate Characterization

4.2.6.1 Particle Size

HA and HA-L-Rapa with different loading degrees were dissolved in PBS at the concentration of 2.5 mg/mL. The particle sizes were measured with a ZetaPALS (Brookhaven Instruments Corp.) using the intensity weighted Gaussian distribution.

4.2.6.2 Zeta Potential

HA and HA-L-Rapa with different loading degree were dissolved in 10 mM KCl at the concentration of 2.5 mg/mL. Zeta potentials were measured using ZetaPALS. Zeta potential was calculated from the mobility of the system fitted into the Smoluchowski model (29).

4.2.6.3 Turbidity

One hundred microliter samples at the concentration of 2.5 mg/mL were placed in a 96-well flat-bottomed plate (Greiner Bio-One UV Star). The turbidities in the wells were measured as absorbance at 350 nm using a Spectra MaxM2 microplate spectrophotometer and determined in triplicate.

4.2.7 Thermal Analysis

4.2.7.1 Differential scanning calorimetry (DSC)

HA-L-Rapa with different loading degrees and HA_{35k} polymer, as received, were studied using a Q100 Universal V4.3A DSC (TA Instruments, New Castle, Delaware). The samples were sealed in a standard aluminum pan and heated from 40 to 300 ^{0}C at a scan rate of 10 ^{0}C/min.

4.2.7.2 Thermo gravimetric analysis (TGA)

TGA was performed on a Q50 thermogravimetric analyzer from TA Instruments. Samples were loaded on a platinum sample pan and heated from 25 to 500 ^{0}C with a heating rate of 10 ^{0}C/min. Data were analyzed using Universal Analysis 2000 (version 4.3A) software (TA Instrument).

4.2.8 Flow Cytometry Analysis

The expression of CD44 receptor on the surface of breast cancer cells, MDA-MB-468 and 4T1.2neu, was examined by flow cytometry analysis. PE mouse anti-human CD44 (BD Pharmingen, San Jose, CA) was used to stain MDA-MB-468 cells, and PE rat anti-mouse CD44 (Pgp-1-R-PE, Southern Biothech, Birmingham, AL) was used with murine 4T1.2neu cells. PE mouse IgGI isotope control (BD Pharmingen, San Jose, CA) was used as a control. Anti-human

CD44 antibody (H-CAM, Thermo Scientific, Rockford, IL) was used in receptor blocking assays.

4.2.9 Cytotoxicity Assay

Breast cancer MDA-MB-468 cells were maintained in Dulbecco's modified eagle medium supplemented with 10 % fetal bovine serum (Hyclone Laboratory Inc., Logan, Utah). Cells were plated in white 96-well flat-bottomed plates at the concentration of 5,000 cells/well in 90 µL of growth medium. After 12 h, rapamycin or HA-L-Rapa in Hanks' solution were added at different concentrations. Hanks' solution and 10 % trichloroacetic acid (TCA) were used as negative and positive control, respectively. The medium was refreshed 8 h after treatment. After 72 h post-treatment, resazurin blue (5 µM) was added and the resorufin product was measured with a fluorophotometer using an excitation wavelength of 550 nm and an emission wavelength of 590 nm.

4.2.10 Cellular Uptake Study

Breast cancer cells, MDA-MB-468, were seeded in a 12-well plate at the concentration of 50,000 cells/well in 1 mL of growth medium. After 12 h incubation, 10 µL of human anti-CD44 antibody was added to each well. After 1 h, 10 µM of rapamycin or HA-L-Rapa conjugate were added to the cells. The supernatant was then analyzed by HPLC with a reverse phase column (TSK-GEL® ODS-100Z, Tosoh Bioscience) at 50℃ and UV detection at 278 nm for rapamycin. The chromatography conditions were a mobile phase A of 0.002 % (v/v) TFA in ddH_2O and B of 0.002 % (v/v) TFA in acetonitrile (ACN) at a flow rate of 1 mL/min. The gradient program was i) 5 min with 10 % B; ii) a linear gradient

from 10 % to 90 % B over 5 min; iii) 8 min with 90 % B; and iv) 7 min with 10 % B. The retention time of rapamycin was 16.05 min.

4.2.11 Pharmacokinetics Study

Female Sprague-Dawley rats (350 - 450 g, Charles Rivers) were administered rapamycin (1 mg/mL in formulation buffer) by intraperitoneal (i.p.) injection or HA-L-Rapa (10 mg/kg equivalent rapamycin; n = 3 for each group) by subcutaneous (s.c) injection under isoflurane anesthesia. Whole blood was withdrawn (100 µL) from the tail vein at 0 min, 5 min, 30 min, 1 h, 2 h, 4 h, 6 h, 12 h, 24 h and 48 h after dosing and placed in heparinized tubes (BD Vacutainer® Lithium Heparin 37 USP unit, BD Franklin Lakes, NJ). The whole blood was centrifuged at 15,000 × *g* for 10 min, and the plasma was frozen at -80°C until analyzed. The animal use statement was approved by the University of Kansas Institutional Animal Care and Use Committee.

Plasma samples and standard curves were prepared using a procedure reported previously (30). Briefly, in a microcentrifuge tube, 125 µL of ddH_2O, 125 µL of 0.1 M zinc sulfate and 250 µL of methanol were added to 100 µL of plasma. Then, the tubes were vortexed and centrifuged for 5 min. The colorless supernatant was injected into the LC/MS system. The analyses were performed on an AB Sciex 3200 Q TRAP LC/MS/MS system (Framingham, MA). In the positive-ion mode, the monitored single plot transitions (m/z) was 936 → 937. The separation was carried on Shimadzu SIC-20 UFLC (Shimadzu Scientific Instrument, Overland Park, KS) with an Ascentis® C18 5 cm × 2.1 mm, 3 µm column (Seattle, WA) maintained at 40 °C. The mobile phases were: (A) ddH_2O/Acetonitrile/Formic acid 95/5/0.1 (v/v/v) and (B) ddH_2O/Acetonitrile/Formic

acid 5/95/0.1 (v/v/v). The gradient program was: i) a linear gradient from 50 % to 90 % B over 3 min; ii) 3 min with 90 % B; iii) 4 min with 50 % B. The rapamycin retention time was 3.96 min.

4.2.12 Animal Survival Study and Tissue Distribution

The murine breast cancer 4T1.2neu cell line was used to establish the synergetic orthotropic tumor model in immunocompetent mice. Female BALB/c mice (20 - 25 g, Charles Rivers) under isoflurane anesthesia were inoculated in the right mammary gland with 1×10^6 cells suspended in PBS. Treatment started when the tumor size reached 50 mm^3. Free rapamycin was dissolved in anhydrous ethanol and reconstituted in formulation buffer before use. The formulation buffer of free rapamycin consisted of 5 % polyethylene glycol 400 and 5 % Tween 80 in Hanks' balance salt solution. HA-L-Rapa was dissolved in Hanks' solution. Mice received 10 mg/kg equivalent rapamycin once per week for 3 weeks by i.p. injection (free rapamycin) or s.c injection (HA-L-Rapa). Control animals were injected with Hanks' solution. Animals were sacrificed when tumors grow larger than 1000 mm^3 or if the tumors ulcerated in accordance with the approved animal use protocol.

Drug tissue distribution was determined in female BALB/c mice (n = 5). Tissue samples (50 mg) in 500 µL PBS were homogenized using a Tissue Tearor (BioSpec Products, Inc., Bartlvesville, OK). The homogenized tissue was mixed with 250 µL $ZnSO_4$ and 500 µL methanol. The mixture solution was centrifuged and the supernatant was analyzed by LC/MS.

In the tissue distribution study, BLAB/c mice were administered the drugs 12 h before being euthanized. Major organs (liver, kidneys, hear, spleen, lungs, brain,

muscle), tumor and lymph nodes were excised and lightly washed with PBS. The organs were stored at -80°C until analyzed by LC/MS.

4.2.13 Statistical Analysis

GraphPad Prism 5 software was used for statistical analysis. A *t*-test was used for statistical analysis of comparing two means. The Mantel-Cox test was used for comparison of Kaplan-Meyer analysis. In all comparisons, statistical significance was set at $p \leq 0.05$.

4.3 Results

4.3.1 Polymer Drug Conjugates Synthesis

4.3.1.1 Hyaluronic Acid (HA)-Temsirolimus

Rapamycin 42-hemisuccinate was synthesized according to previous protocols (27). High resolution mass spectrometry (ESI) Calcd for $C_{55}H_{83}NO_{16}Na$ $(M + Na)^+$: 1036.5610; Found: 1036.5623, which was consistent with the reported data.

^{1}H-NMR (D_2O, 400 MHz): δ = 6.79 (m, 1H), 6.18 (m, 1H), 5.95 (m, 1H), 5.50 (m, 1H), 5.21 (m, 1H), 4.47 (broad doublet, 1H on HA), 4.37 (broad doublet, 1H on HA), 4.38-4.45 (broad multiplicity, 8H on HA), 3.43-3.39 (broad doublet, 2H on HA), 3.26 (s, 3H), 3.22 (s, 3H), 2.68 (m, 2H), 2.61 (m, 2H), 1.92 (bs), 1.82 (m, 3H), 1.45 (m, 1H), 1.08 (t, 3H), 0.98 (t, 3H).

4.3.1.2 Rapamycin-42-(Fmoc-3'-amino-4'-methoxy) benzoate

^{1}H-NMR (MeOH-d_4, 400 MHz): δ = 8.47 (s, 1H), 7.80 (d, *J* = 7.6 Hz, 2H), 7.77 (d, *J* = 8.5 Hz, 1H), 7.67 (d, *J* = 6.5 Hz, 2H), 7.40 (t, *J* = 7.3 Hz, 2H), 7.40 (t, *J* = 7.4 Hz, 2H), 7.01 (d, *J* = 8.4 Hz, 1H), 6.86-6.71 (m, 1H), 6.65-6.49 (m, 2H), 6.44-6.10 (m, 5H), 5.78-5.66 (m, 1H), 5.57-5.43 (m, 2H), 5.37-5.15 (m, 3H), 4.45 (d, *J*

= 6.9 Hz, 2H), 4.30 (d, *J* = 6.8 Hz, 1H), 4.27-4.25 (m, 1H), 4.21-4.04 (m, 2H), 3.99-3.93 (m, 2H), 3.92 (s, 3H), 3.66-3.62 (m, 1H), 3.44-3.39 (m, 3H), 3.34 (s, 3H), 3.33 (s, 3H), 3.32 (s, 3H), 2.99-2.89 (m, 2H), 2.84-2.56 (m, 1H), 2.37-2.21 (m, 3H), 2.14-1.98 (m, 3H), 1.96-1.60 (m, 13H), 1.54-1.21 (m, 6H), 1.19-0.63 (m, 25H). HRMS (ESI) Calcd for $C_{74}H_{96}N_2O_{17}Na$ $(M + Na)^+$: 1307.6607; Found: 1037.6650.

4.3.1.3 Hyaluronic Acid-Rapamycin-42-(3'-amino-4'methoxy) benzoate

^{1}H-NMR (D_2O, 400 MHz): δ = 7.65 (d, *J* = 7.6 Hz, 1H), 7.47 (t, *J* = 7.5 Hz, 1H), 7.39 (td, *J* = 7.5, 1.1 Hz, 1H), 6.41-6.35 (m, 1H), 6.20-6.14 (m, 1H), 5.95-5.86 (m, 1H), 5.60-5.40 (m, 2H), 5.15-5.09 (m, 1H), 4.47-4.39 (broad doublet, 2H on HA), 4.39 (broad doublet, *J* = 7.0, 1H on HA), 3.89-3.86 (m, 2H), 3.85-3.80 (m, 4H), 3.78-3.54 (broad multiplicity, 8H on HA), 3.51-3.49 (broad doublet, 2H on HA), 3.42 (broad peak, 2H), 3.26 (s, 3H), 3.22 (s, 3H), 3.13-3.03 (m, 6H), 2.92 (d, *J* = 0.3 Hz, 3H), 2.83-2.80 (m, 4H), 2.79-2.77 (m, 4H), 2.76(m, 6H), 2.68 (m, 2H), 2.61 (m, 2H), 1.92 (broad singlet, 3H), 1.72-1.65 (m, 3H), 1.61-1.55 (m, 3H), 1.50-1.43 (m, 2H), 1.28-0.90 (m, 30H).

Rapamycin loading degree was calculated based on the ratio of 2H on HA (δ = 4.47-4.39) and 1H on rapamycin (δ = 5.15-5.09).

4.3.2 *In Vitro* Drug Release Study

HA-Temsirolimus and HA-L-Rapa were dissolved in ddH_2O at the concentration of 2.5 mg/mL. Free rapamycin was dissolved in ethanol and ddH_2O mixture. The dialysis medium was PBS or PBS supplemented with 10 % FBS. The release profiles were fitted using first (1) or second (2) order kinetics with the following equations:

$A = A_0 e^{-kt}$ (1)

$1/A = 1/A_0 + kt$ (2)

The release half-lives of free rapamycin (PBS), HA-Temsirolimus (PBS), HA-L-Rapa (PBS), HA-L-Rapa (serum) were 0.16 h, 4 h, 7 d and 1.5 d, respectively. The rate constants of release for free rapamycin (PBS), HA-Temsirolimus (PBS), HA-L-Rapa (PBS) and HA-L-Rapa (serum) were shown in Table 1.

Table 1: Calculated release constants of free rapamycin, HA-Rapa and HA-L-Rapa.

	k (day^{-1})	A	error
Free Rapamycin 1st order fit	-27.23	33.48	1700.33
HA-Rapa 1st order fit	-0.1469	22.08	692.99
HA-L-Rapa 1st order fit	-0.07105	26.36	1574.43
HA-L-Rapa 2nd order fit	-0.01767	4.807	19829.83
HA-L-Rapa (serum) 1st order fit	0.9999	2.37×10^{-6}	32815.21
HA-L-Rapa (serum) 2nd order fit	-0.00344	29.56	3520.77

4.3.3 Characterizations of HA Drug Conjugates

4.3.3.1 *Particle sizes and Zeta potentials*

The non-conjugated HA_{35k} and HA-L-Rapa with different drug loading degrees were dissolved in PBS at the concentration of 2.5 mg/mL. Particle sizes were determined by dynamic light scattering (DLS) (Table 2). There was no significant size difference between drug conjugated and non-conjugated HA. However, the absolute value of zeta potential decreased with increasing the drug loading degree on the HA. The negative zeta potential is expected as each HA monomer has one carboxylic group (pKa ~4.5) and one HA_{35k} has approximately 87 repeating units that yield a strong negatively charged nanoparticle at pH 7.4. By conjugating with rapamycin, a large hydrophobic molecule, carboxylic groups on HA surface were partially esterified by conjugation and some adjacent negative charged carboxylic groups were shielded by the drug; therefore, the absolute zeta potential value was decreased.

4.3.3.2 Turbidity

The turbidity test is an objective method to evaluate the solubility of a compound to the solvent. The solubility of HA_{35k} and HA-L-Rapa conjugates were studied in PBS or Hanks' balanced salt solution. At the same concentration, HA-L-Rapa was more turbid in PBS than Hanks' solution, whereas there was no difference for the HA_{35k} control group (Fig. 2).

This indicated that Hanks' solution is a better formulation buffer than PBS. Both PBS and Hanks' solution are isotonic buffered saline solution. However, glucose is supplemented to Hanks' solution. Sugar molecules could bind to the HA or rapamycin through hydrogen-bonding. The hydrophobic surface of the

Table 2: Particle sizes and zeta potentials of HA-L-Rapa with different rapamycin loading degrees (Mean ± SD).

	Size (nm)	**Zeta Potential (mV)**
HA_{35k}	10 ± 0.045	-77.36 ± 14.78
HA-L-Rapa 1.14 % (w/w)	9.8 ± 0.124	-56.15 ± 8.18
HA-L-Rapa 2.21 % (w/w)	9.4 ± 0.012	-44.40 ± 8.11
HA-L-Rapa 4.78 % (w/w)	10.7 ± 0.014	-13.10 ± 3.96

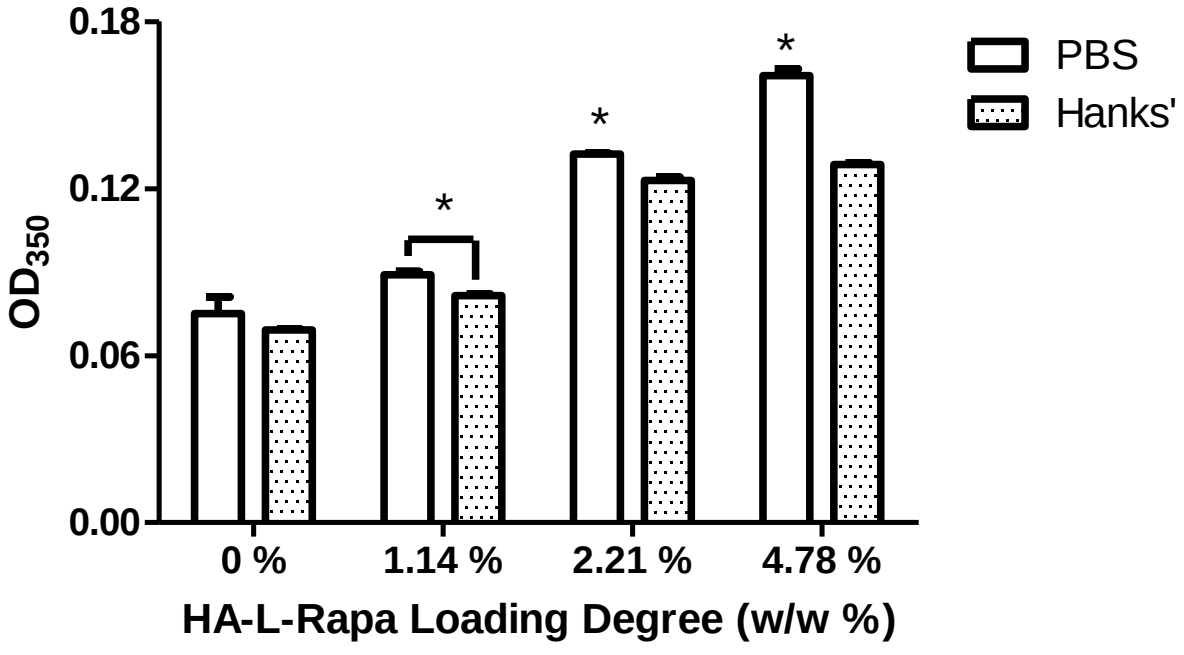

Fig. 2: Turbidity study of HA-L-Rapa with different loading degree in PBS or Hanks' solution (mean ± SD) (n = 3; *, $p < 0.05$).

polymer-drug conjugate might be masked by sugar molecules and the solubility of the polymer-drug conjugates can be improved.

4.3.3.3 DSC

Thermally induced conformational transitions of rapamycin, HA_{35k} and HA-L-Rapa with different drug loading degree are shown in Fig. 3. The rapamycin showed two endothermic peaks at 187 °C and 200 °C. The free HA_{35k} was characterized by a broad endothermic at 120 °C and an exothermic peak at 240 °C. The first broad endothermic peak of HA at approximately 120 °C suggests a dehydration process. An exothermic peak at ca. 240 °C was attributed to the decomposition of the polymer. The free rapamycin was characterized by two endothermic peaks at 187 °C and 200 °C. The split peak indicated that there are two crystalline structures of pure rapamycin. However, the second exothermic characteristic peak of HA_{35k} was not observed in HA-L-Rapa conjugates' DSC profiles. In addition, the two endothermic peaks of free rapamycin merged together and shifted to a higher temperature (210 °C).

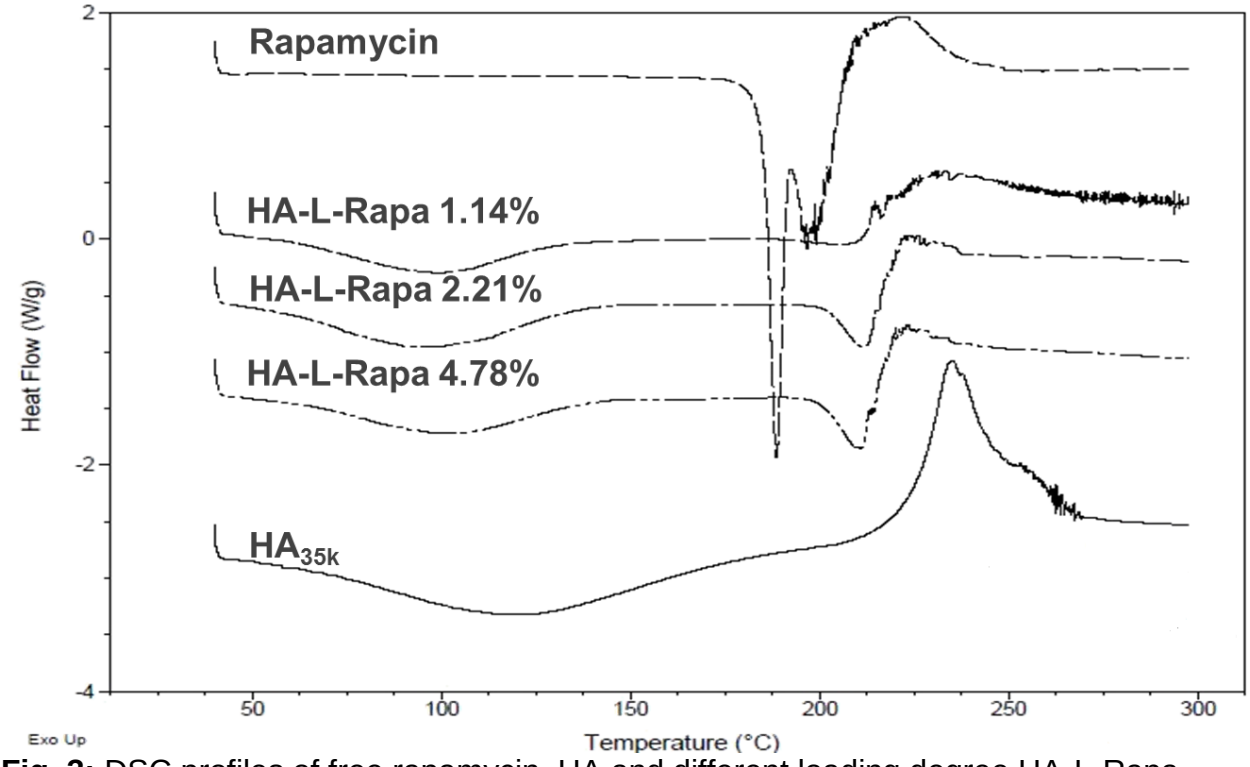

Fig. 3: DSC profiles of free rapamycin, HA and different loading degree HA-L-Rapa.

Both the characteristic decomposition DSC peaks of HA_{35k} and rapamycin disappeared in the HA-L-Rapa profile. The exothermic peak of HA was ascribed to the melting of the polymer crystal. The disappearance of this peak indicated that the original crystalline HA structure was disrupted. In addition, the dehydration peak of HA shifted to a lower temperature (around 100 °C), indicating that the interaction between water and polymer decreased with conjugation of the hydrophobic rapamycin. The endothermic peak of rapamycin shifted to a higher temperature (near 210 °C). The enthalpy (ΔH) was calculated by integrating over the endothermic peak area. For 1.14 %, 2.21 % and 4.78 % (w/w) drug loaded HA, the ΔH was 33.6 ± 0.95, 53.58 ± 0.83 and 65.96 ± 2.81 J/g, respectively. This demonstrated that the degree of thermal stability of HA-L-Rapa is decreased with increased drug loading degree.

4.3.3.4 TGA

Thermogravimetric analysis showed that the drug-polymer conjugates were stable up to 200 °C, when degradation began (Fig. 4).

There were two transition regions during the decomposition process. For the non-drug conjugated HA, the 6.402 % weight lost at approximately 100 °C was consistent with the expected water content of HA. The maximum decomposition, 72.24 % wt, occurred at 235.72 °C which is consistent with polymer decomposition. The temperature of maximum degradation decreased with increasing drug loading: 224.14 °C for the 1.14 % (w/w) conjugate, 218.35 °C for the 2.2 % (w/w) conjugate, and 216.61 for the 4.78 % (w/w) conjugate.

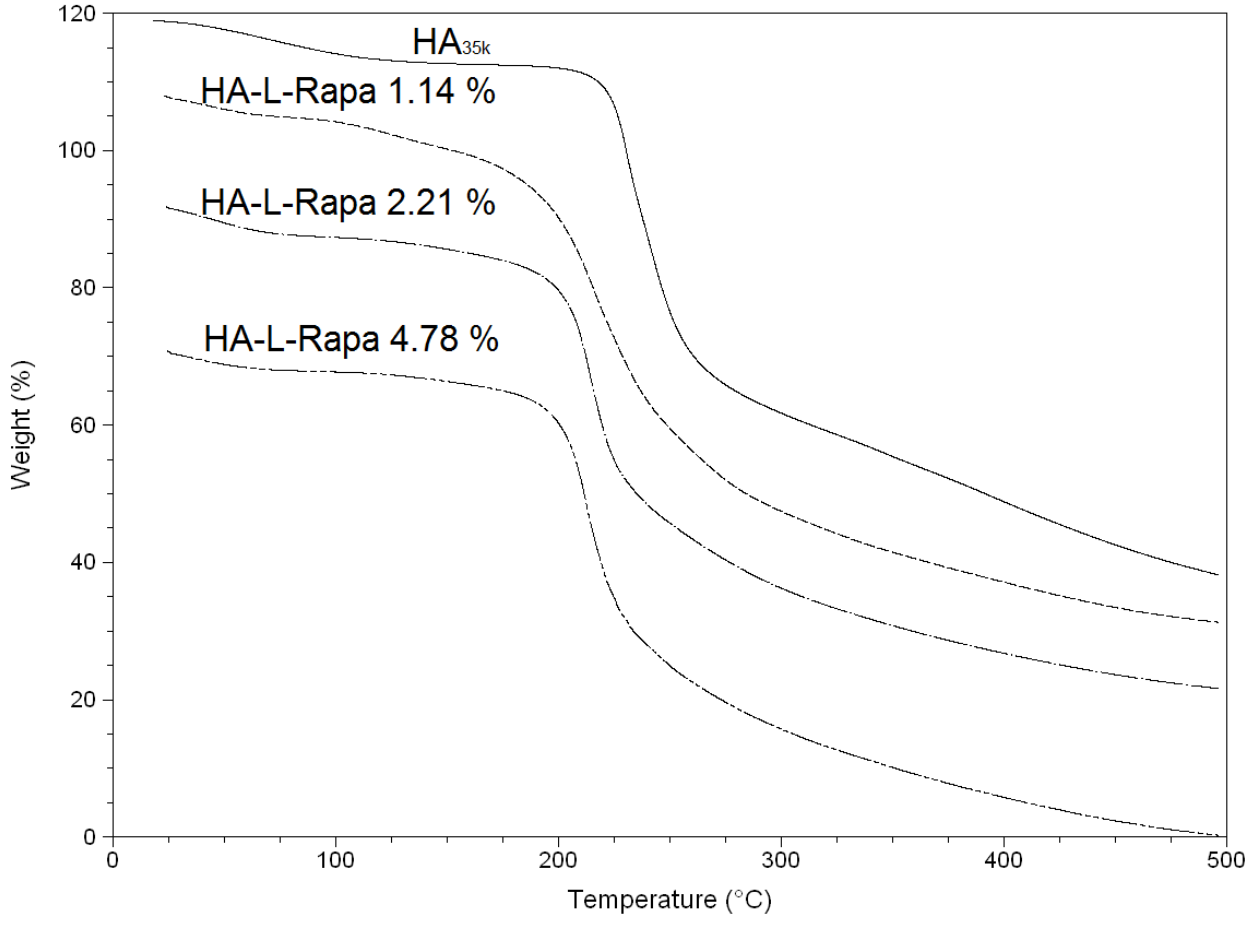

Fig. 4: TGA analysis of HA_{35k} and different loading degree HA-L-Rapa. (A) HA_{35k}; (B) HA-L-Rapa 1.14 % (w/w %); (C) HA-L-Rapa 2.21 % (w/w %); (D) HA-L-Rapa 4.78 % (w/w %).

The first transition region corresponds to the loss of water bonded to the HA molecule. The degradation temperatures of HA-L-Rapa conjugates were lower and the weight losses were smaller compared to HA_{35k}. This trend is consistent with the DSC data, and it can be explained by that the water content was decreased when the hydrophobic molecules were conjugated on the HA surface. The second transition region is polymer degradation. The TGA plots illustrated that the weight loss was decreased with higher drug conjugated HA. This is also consistent with DSC data that the enthalpy at this region was increased with the drug loading degree.

4.3.4 Flow Cytometry

The expression of CD44 receptors on MDA-MB-468 cells was studied by flow cytometry. The cells were directly stained with PE-CD44 antibody and the PE-IgG1 isotope was used as a control (Fig. 5). Protein quantification by flow cytometry demonstrated that the percentage of CD44 positive cells in MDA-MB-468 and 4T1.2neu was 99.92 % and 89.59 %, respectively. When MDA-MB-468 CD44 binding sites were blocked with H-CAM, the percentage of active sites decreased to 0.57 %. This result indicated that H-CAM can be used as an inhibitor to block the receptor-mediated endocytosis of HA.

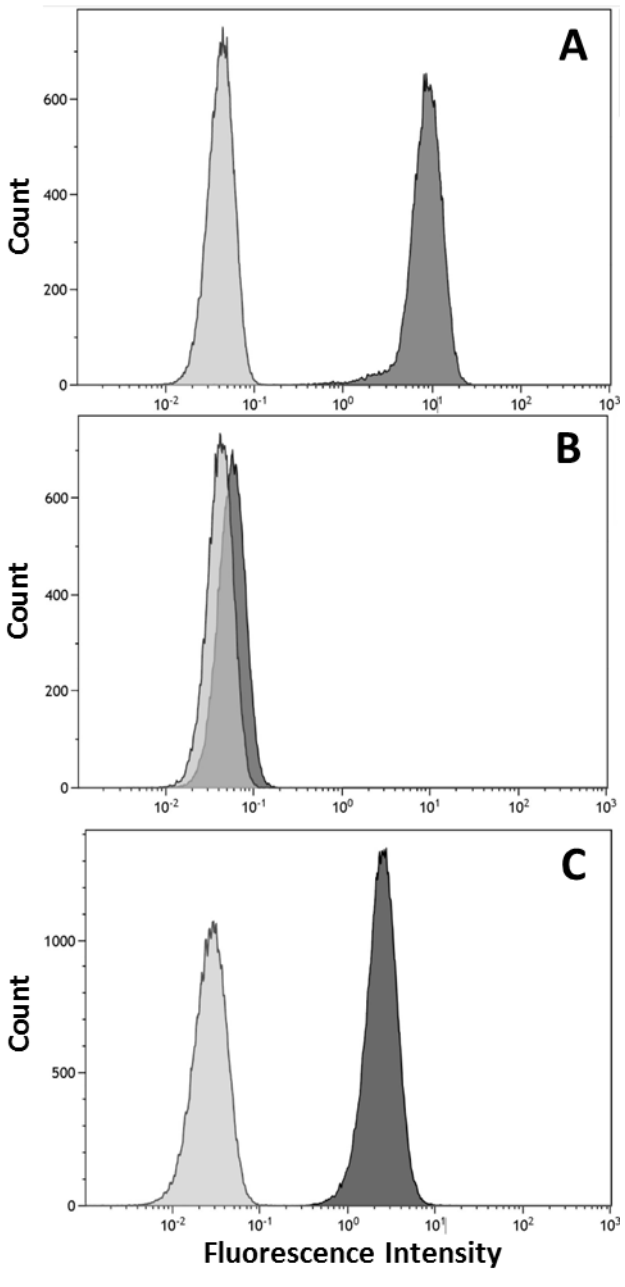

Fig. 5: Flow cytometry analysis of available CD44 receptor binding sites on the cell surface. (A) MDA-MB-468 stained with PE anti-CD44 antibody (dark grey) and PE IgGI isotope (light grey); (B) MDA-MB-468 treated with H-CAM and stained with PE anti-CD44 antibody (dark grey) and PE IgGI isotope (light grey); (C) 4T1.2neu stained with PE anti-CD44 antibody (dark grey) and PE IgGI isotope (light grey).

4.3.5 *In Vitro* Efficacy Study

4.3.5.1 Cytotoxicity

Cytotoxicity of unconjugated rapamycin and HA-L-Rapa at different concentrations was determined in MDA-MB-468 cells with or without H-CAM treatment (Fig. 6). In CD44 positive MDA-MB-468 cells, HA-L-Rapa decreased cell-viability by 8.72 % compared to rapamycin (p = 0.027) at 10 μM. The addition of H-CAM blocked CD44-mediated uptake and there was no significant difference in cell viability between HA-L-Rapa and the free drug (p = 0.065).

4.3.5.2 Cellular Uptake Analysis

MDA-MB-468 cells with or without H-CAM in a 12-well plate were treated with free rapamycin or HA-L-Rapa at a drug concentration of 10 μM. Drug concentration in the cell culture medium was analyzed by HPLC (Fig. 7). In CD44 positive cells, the polymer drug conjugate significantly improved the drug uptake by 3.2 times compared to the free rapamycin (p = 0.012). When CD44 was blocked with H-CAM, there was no difference in rapamycin uptake between the free drug and polymer conjugate groups (p = 0.13).

4.3.6 Pharmacokinetics Evaluation

The pharmacokinetics of free rapamycin (i.p.) and HA-L-Rapa (s.c.) were compared in female Sprague-Dawley rats (n = 3). A two-compartment pharmacokinetic model was selected to describe the exponential nature of the pharmacokinetics disposition of the drug (Fig. 8). The area under the plasma concentration time curve ($AUC_{0\rightarrow\infty}$) of rats administrated with HA-L-Rapa was 2.78-fold greater than that of the free drug, and the concomitant total body clearance was 2.09-fold slower (Table 3).

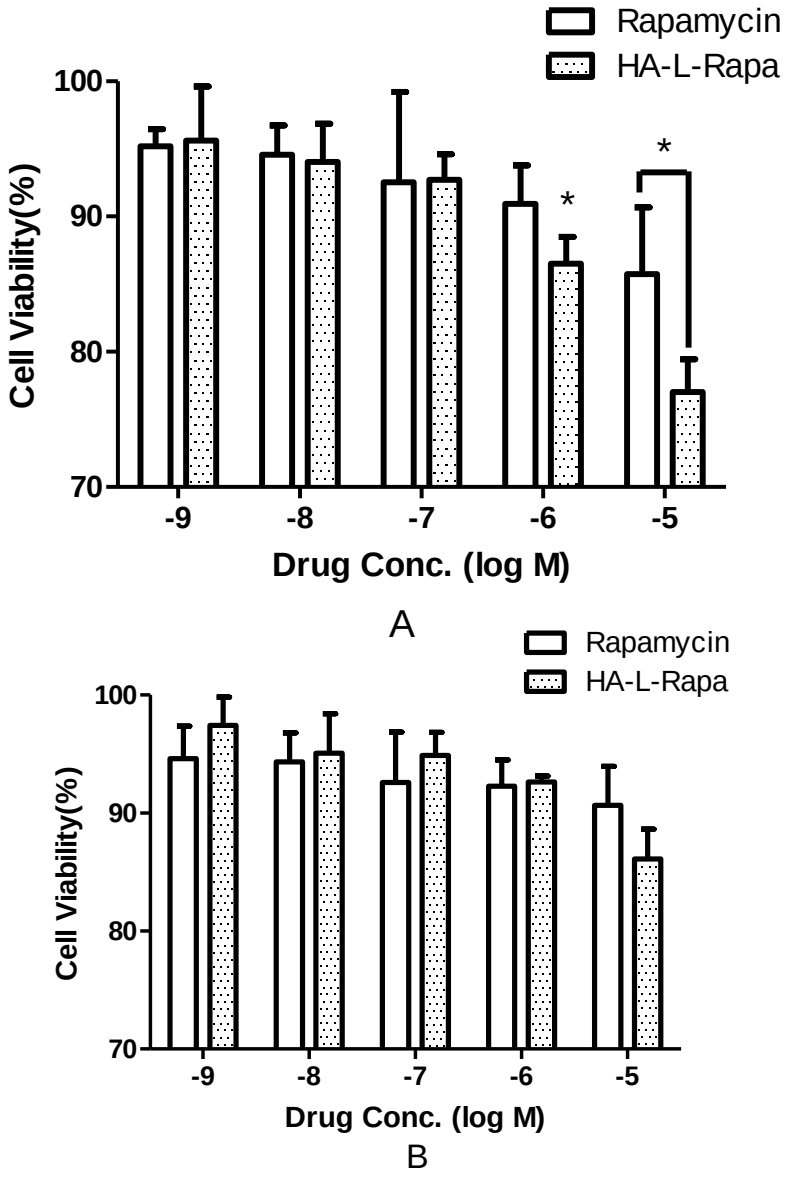

Fig. 6: Cell viability assay of free rapamycin and HA-L-Rapa in MDA-MB-468 cells (A) CD44 positive cells and (B) with H-CAM blocking of CD44 (Mean ± SD) (*, $p < 0.05$).

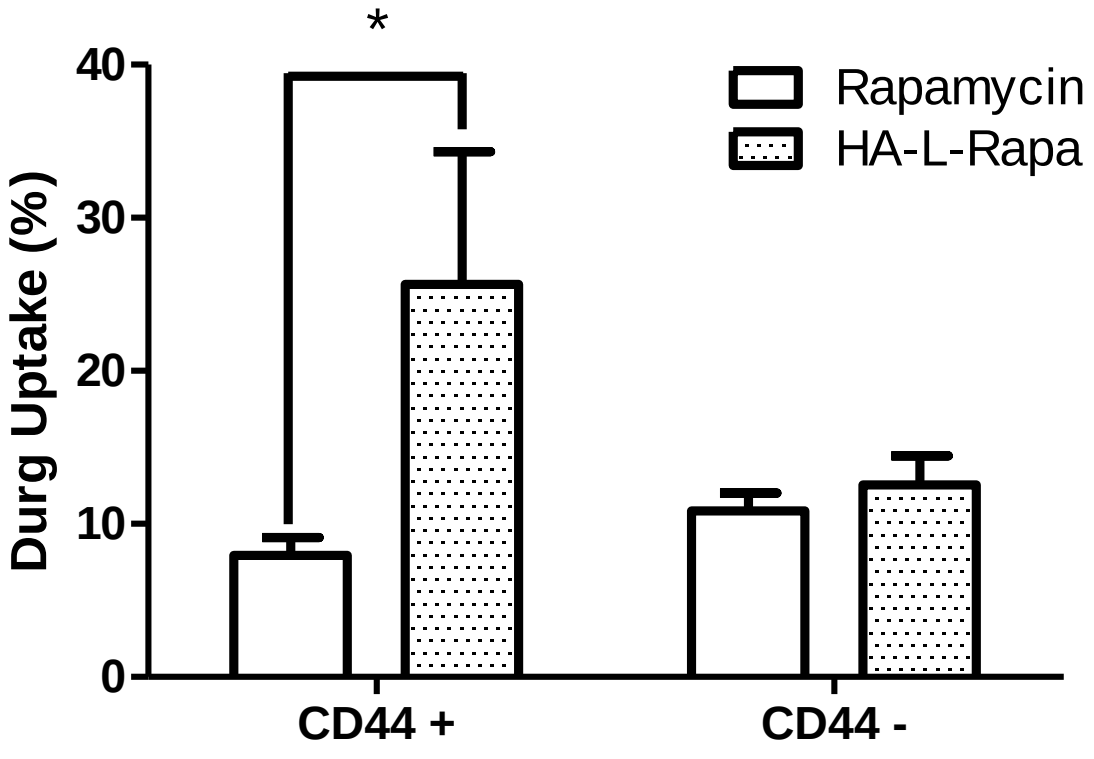

Fig. 7: HA-L-Rapa formulation improved CD44+ cells' uptake of the drug (mean ± SD) (*: $p < 0.05$).

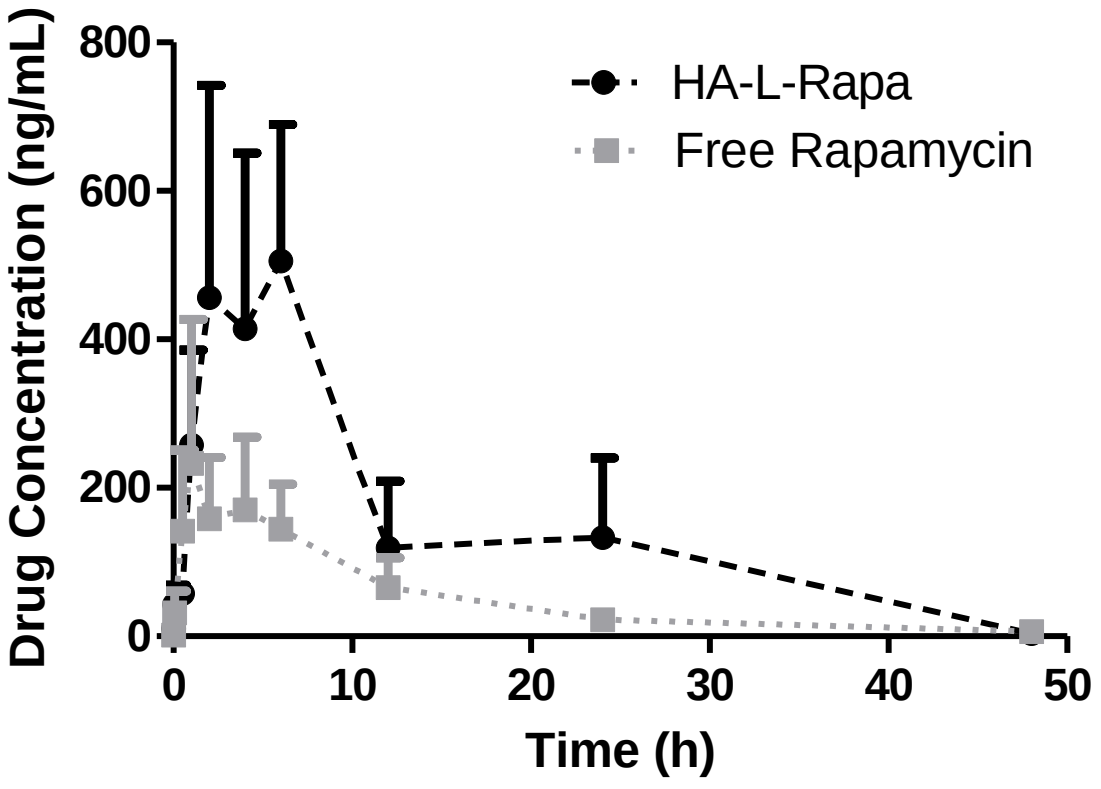

Fig. 8: Plasma rapamycin concentration versus time disposition (Mean ± SD, n = 3).

Table 3: Pharmacokinetic parameters after i.p. free rapamycin and s.c. HA-L-Rapa. (Mean ± SD, n = 3) (*: $p < 0.05$; **: $p < 0.01$)

Parameters	Unit	Free Rapamycin i.p.	HA-L-Rapa s.c.
V_d	L/kg	37.68 ± 15.49	12.88 ± 5.24*
$AUC_{0\rightarrow\infty}$	(µg·h)/mL	2.36 ± 0.46	6.57 ± 0.92**
Cl	L/(kg·h)	4.23 ± 0.95	2.02 ± 0.73**
C_{max}	ng/mL	172.86 ± 69.06	544.84 ± 123.56*
$t_{1/2}$	h	10.49 ± 3.76	27.95 ± 13.33*

4.3.7 Animal Survival and Tumor Suppression Studies

BALB/c mice were inoculated with 4T1.2neu cells to evaluate the attenuation effect of HA-L-Rapa on overall tumor progression. The median survival times of control, free rapamycin and HA-L-Rapa treatment groups were 17, 15 and 22 days, respectively (Fig. 9). Regression analysis demonstrated that HA-L-Rapa treatment was associated with significantly longer survival of mice with mouse mammary carcinoma compared with both the untreated control group (p = 0.047) and free drug treatment group (p = 0.018).

The *in vivo* 4T1.2neu breast cancer model also illustrated a significant decrease (p = 0.049) in tumor volume on day 20 in BALB/c mice treated with HA-L-Rapa (10 mg/kg equivalent rapamycin) compared with that of the control group. Free rapamycin (10 mg/kg) also decreased tumor volume; however, the difference was not significant (p = 0.056).

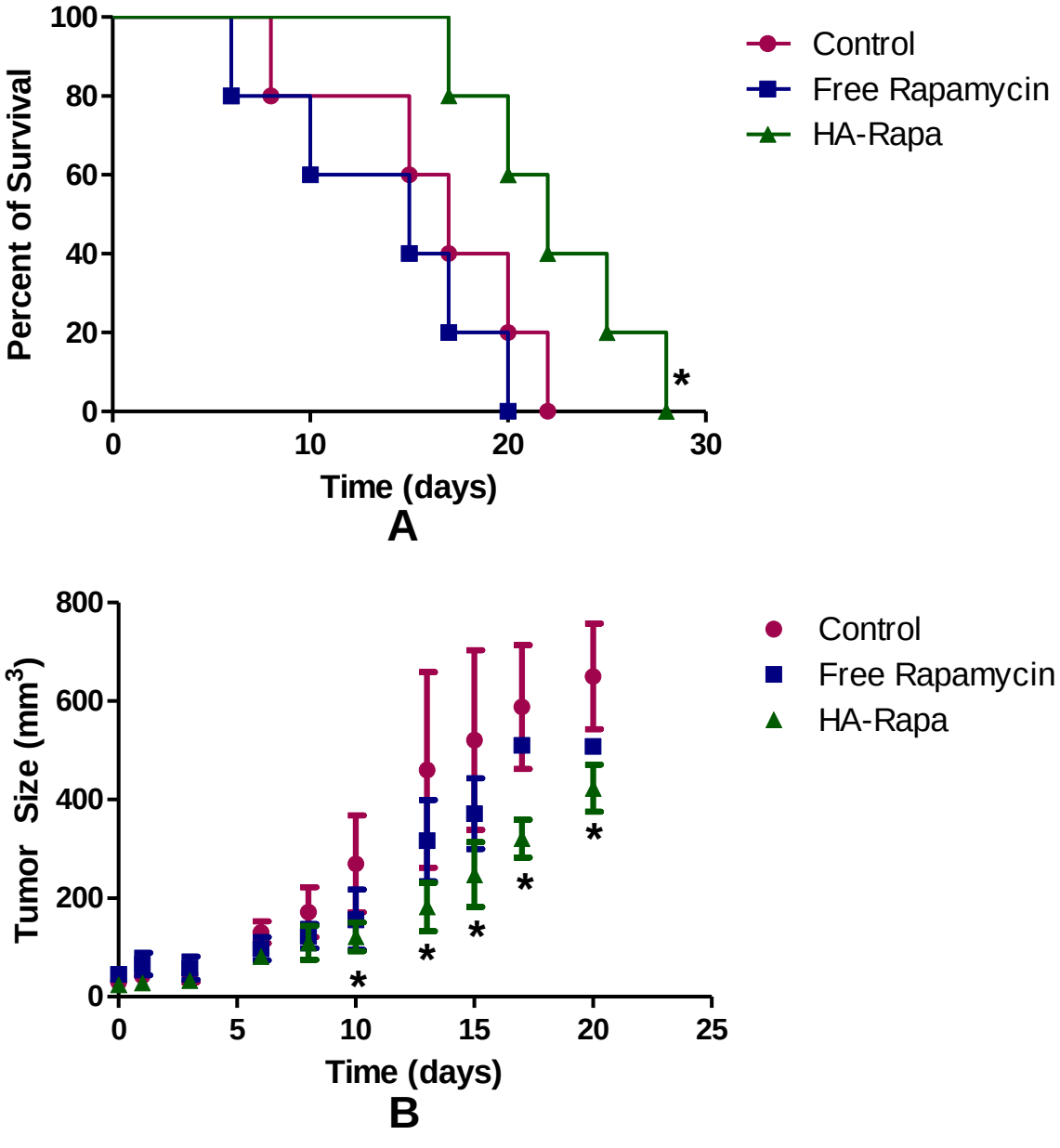

Fig. 9: HA-Rapa significantly improved animal survival (A) and suppressed tumor progression (B) in BALB/c mice with 4T1.2neu breast cancer (Mean ± SD) (n = 5; *, $p < 0.05$).

4.3.8 Tissue Distribution

Twelve hours after s.c injection of HA-L-Rapa, the drug concentrations in tumor, lymph and lung were 1.56, 2.78 and 3.23-fold greater than the free drug treatment group (Table 4). The order of drug concentrations for the control group, free rapamycin (i.p.), were tumor > lymph > lungs > kidneys > heart > liver > muscle > spleen > brain. The drug concentration of HA-L-Rapa (s.c.) formulation were lungs > lymph > tumor > spleen > muscle > liver > kidneys > heart > brain.

4.4 Discussion

In this study, we described the use of hyaluronic acid as a drug delivery carrier that can enhance the efficacy of the conjugated rapamycin against CD44 positive cancer cells. Previously in our lab, we showed that the $t_{50\%}$ of the lymphatic drainage of medium length HA (35 kDa – 74 kDa) to the axillary lymph node was 15 -17 h and the t_{max} was around 2 h (31). The release half-life of rapamycin from HA-Temsirolimus in PBS was approximately 4 h. The bulk of the drug would therefore be released before the polymer cleared from the target site. However, the sustained release characteristics can be improved by using 3-amino-4-methoxy-benzoic acid instead of ADH as a linker to conjugate the drug (HA-L-Rapa). This can be explained as HA-Temsirolimus was prepared using an unhindered ester, which allows rapid hydrolysis and release of the drug in water and serum. In comparison, the ester bond in HA-L-Rapa is stabilized by the para site methoxy group on the benzene ring that served as a strong electron donating group and reduced the hydrolysis rate. In addition, the ester bond in HA-L-Rapa was more hindered and the drug was in a more rigid condition. These structural configurations provided a more hydrophobic environment than that of HA-Temsirolimus, which may limit access by serum

Table 4: Mean concentration of rapamycin in mice tissues measured at 12 h post administration of 10 mg/kg equivalent rapamycin by i.p. (free rapamycin) and s.c. (HA-L-Rapa) injection. (Mean ± SD, n = 5) (*, $p < 0.05$; **, $p < 0.01$)

Tissue	Free Rapamycin (µg/g)	HA-L-Rapa (µg/g)
Brain	107.69 ± 37.25	195.01 ± 48.56*
Kidneys	469 ± 27.27	495.04 ± 349.05
Tumor	1237.01 ± 256.20	1931.84 ± 195.46**
Lymph	705.28 ± 115.87	1972.78 ± 634.80**
Heart	440.73 ± 81.57	358.88 ± 110.31
Liver	378.72 ± 40.56	565.56 ± 54.06*
Lungs	617.53 ± 298.54	1990.00 ± 634.80**
Muscle	315.56 ± 154.12	927.64 ± 453.48*
Spleen	183.91 ± 66.46	1386.31 ± 342.71**

esterase. The release half-life was increased to approximately 36 h in serum supplemented PBS. This could provide a sustained release of the drug at the targeted tissue and minimize the systemic toxicity by reducing the necessary drug dose and limiting drug non-targeted tissue exposure.

Low molecular weight HA (less than 10 kDa) was reported to reversibly bind CD44 and is associated with immunogenicity. However, higher molecular weight HA (greater than 30 kDa) binds irreversible to CD44 due to the increased multivalent interactions (32). The 35-kDa HA used in this study has approximately 87 D-glucuronic acid repeating units. The 2.6 % w/w loading is equivalent to one rapamycin per one polymer chain, so over 98 % of the glucuronic side chains are available for binding CD44.

The *in vitro* results of the antibody blocking studies showed that the internalization of HA-drug conjugate was inhibited by the H-CAM CD44 inhibitor, which blocked endocytosis and CD44 specific uptake. Since HA-L-Rapa entered the cells through an endocytic pathway, inhibition of this pathway resulted in a reduction of the internalization degree of the polymer drug conjugate. Cellular uptake of the lipid permeable free drug is driven by a concentration gradient. After equilibrium is established, no more drug is able to enter cells, hence inhibition of CD44 receptor did affect free rapamycin uptake by MDA-MB-468 cells. Receptor mediated transport of HA-L-Rapa improved drug delivery in CD44 positive cells and the cytotoxicity was also significantly enhanced. These results also indicated that conjugate of rapamycin does not inhibit the HA-CD44 interaction at the amounts studied; this strategy could be utilized as a novel drug delivery platform for targeted chemotherapy with rapamycin.

This study limited rapamycin to i.p. injection and the conjugate to local s.c. administration. Rapamycin is poorly water soluble and no safe i.v. formulation has been reported. Clinical trials of i.v. rapamycin resulted in injury (swelling and focal lesion) at the injection site, lymphoid atrophy and periarterial edema in the heart, liver (FDA NDA 21-083). Our own previous rat studies demonstrated significant morbidity and a 40 % mortality of i.v. rapamycin in rats (30). Rapamycin cannot be given subcutaneously repeatedly and safely as the free drug. Myckatyn reported skin ulceration in mice administrated 2 mg/kg rapamycin (one fifth of our dose), and given the ulceration potential of the 4T1.2neu model, this control study was not permitted by institutional animal care guidelines (33). Therefore, in this study, intravenous administration of rapamycin was not investigated.

The pharmacokinetics profile of s.c. HA-L-Rapa was greatly altered compared to the standard i.p. free rapamycin formulation. The high value of V_d of free rapamycin results from its lipophilicity and thus high tissue distribution. The HA conjugate significantly reduced the volume distribution possibly by minimizing nonspecific tissue binding. The increased AUC and slower clearance rate of s.c. HA-L-Rapa are consistent with the sustained release of the drug from the conjugate.

HA targets to CD44 receptors and could specifically bind to CD44 positive cells. HA molecules are uptake by the cells through CD44 receptor-mediated endocytosis followed by lysosomal degradation. The distribution of rapamycin in the HA-L-Rapa treated mice was mainly in the tumor. The significant improvement in exposure drug in target tissues by HA-L-Rapa suggested that a lower dose of rapamycin may achieve a therapeutic effect.

In addition, the 4T1 is a highly metastatic cancer cell line (34). At necropsy, lung metastases were observed in 5/5 of the free rapamycin group and only 1/5 of the HA-L-Rapa group. This is consistent with that more drug was detected in HA-L-Rapa treated animals' lungs. The lung accumulation can be explained by the prevalence of four major HA-binding proteins that potentially contributed to lung pathology regulation: CD44, toll-like receptor (TLR4), HA-binding protein 2 (HABP2) and receptor for HA-mediated motility (RHAMM) (35). Meanwhile, HA constitutes the major glycosaminoglycan in lung tissue and it has diverse function in lung homeostasis and pulmonary disease.

HA is cleared from tissues mainly by the lymphatic system due to the presence of lymphatic endothelial hyaluronan receptor, LYVE-1 (36). The expression of LYVE-1 is largely restricted to lymphatic vessels and splenic sinusoidal endothelia cells (37). The LYVE-1 receptor has a 41 % homology to the HA-binding CD44 receptor. This provided an additional HA targeting mechanism. It is consistent with HA-L-Rapa treated mice, where more drug accumulated in the lymph node and the spleen compared to the free drug treatment group.

The breast cancer cell line, 4T1, has an inherent propensity of ulceration (38). Our data illustrated that HA-L-Rapa treatment significantly inhibited tumor growth and diminished the incidence of ulcerated tumor in mammary carcinoma bearing mice. The free rapamycin treatment group showed smaller tumor sizes compared to the non-treatment group. However, the animals were sacrificed due to the presence of hemorrhagic skin ulcers and there was no statically significant survival benefit compared to saline.

Rapamycin is a promising therapeutic agent with both immunosuppressant (mTOR inhibitor) and anti-tumor activities. The immunosuppressant effect of rapamycin comes from the inhibition of T and B cell proliferation (39, 40), which is the same mechanism of anticancer activity. However, based on currently available evidence, the anti-neoplastic activity is more dominant than that of immunosuppressant effects (41). In our study, we developed a formulation that can target the drug specifically to the tumor and lymphatic tissue via a CD44 interaction. This could further minimize the systemic immunosuppressant activity of rapamycin and augment the anti-cancer effects of the drug.

4.5 Conclusion

We have developed a novel HA-rapamycin conjugate for treating localized CD44 positive cancer. To conjugate rapamycin to HA, two formulation strategies were developed and compared. We found that the polymer-drug conjugate prepared by 3-amino-4-methoxy-benzoic acid released the drug in a sustained fashion. *In vitro* cell line based studies showed that HA-L-Rapa entered the cells via CD44 mediated endocytosis. *In vivo* animal studies indicated that HA-L-Rapa improved animal survival rate and suppressed tumor progression in BALB/c mice. These results suggest that the HA rapamycin conjugate could be used as a potential therapeutic agent for CD44 positive cancers.

4.6 References

1. J.S. Chan, H.A. Robertson, and H.G. Friesen. The purification and characterization of ovine placental lactogen. Endocrinology. 98:65-76 (1976).

2. G. Tzircotis, R.F. Thorne, and C.M. Isacke. Chemotaxis towards hyaluronan is dependent on CD44 expression and modulated by cell type variation in CD44-hyaluronan binding. Journal of cell science. 118:5119-5128 (2005).
3. B.L. Lokeshwar, V.B. Lokeshwar, and N.L. Block. Expression of CD44 in prostate cancer cells: association with cell proliferation and invasive potential. Anticancer research. 15:1191-1198 (1995).
4. E. Olsson, G. Honeth, P.O. Bendahl, L.H. Saal, S. Gruvberger-Saal, M. Ringner, J. Vallon-Christersson, G. Jonsson, K. Holm, K. Lovgren, M. Ferno, D. Grabau, A. Borg, and C. Hegardt. CD44 isoforms are heterogeneously expressed in breast cancer and correlate with tumor subtypes and cancer stem cell markers. BMC cancer. 11:418 (2011).
5. S. Misra, P. Heldin, V.C. Hascall, N.K. Karamanos, S.S. Skandalis, R.R. Markwald, and S. Ghatak. Hyaluronan-CD44 interactions as potential targets for cancer therapy. The FEBS journal. 278:1429-1443 (2011).
6. S.C. Ghosh, S. Neslihan Alpay, and J. Klostergaard. CD44: a validated target for improved delivery of cancer therapeutics. Expert opinion on therapeutic targets. 16:635-650 (2012).
7. C. Liand S. Wallace. Polymer-drug conjugates: recent development in clinical oncology. Advanced drug delivery reviews. 60:886-898 (2008).
8. A.K. Shakyaand K.S. Nandakumar. Applications of polymeric adjuvants in studying autoimmune responses and vaccination against infectious diseases. Journal of the Royal Society, Interface / the Royal Society. 10:20120536 (2013).
9. R. Duncan. Polymer therapeutics as nanomedicines: new perspectives. Current opinion in biotechnology. 22:492-501 (2011).

10. P.J. Mease. Certolizumab pegol in the treatment of rheumatoid arthritis: a comprehensive review of its clinical efficacy and safety. Rheumatology (Oxford). 50:261-270 (2011).
11. S.D. Chipman, F.B. Oldham, G. Pezzoni, and J.W. Singer. Biological and clinical characterization of paclitaxel poliglumex (PPX, CT-2103), a macromolecular polymer-drug conjugate. International journal of nanomedicine. 1:375-383 (2006).
12. W.B. Liechty, D.R. Kryscio, B.V. Slaughter, and N.A. Peppas. Polymers for drug delivery systems. Annual review of chemical and biomolecular engineering. 1:149-173 (2010).
13. G. Pasutand F.M. Veronese. PEG conjugates in clinical development or use as anticancer agents: an overview. Advanced drug delivery reviews. 61:1177-1188 (2009).
14. A. Jainand S.K. Jain. PEGylation: an approach for drug delivery. A review. Critical reviews in therapeutic drug carrier systems. 25:403-447 (2008).
15. M.J. Vicent, L. Dieudonne, R.J. Carbajo, and A. Pineda-Lucena. Polymer conjugates as therapeutics: future trends, challenges and opportunities. Expert opinion on drug delivery. 5:593-614 (2008).
16. A. Vaidya, A. Agarwal, A. Jain, R.K. Agrawal, and S.K. Jain. Bioconjugation of polymers: a novel platform for targeted drug delivery. Current pharmaceutical design. 17:1108-1125 (2011).
17. W. Du, D. Gerald, C.A. Perruzzi, P. Rodriguez-Waitkus, L. Enayati, B. Krishnan, J. Edmonds, M.L. Hochman, D.C. Lev, and T.L. Phung. Vascular tumors have increased p70 S6-kinase activation and are inhibited by topical rapamycin. Laboratory investigation; a journal of technical methods and pathology(2013).

18. Y. Geand J. Chen. Mammalian target of rapamycin (mTOR) signaling network in skeletal myogenesis. The Journal of biological chemistry. 287:43928-43935 (2012).

19. P.M. LoRusso. Mammalian target of rapamycin as a rational therapeutic target for breast cancer treatment. Oncology. 84:43-56 (2013).

20. L. Liu, N. Wu, and J. Li. Novel targeted agents for gastric cancer. Journal of hematology & oncology. 5:31 (2012).

21. Z.Z. Chong, Y.C. Shang, and K. Maiese. Cardiovascular disease and mTOR signaling. Trends in cardiovascular medicine. 21:151-155 (2011).

22. Y. Kamada, T. Funakoshi, T. Shintani, K. Nagano, M. Ohsumi, and Y. Ohsumi. Tor-mediated induction of autophagy via an Apg1 protein kinase complex. The Journal of cell biology. 150:1507-1513 (2000).

23. Y. Zhaoand Y. Sun. Targeting the mTOR-DEPTOR pathway by CRL E3 ubiquitin ligases: therapeutic application. Neoplasia. 14:360-367 (2012).

24. C. Cabrera-Lopez, T. Marti, V. Catala, F. Torres, S. Mateu, J. Ballarin, and R. Torra. Assessing the effectiveness of rapamycin on angiomyolipoma in tuberous sclerosis: a two years trial. Orphanet journal of rare diseases. 7:87 (2012).

25. M.J. Kaplan, C.N. Ellis, Z. Bata-Csorgo, R.S. Kaplan, J.L. Endres, and D.A. Fox. Systemic toxicity following administration of sirolimus (formerly rapamycin) for psoriasis: association of capillary leak syndrome with apoptosis of lesional lymphocytes. Archives of dermatology. 135:553-557 (1999).

26. B. Tyler, S. Wadsworth, V. Recinos, V. Mehta, A. Vellimana, K. Li, J. Rosenblatt, H. Do, G.L. Gallia, I.M. Siu, R.T. Wicks, M.A. Rudek, M. Zhao, and H. Brem.

Local delivery of rapamycin: a toxicity and efficacy study in an experimental malignant glioma model in rats. Neuro-oncology. 13:700-709 (2011).

27. J. Gu, M.E. Ruppen, and P. Cai. lipase-catalyzed regioselective esterification of rapamycin: synthesis of temsirolimus (CCI-779). Organic letters. 7:3945-3948 (2005).

28. A. Hioki, A. Wakasugi, K. Kawano, Y. Hattori, and Y. Maitani. Development of an in vitro drug release assay of PEGylated liposome using bovine serum albumin and high temperature. Biological & pharmaceutical bulletin. 33:1466-1470 (2010).

29. T.L. Doane, C.H. Chuang, R.J. Hill, and C. Burda. Nanoparticle zeta -potentials. Accounts of chemical research. 45:317-326 (2012).

30. J.A. Yanez, M.L. Forrest, Y. Ohgami, G.S. Kwon, and N.M. Davies. Pharmacometrics and delivery of novel nanoformulated PEG-b-poly(epsilon-caprolactone) micelles of rapamycin. Cancer chemotherapy and pharmacology. 61:133-144 (2008).

31. S.C. Taryn R. Bagby, Shaofeng Duan, Sharadvi Thati, Daniel J. Aires, M. Larid Forrest. Impact of Molecular Weight on Lymphatic Drainage of a Biopolymer-Based Imaging Agent. Pharmaceutics. 4:276-296 (2012).

32. P.M. Wolny, S. Banerji, C. Gounou, A.R. Brisson, A.J. Day, D.G. Jackson, and R.P. Richter. Analysis of CD44-hyaluronan interactions in an artificial membrane system: insights into the distinct binding properties of high and low molecular weight hyaluronan. The Journal of biological chemistry. 285:30170-30180 (2010).

33. T.M. Myckatyn, R.A. Ellis, A.G. Grand, S.K. Sen, J.B. Lowe, 3rd, D.A. Hunter, and S.E. Mackinnon. The effects of rapamycin in murine peripheral nerve

isografts and allografts. Plastic and reconstructive surgery. 109:2405-2417 (2002).

34. O. Hussein, K. Tiedemann, M. Murshed, and S.V. Komarova. Rapamycin inhibits osteolysis and improves survival in a model of experimental bone metastases. Cancer letters. 314:176-184 (2012).

35. F.E. Lennonand P.A. Singleton. Role of hyaluronan and hyaluronan-binding proteins in lung pathobiology. American journal of physiology Lung cellular and molecular physiology. 301:L137-147 (2011).

36. D.G. Jackson. Biology of the lymphatic marker LYVE-1 and applications in research into lymphatic trafficking and lymphangiogenesis. APMIS : acta pathologica, microbiologica, et immunologica Scandinavica. 112:526-538 (2004).

37. K. Leung. Hyaluronan conjugated with IR-783. Molecular Imaging and Contrast Agent Database (MICAD), Bethesda (MD), 2004.

38. M.K. Wendt, J. Molter, C.A. Flask, and W.P. Schiemann. In vivo dual substrate bioluminescent imaging. Journal of visualized experiments : JoVE(2011).

39. F.J. Dumontand Q. Su. Mechanism of action of the immunosuppressant rapamycin. Life sciences. 58:373-395 (1996).

40. J.E. Kay, L. Kromwel, S.E. Doe, and M. Denyer. Inhibition of T and B lymphocyte proliferation by rapamycin. Immunology. 72:544-549 (1991).

41. B.K. Law. Rapamycin: an anti-cancer immunosuppressant? Critical reviews in oncology/hematology. 56:47-60 (2005).

Chapter 5

Bioavailability Enhancing Strategy for Oral Administration of Doxorubicin

5.1 Introduction

Doxorubicin (DOX), also known as Adriamycin, is an anthracycline antibiotic with anti-cancer activity. DOX is isolated from *Streptomycin peucetius* and it is a 14-hydroxyalted congener of daunorubicin. It has been commonly used in the treatment of a wide variety of cancers, including ovarian cancer (1), bone and soft tissue sarcomas (2), lymphoma (3) and adrenocortical carcinomas (4). DOX can prevent DNA replication by blocking topoisomerase II activity and ultimately inhibiting protein synthesis. The planar aromatic chromophore of DOX molecule intercalates between two pairs of nucleic acids; thus, DNA transcription is blocked. The crystal structure of DOX-DNA complex showed that the six-membered duanosamine sugar sits in the DNA double helix minor groove and interacts with flanking base pairs adjacent to the intercalation site (5, 6).

DOX is a substrate of the P-glycoprotein (P-gp) efflux pump and cytochrome P450. Due to low GI absorption and first-pass metabolism, the oral bioavailability of DOX is only approximately 5 %. Therefore, DOX is formulated as hydrochloride salt and administrated by intravenous injection.

Quercetin is an important dietary flavonol derived from plants, such as fruit and vegetables. Recent studies showed that quercetin has anti-cancer, anti-viral and anti-inflammation activities (7, 8). Quercetin could induce apoptosis in certain types of cancer cells, such as H460 lung cancer cells (9), MDA-MB-231 and AU565 breast cancer cells (10), PC-3 and LNCaP prostate cancer cells (11), human 232B4 chronic lymphocytic leukemia cells (12) and C6 glioma cells (13).

The combination chemotherapy of DOX and quercetin showed significant promise in cancer treatment. When drugs that work by different mechanisms are combined, it

could decrease the likelihood of drug resistant development, and minimize the intolerable side effects in patients. The combination of DOX and quercetin studies indicated that quercetin could enhance the sensitivity of tumor cells, such as breast cancer MCF-7 and liver cancer SMMC7721, to the chemical drug and selectively induce apoptosis in cancer cells (14, 15). In addition, quercetin was reported as an inhibitor of both CYP3A4 enzyme and P-gp, which would minimize P-gp-mediated efflux and drug lost in first past metabolism (16). Besides, intraduodenally administration of quercetin in rats showed that quercetin and its deviates can be absorbed directly through intestinal cells and a higher drug concentration in lymph than in plasma was observed (17). It may provide a target delivery mechanism of the conjugated drug.

The co-administration of quercetin with anti-cancer drugs was reported as an oral bioavailability enhancing strategy. The absolute bioavailability of paclitaxel in quercetin pretreated rats was significantly higher than the control group, and both the elimination half-life and mean residence times of the drug were significantly slower (18). Besides, both the absolute and relative bioavailabilities of DOX by orally co-administered with quercetin were also found can be significantly improved (16).

In this study, a novel doxorubicin-quercetin prodrug was synthesized. Chemical and biological properties were characterized. Pharmacokinetics were examined in Sprague-Dawley rats.

5.2 Materials and Methods

5.2.1 Materials

Doxorubicin-HCl, 2 mg/mL sterile isotonic solution, was bought from Bedford Laboratories (Bedford, OH). Quercetin was purchased from INDOFINE Chemical

Co. (Hillsborough Township, NJ). H-Gly-OtBu-HCl was gotten from Bachem Americas Inc. (Torrance, CA). The chemical solvents were obtained from Fisher Scientific (Lenexa, KS). NMR spectra were collected with a 400-MHz Bruker, and the mass spectra were obtained by electrospray ionization mass spectrometry (ESI-MS).

5.2.2 Synthesis of Doxorubicin-Quercetin Prodrug

The synthetic scheme of the doxorubicin-quercetin prodrug is shown in Fig. 1.

Compound 1. All the glassware were flame dried and protected under dry argon. All the organic solvents were dried by distillation. In a round bottom flask, 3 mmol of H-Gly-OtBu-HCl, 3.3 mmol of Bis(4-nitrophenyl) and 6 mmol of N,N-Diisopropylethylamine (DIPEA) were dissolved in a mixture of THF (20 mL) and DMF (10 mL). The reaction was stirred at ambient temperature under dry argon for 24 h. Then, 3 mmol of quercetin was added. The solution was stirred at ambient temperature for an additional 24 h. After the reaction, the organic phase was concentrated under reduced pressure. The residue was purified by silica gel column chromatography and eluted with dichloromethane (DCM)-acetone (6:1) to furnish the title compound as a yellow solid (0.9 g, yield: 63.85 %).

Compound 2. Compound 1 (0.9 g) was dissolved in 10 mL of DCM on ice and 4 mL of trifluoroacetic acid (TFA) was added gradually. The reaction was stirred at ambient temperature for 2 h. The yellow precipitate was filtered and washed with DCM and acetone (0.443 g, yield: 49.26 %).

Compound 3. Doxorubicin HCl solution (2 mg/mL, 2.5 mL) was lyophilized. Compund 2 (10 mg, 2.5 eq), DIPEA (15 µL, 10 eq) and HATU (7.4 mg, 2.5 eq) were dissolved in 5 mL of DMSO. After 30 min, 5 mg of DOX lyophilized powder

was added. The reaction was stirred at ambient temperature for 24 h. The final product was purified by HPLC (Rainin Instrument Inc., Woburn, MA) with a programmable absorbance detector (Applied biosystems®, Bedford, MA) and a reverse phase semi-prep column (Phenomenex Luna® 10 μm, 250 × 10 mm, Torrance, CA). The chromatography conditions were a mobile phase A of 0.1 % formic acid in ddH_2O and B of 0.1 % formic acid in methanol (MeOH) at a flow rate of 6 mL/min. The gradient program was i) a linear gradient from 50 % to 90 % solvent B over 10 min; ii) 8 min with 90 % solvent B; iii) a liner gradient from 90 % to 10 % solvent B over 2 min; and iv) 5 min with 10 % solvent B. The retention time of the final product was 11.4 min.

5.2.3 *In vitro* drug release

The prodrug was dissolved in PBS supplemented with 10 % FBS and placed in a 37 °C water bath. After pre-determined time intervals, 100-μL aliquots from the sample tubing were analyzed by HPLC with fluorescent detector (ex/em 480/590). The release scheme of DOX and quercetin from DOX-Pro is shown in Fig. 2.

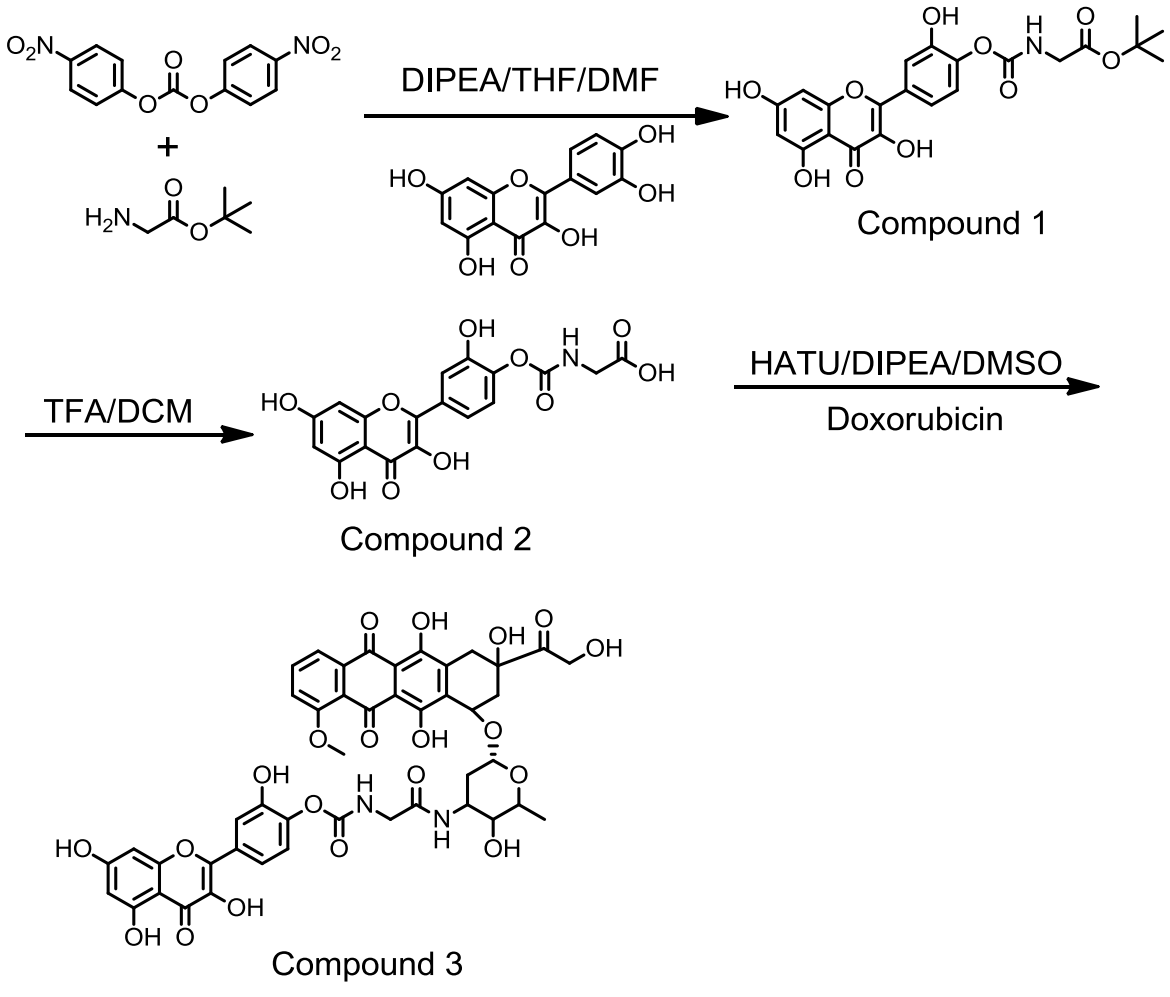

Fig. 1: Synthetic scheme of doxorubicin-quercetin prodrug.

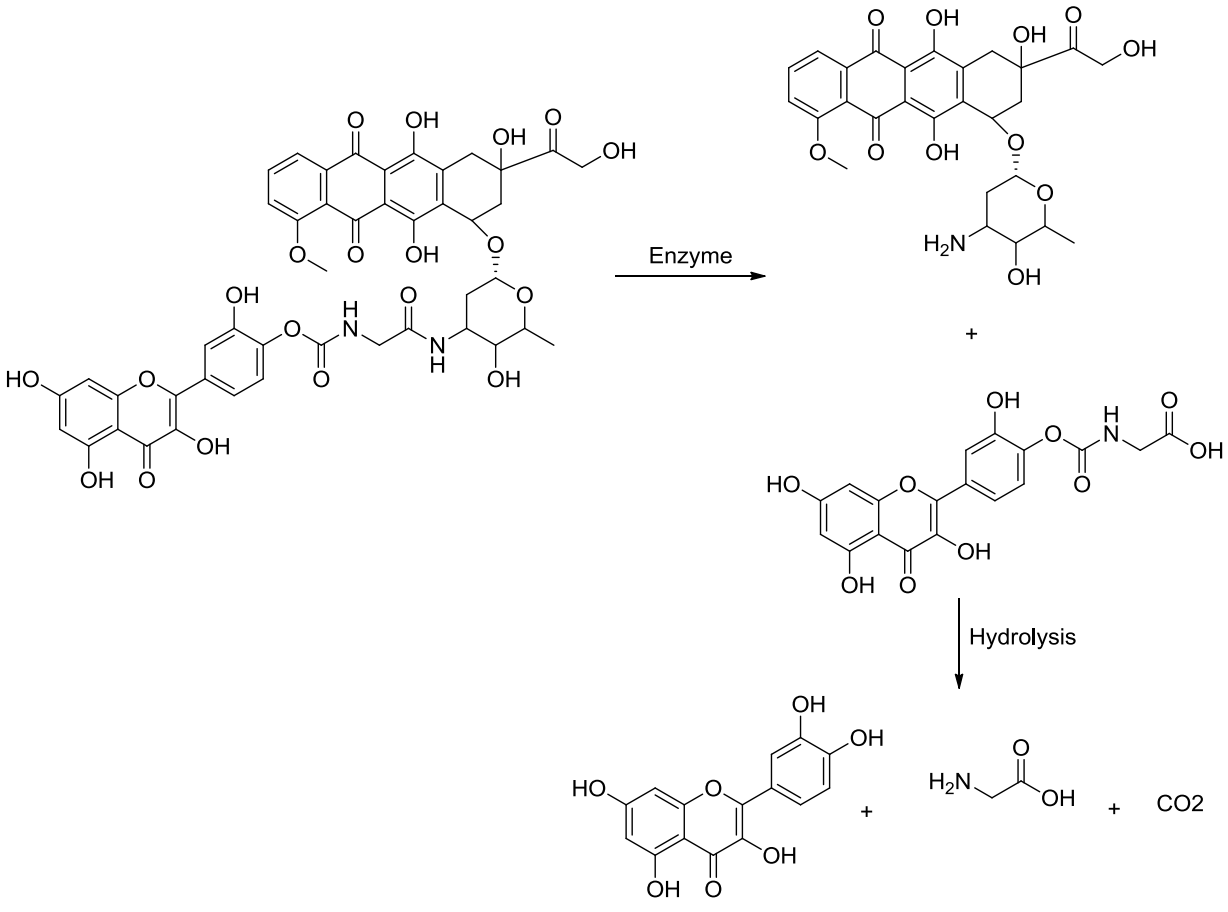

Fig. 2: The scheme of DOX and quercetin release from DOX-Pro.

5.2.4 Cellular uptake of doxorubicin by MDCK-MDR cells

Multi-drug resistant canine kidney cells (MDCK-MDR) were maintained in high glucose Dulbecco's modified eagle medium (DMEM) with 1× L-Glutamine and sodium pyruvate that was supplemented with 10 % FBS, 1× non-essential amino acid and 1× penicillin-streptomycin. Cells were seeded onto poly L-lysine pre-coated glass coverslips (BD, Franklin Lakes, NJ) in a 12-well culture plate at a density of 5000 cells/well. After 12 h, the cells were treated with 50-nM free DOX, or DOX-quercetin mixture, or DOX prodrug along with 3 μg/mL DAPI at 15 min prior to cell imaging. After the treatment, the cells were washed three times with PBS. The live cells were rapidly imaged on a Nikon Eclipse 80i epiflurescence microscope (Melville, NY) with a 20 × 0.75 NA objective and a Hamamatsu ORCA ER digital camera (Houston, TX). The GFP filter set (Nikon, NY) was used to image the fluorescence signal from DOX. All the images were taken with identical instrument settings and scaled equally so that fluorescence intensity could be compared between independent images and quantified accurately.

The cellular uptake and accumulation of DOX in MDCK-MDR cells was quantified using HPLC. The cells were seeded in a 12-well plate at a concentration of 10,000 cells/well. After the cells attached to the surface, 1-μM DOX, DOX quercetin mixture or DOX prodrug was added. After a 6-h treatment, the supernatant was removed and analyzed.

5.2.5 Pharmacokinetic study

Female Sprague-Dawley rats were administrated free DOX and doxorubicin-quercetin prodrug orally at the dosage of 10 mg/kg. Whole blood was withdrawn at 0 min, 15 min, 30 min, 1 h, 2 h, 4 h, 6 h, 12 h, 24 h and 48 h after dosing. The

whole blood was centrifuged, and the plasma was collected. Urine samples were collected at 0 h, 2 h, 6 h, 12 h, 24 h, 48 h and 72 h. The drug concentration was analyzed by a fluorophotometer (RF-5301 PC, Shimadzu). The PK parameters were calculated by WinNonlin®.

5.2.6 Statistical analysis

GraphPad Prism 5 software was used for statistical analysis. A *t*-test was used for statistical analysis between two means. In all comparisons, statistical significance was set at $p \leq 0.05$.

5.3 Results

5.3.1 DOX-Quercetin Prodrug Synthesis

Quercetin-Gly-tBu was synthesized according to the reference (19). High resolution mass spectrometry (ESI) Calc'd for $C_{22}H_{20}NO_{10}$ $(M-H)^-$: 458.1087; Found: 458.0047. ^{1}H-NMR (Acetone-d_6, 400 MHz): δ = 12.06 (s, 1H), 9.23(bs, 1H), 7.99 (d, *J* = 2.2 Hz, 1H), 7.96 (dd, *J* = 8.6, 2.1 Hz, 1H), 7.06 (d, *J* = 8.7 Hz, 1H), 6.99 (t, *J* = 6.6 Hz, 1H), 6.46 (t, *J* = 2.1 Hz, 1H), 6.21 (t, *J* = 2.1 Hz, 1H), 3.86 (d, *J* = 6.0 Hz, 2H), 1.43 (s, 9H).

Quercetin-Gly-COOH ^{1}H-NMR ^{1}H-NMR (DMSO-d_6, 400 MHz): δ = 12.69 (bs, 1H), 12.44 (s, 1H), 10.81(bs, 1H), 10.38 (bs, 1H), 9.56 (s, 1H), 8.02 (t, *J* = 6.8 Hz, 1H), 7.91 (dd, *J* = 8.6, 2.3 Hz, 1H), 7.88 (d, *J* = 2.2 Hz, 1H), 7.06 (d, *J* = 8.6 Hz, 1H), 6.47 (d, *J* = 2.0 Hz, 1H), 6.21 (d, *J* = 2.0 Hz, 1H), 3.77 (d, *J* = 6.1 Hz, 2H). HRMS (ESI) Calcd for $C_{18}H_{12}NO_{10}$ $(M-H)^-$: 402.0461; Found: 402.0419.

Quercetin-Gly-Dox ^{1}H-NMR (DMSO-d_6, 400 MHz): δ = 8.32 (s, 1H), 7.94 (t, *J* = 6.4 Hz, 1H), 7.90 (d, *J* = 1.2 Hz, 1H), 7.88 (s, 1H), 7.79 (s, 1H), 7.71 (s, 1H), 7.15 (d, *J* = 8.4 Hz, 1H), 7.06 (d, *J* = 8.4 Hz, 1H), 6.46 (s, 1H), 6.19 (s, 1H), 5.50

(s, 1H), 5.23 (s, 1H), 4.97 (s, 1H), 4.87 (s, 2H), 4.57 (s, 1H), 4.16 (s, 1H), 4.00-3.89 (m, 3H), 3.07 (s, 3H), 3.00 (s, 1H), 2.92 (s, 3H), 2.78 (d, *J* = 9.6 Hz, 1H), 2.68 (d, *J* = 6.4 Hz, 1H), 2.21-2.11 (m, 2H), 3.32 (s, 3H), 2.99-2.89 (m, 2H), 2.84-2.56 (m, 1H), 2.37-2.21 (m, 3H), 1.51-1.41 (m, 1H), 1.24 (s, 1H), 1.13 (d, *J* = 7.6 Hz, 3H). HRMS (ESI) Calcd for $C_{45}H_{39}N_2O_{20}$ $(M-H)^-$: 927.2096; Found: 927.2086.

5.3.2 Drug release study

The *in vitro* drug release profile is shown in Fig. 3. The release of DOX was due to the enzyme digestion of the amide bond. The release of DOX from the prodrug showed a first-order kinetic profile and the $t_{1/2}$ was approximately 60 h. Quercetin was released from the prodrug conjugate by hydrolysis of the carbamate bond. The quercetin exhibited second-order kinetics in aqueous medium and the release half-life was over 100 h.

5.3.3 Cellular uptake analysis

Confocal microscopy was used to examine if the prodrug would improve DOX uptake by P-gp positive cells. More fluorescence signal was detected in DOX quercetin mixture and DOX prodrug treatment groups (Fig. 4). The images were analyzed by ImageJ (Fig. 5). After 5 min treatment, there was no significant improvement of drug uptake by the cells treated with DOX-quercetin mixture compared to that of the free DOX (p = 0.595). However, the fluorescence signal was significantly enhanced in the cells treated with DOX prodrug (p = 0.0123).

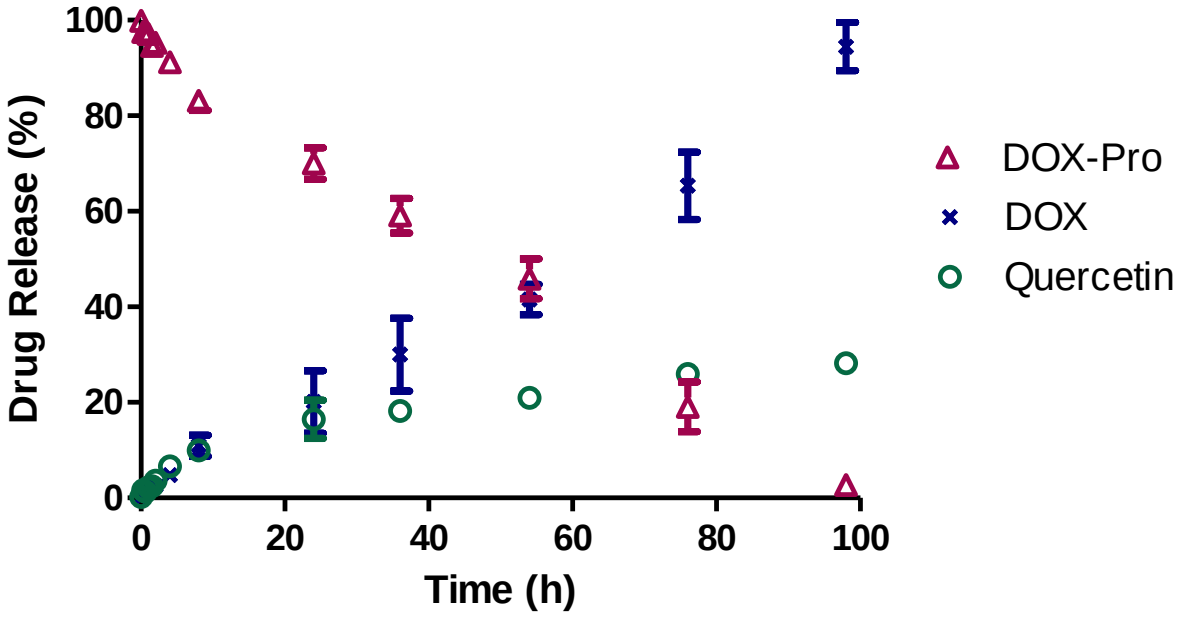

Fig. 3: *In vitro* drug release of DOX and quercetin from DOX prodrug.

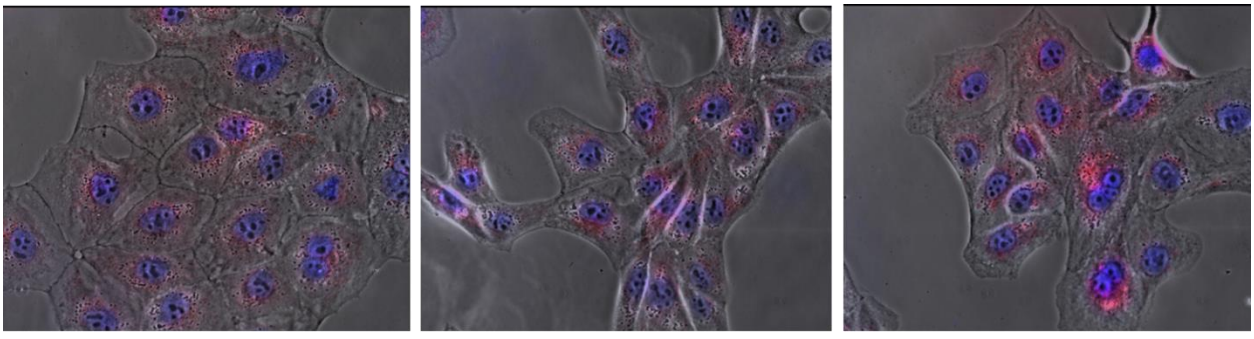

Fig. 4: Fluorescence imaging study of cell uptake of doxorubicin by MDCK-MDR cells. (A) cells were treated with 50 nM free DOX; (B) cells were treated with 50 nM DOX and 50 nM quercetin; (C) cells were treated with 50 nM DOX prodrug.

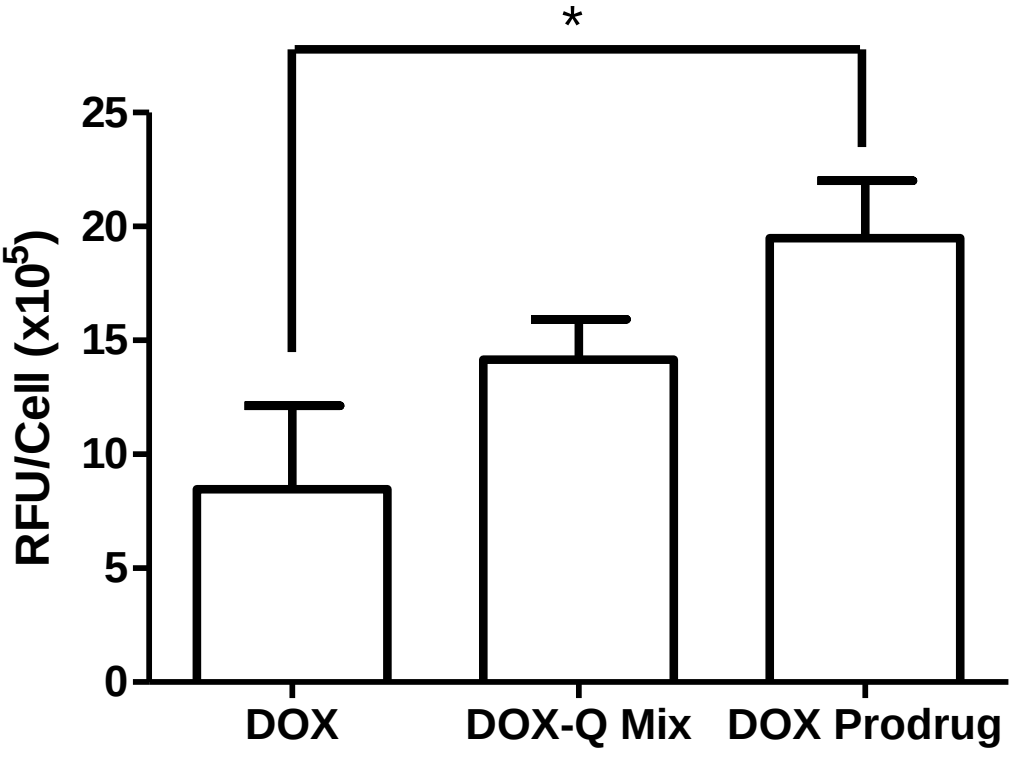

Fig. 5: The fluorescence signals of the images of MDCK-MDR cells treated by DOX, DOX-quercetin and DOX prodrug analyzed by ImageJ. (Mean ± SD, *: $p < 0.05$)

The drug uptaken by the cells quantified by HPLC is shown in Fig. 6. The prodrug formulation significantly improved drug uptake compared to both the free DOX and DOX-quercetin mixture. This is consistent with the fluorescence imaging study.

5.3.4 Pharmacokinetics in Rat Serum

The pharmacokinetics of oral administration of free DOX and doxorubicin-quercetin prodrug were compared in female Sprague-Dawley rats. Pharmacokinetics of free DOX and DOX-Pro in rat serum and urine are shown in Fig. 7. The serum pharmacokinetics parameters were calculated and listed in Table 1. The area under the plasma concentration time curve ($AUC_{0\rightarrow\infty}$) of rat administrated with the prodrug was 7.37-fold greater than that of the free DOX. The clearance was 2.87-fold slower.

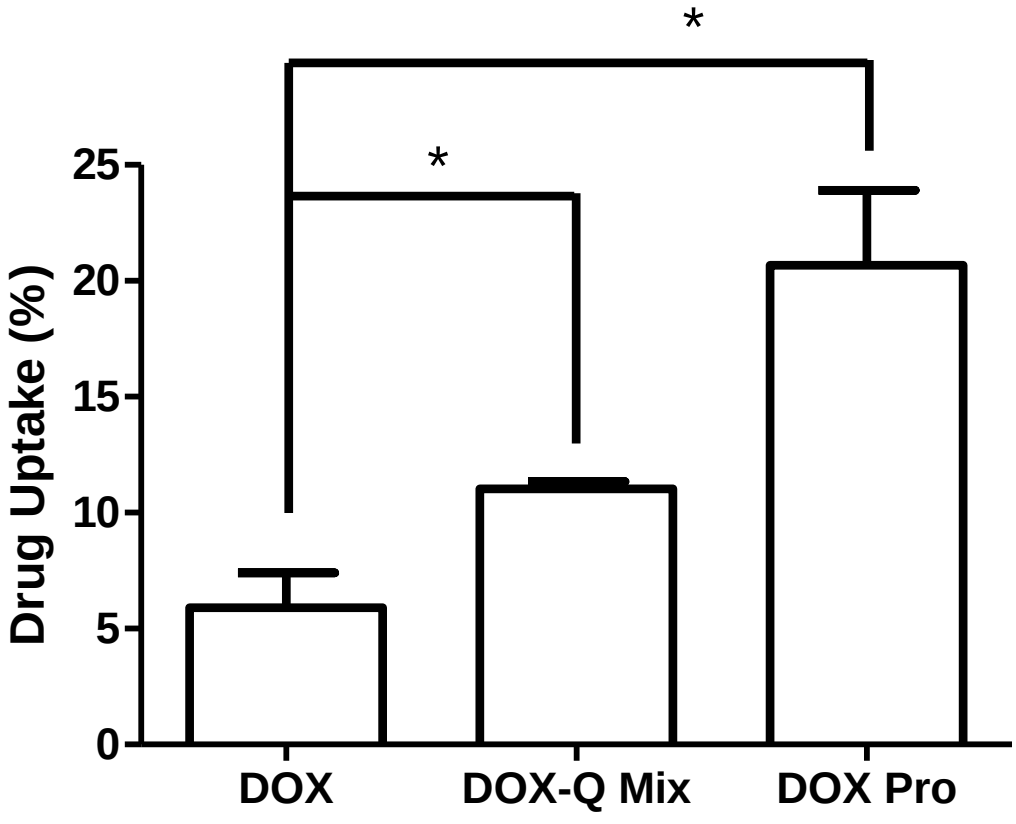

Fig. 6: Prodrug formulation improved drug uptake by P-gp positive cells. (Mean ± SD, *: $p < 0.001$)

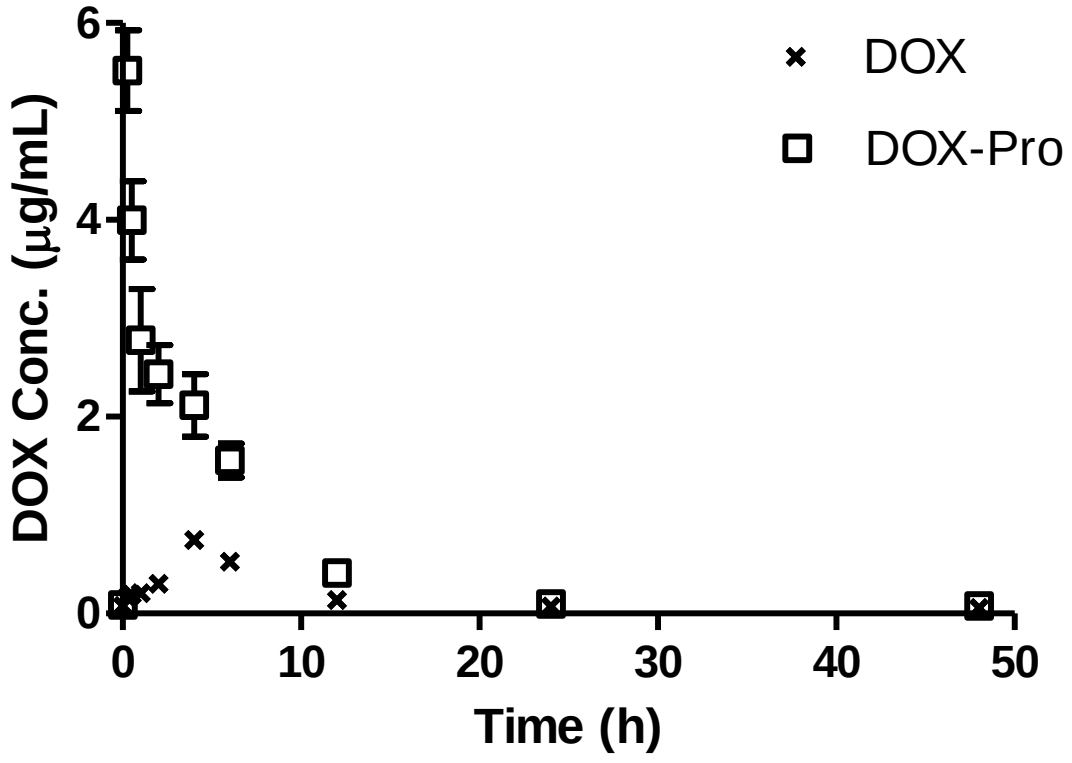

Fig. 7: Concentration-time profiles of DOX in rat serum after oral administration (mean ± SEM, n = 2).

Table 1: Pharmacokinetic parameters of DOX and DOX-Pro in rats (Mean ± SD, n = 2) (* $p < 0.05$, ** $p < 0.01$).

Parameters	Unit	DOX	DOX-Pro
C_{max}	$\mu g \cdot mL^{-1}$	0.748 ± 0.0767	5.516 ± 0.410**
$t_{1/2}$ (Serum)	h	13.412 ± 1.306	7.817 ± 0.318
AUC (Serum)	$\mu g \cdot h \cdot mL^{-1}$	8.732 ± 0.154	26.342 ± 2.438*
F_e	%	2.739 ± 0.283	4.488 ± 0.287*
Cl	$mL \cdot h^{-1} \cdot kg^{-1}$	340.735 ± 18.431	118.687 ± 8.157**
Cl_{renal}	$mL \cdot h^{-1} \cdot kg^{-1}$	9.856 ± 1.663	5.397 ± 0.013
Cl_{NR}	$mL \cdot h^{-1} \cdot kg^{-1}$	347.191 ± 22.191	115.383 ± 8.011*
Vz/F	mL	6628.05 ± 998.48	1342.22 ± 146.52*
MRT	h	20.487 ± 2.230	9.452 ± 0.329*

5.3.5 Pharmacokinetics in Rat Urine

Following orally administration of DOX or DOX-Pro, the rate elimination plots, total amount excreted urine plots and the amount remaining to be excreted (ARE) plots are shown in Fig. 8. The fraction excreted unchanged of DOX from DOX-Pro formulation (4.49 ± 0.29 %) was increased by 1.64-fold than the naked drug. In addition, there was no significant difference was observed between Cl_{renal}. However, the Cl_{NR} was reduced by 3-fold. The total amount excreted plot indicates that DOX was excreted in a higher amount in prodrug form compared to the free DOX.

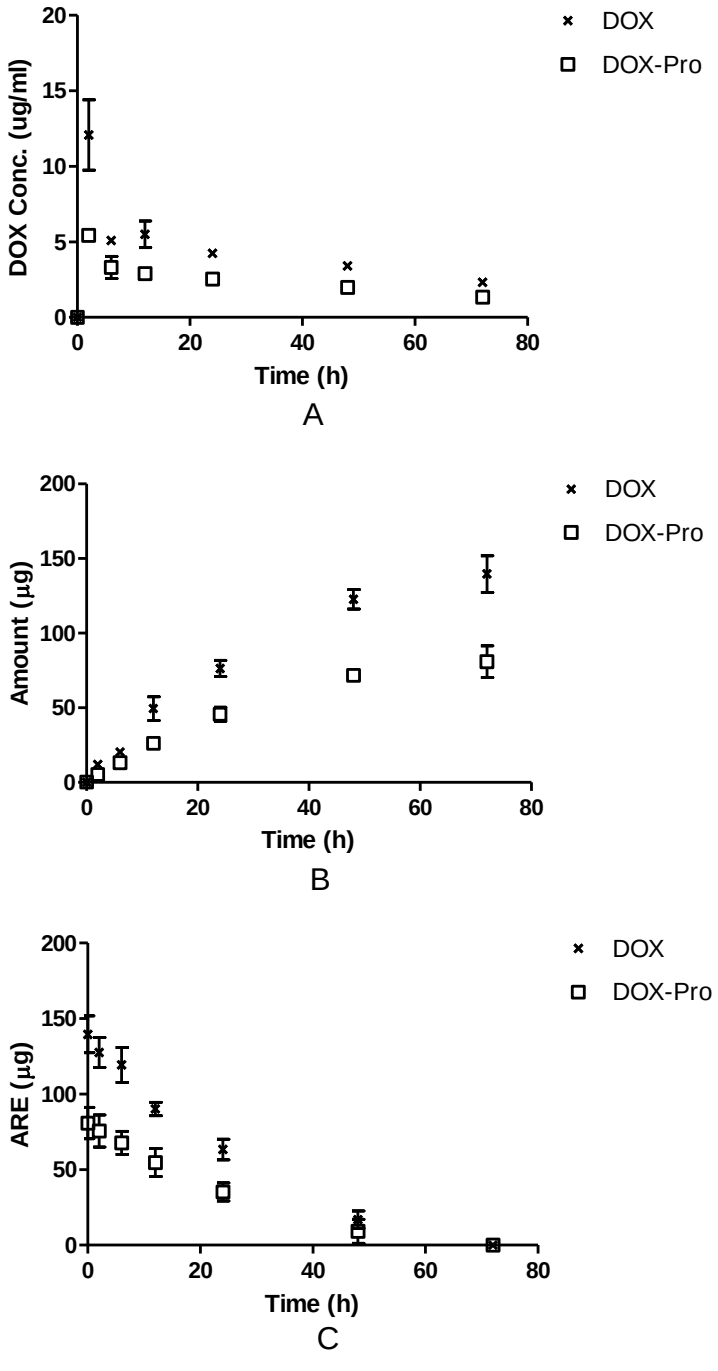

Fig. 8: (A) Urinary rate plot; (B) Total amount excreted in urine plot; (C) amount remaining to be excreted in urine (ARE) of rats after oral administration of DOX or DOX-Pro at a dose of 10 mg/kg (Mean ± SD, n = 2).

5.4 Discussion and Conclusion

The first-pass effect, or first-pass metabolism, is when orally administrated drugs are degraded or altered by gastrointestinal and hepatic enzymes, resulting in greatly reduced active drug form reaching the general systemic circulation. Bioavailability is defined as the fraction of orally administered drug absorbed unchanged into the systemic circulation. The oral bioavailability of a drug could be significantly reduced by induction of the first-pass effect.

P-gp, also known as muti-drug resistance protein 1, is a glycoprotein that is extensively distributed and expressed in the intestinal epithelium (20). It is a member of the ATP-binding cassette transporter superfamily. This transmembrane protein is an ATP-dependent efflux pump with broad substrate specificity. The P-gp transporter consists of two domains, the transmembrane domain and the nucleotide binding domain. The transmembrane domain recognizes a wide variety of substrates and undergoes a conformational change to pump out the substrate. The nucleotide binding domain is the site for ATP binding and hydrolysis. The expression of P-gp in intestinal compartments can reduce body absorption of drugs that are the substrates of P-gp, such as DOX. Therefore, drug oral bioavailability is reduced and no therapeutic plasma concentration of the drug can be achieved.

Qian et al. showed that quercetin was tightly bound to the nucleotide binding domain of P-gp and directly inhibited its ATPase activity. Homology modeling of the nucleotide binding site was modeled, and then the quercetin was docked into the modeled structure. They demonstrated that the ATP binding sites were spatial coordinates overlapped with quercetin and that the quercetin was competing for

binding. There are 14 putative hydrogen bonds observed between the quercetin and the binding site (21).

Another factor that contributes to low oral bioavailability of free DOX is that DOX is also a substrate of CYP3A4 enzyme (22). CYP3A4 is a member of the cytochrome P450 family and involves in the oxidation of the largest range of substrates of all the CYPs. It is present in the largest quantity of all the CYPs in the liver. There is an estimate that half of the drugs on the market can be metabolized by CYP3A4. Quercetin is not only an inhibitor of P-gp, but also a substrate of CYP3A4. Choi et al. showed that the combination of quercetin with doxorubicin significantly improved oral bioavailability of doxorubicin in rats (16). The activity of both P-gp and CYP3A4 were dramatically suppressed by quercetin.

There is a clinical evidence that antioxidant may alter the effectivity of the chemotherapy treatment (23, 24). On the one hand, some studies showed that taking antioxidants during chemotherapy can be helpful (25). This is because most cytotoxic chemotherapy drugs generate reactive oxygen species (ROS) and cause high levels of oxidative stress in the tumor and normal tissues. Clinical studies showed that the most dangerous side effect of DOX HCl solution is heart damage in patients (26). The free radicals generated by DOX are the key factor contributing to its severe cardiotoxic side effect (27). The scavengers of those free radicals can inhibit DOX induced cardiomyocyte apoptosis and minimize systemic toxicities (28). On the other hand, some suggest that using anti-oxidants should be avoided when a patient is under cancer chemotherapy. Studies showed that antioxidants, such as quercetin, may protect cancer cells from apoptosis and enhance cell viability (29). Since both anti-cancer activity and protection effect were reported, the working

mechanism of quercetin may be cell line specific. Thus, cancer patients should be carefully considered for traditional phytotherapy during cancer treatment.

In this study, quercetin was chemically conjugated to DOX. The DOX was released from the prodrug by peptidase cleavage, and the quercetin was released by hydrolysis reaction. Before the prodrug converted into the free DOX and quercetin, the bulky structure might further reduce the binding affinity of DOX to the transmembrane domain of P-gp compared to the free DOX. In addition, quercetin was conjugated with a linker that could provide enough free space. The binding of quercetin to P-gp at the nucleotide binding domain, which is inside the cytoplasm, may not be hindered. In addition, the prodrug may change the pharmacokinetics and drug disposition of both DOX and quercetin. The protecting effect of quercetin in certain types of cancer may be altered.

In rat pharmacokinetics study, the DOX-Pro formulation significantly improved serum $t_{1/2}$, AUC, and F_e. Following oral administration of the prodrug, the non-renal clearance was significantly decreased. It can be explained by the quercetin protection mechanism against the enzymes in the liver. Moreover, the total body clearance was significantly faster in the DOX-Pro administrated rats than that of the free DOX. It indicates that the drug accumulation in the body can be reduced by the prodrug formulation, and the DOX-Pro may further lower non-specific toxicity caused by DOX in the body. Therefore, the prodrug formulation may serve as a novel form of DOX for oral administration with improved bioavailability and altered tolerability.

5.5 References

1. M.A. Salah-Eldin, H.A. Wahba, and A.A. Halim. Biweekly peglated liposomal doxorubicin/oxaliplatin for ovarian cancer resistant to taxane-platinum treatment: a Phase II study. Indian journal of cancer. 49:169-175 (2012).
2. Y. Iwamotoand K. Tanaka. The activity of the Bone and Soft Tissue Tumor Study Group of the Japan Clinical Oncology Group. Japanese journal of clinical oncology. 42:467-470 (2012).
3. M. Spina, M. Balzarotti, L. Uziel, A.J. Ferreri, L. Fratino, M. Magagnoli, R. Talamini, A. Giacalone, E. Ravaioli, E. Chimienti, M. Berretta, A. Lleshi, A. Santoro, and U. Tirelli. Modulated chemotherapy according to modified comprehensive geriatric assessment in 100 consecutive elderly patients with diffuse large B-cell lymphoma. The oncologist. 17:838-846 (2012).
4. M. Fassnacht, M. Terzolo, B. Allolio, E. Baudin, H. Haak, A. Berruti, S. Welin, C. Schade-Brittinger, A. Lacroix, B. Jarzab, H. Sorbye, D.J. Torpy, V. Stepan, D.E. Schteingart, W. Arlt, M. Kroiss, S. Leboulleux, P. Sperone, A. Sundin, I. Hermsen, S. Hahner, H.S. Willenberg, A. Tabarin, M. Quinkler, C. de la Fouchardiere, M. Schlumberger, F. Mantero, D. Weismann, F. Beuschlein, H. Gelderblom, H. Wilmink, M. Sender, M. Edgerly, W. Kenn, T. Fojo, H.H. Muller, B. Skogseid, and F.-A.S. Group. Combination chemotherapy in advanced adrenocortical carcinoma. The New England journal of medicine. 366:2189-2197 (2012).
5. J.D. Conroyand N.J. Sharp. Bibliography of comparative and veterinary dermatology. Part 7. International journal of dermatology. 16:601-604 (1977).
6. W.J. Pigram, W. Fuller, and L.D. Hamilton. Stereochemistry of intercalation: interaction of daunomycin with DNA. Nature: New biology. 235:17-19 (1972).

7. C. Spagnuolo, M. Russo, S. Bilotto, I. Tedesco, B. Laratta, and G.L. Russo. Dietary polyphenols in cancer prevention: the example of the flavonoid quercetin in leukemia. Annals of the New York Academy of Sciences. 1259:95-103 (2012).

8. S. Chirumbolo. The role of quercetin, flavonols and flavones in modulating inflammatory cell function. Inflammation & allergy drug targets. 9:263-285 (2010).

9. H. Youn, J.C. Jeong, Y.S. Jeong, E.J. Kim, and S.J. Um. Quercetin potentiates apoptosis by inhibiting nuclear factor-kappaB signaling in H460 lung cancer cells. Biological & pharmaceutical bulletin. 36:944-951 (2013).

10. C. Huang, S.Y. Lee, C.L. Lin, T.H. Tu, L.H. Chen, Y.J. Chen, and H.C. Huang. Co-treatment with quercetin and 1,2,3,4,6-penta-O-galloyl-beta-D-glucose causes cell cycle arrest and apoptosis in human breast cancer MDA-MB-231 and AU565 cells. Journal of agricultural and food chemistry. 61:6430-6445 (2013).

11. G. Wang, L. Song, H. Wang, and N. Xing. Quercetin synergizes with 2-methoxyestradiol inhibiting cell growth and inducing apoptosis in human prostate cancer cells. Oncology reports. 30:357-363 (2013).

12. A.A. Gokbulut, E. Apohan, and Y. Baran. Resveratrol and quercetin-induced apoptosis of human 232B4 chronic lymphocytic leukemia cells by activation of caspase-3 and cell cycle arrest. Hematology. 18:144-150 (2013).

13. G. Wang, J. Wang, J. Luo, L. Wang, X. Chen, L. Zhang, and S. Jiang. PEG2000-DPSE-coated quercetin nanoparticles remarkably enhanced anticancer effects through induced programed cell death on C6 glioma cells. J Biomed Mater Res A. 101:3076-3085 (2013).

14. S.Z. Li, K. Li, J.H. Zhang, and Z. Dong. The effect of quercetin on doxorubicin cytotoxicity in human breast cancer cells. Anti-cancer agents in medicinal chemistry. 13:352-355 (2013).

15. G. Wang, J. Zhang, L. Liu, S. Sharma, and Q. Dong. Quercetin potentiates doxorubicin mediated antitumor effects against liver cancer through p53/Bcl-xl. PloS one. 7:e51764 (2012).

16. J.S. Choi, Y.J. Piao, and K.W. Kang. Effects of quercetin on the bioavailability of doxorubicin in rats: role of CYP3A4 and P-gp inhibition by quercetin. Archives of pharmacal research. 34:607-613 (2011).

17. I.L. Chen, Y.J. Tsai, C.M. Huang, and T.H. Tsai. Lymphatic absorption of quercetin and rutin in rat and their pharmacokinetics in systemic plasma. Journal of agricultural and food chemistry. 58:546-551 (2010).

18. J.S. Choi, B.W. Jo, and Y.C. Kim. Enhanced paclitaxel bioavailability after oral administration of paclitaxel or prodrug to rats pretreated with quercetin. Eur J Pharm Biopharm. 57:313-318 (2004).

19. M.K. Kim, K.S. Park, W.S. Yeo, H. Choo, and Y. Chong. In vitro solubility, stability and permeability of novel quercetin-amino acid conjugates. Bioorganic & medicinal chemistry. 17:1164-1171 (2009).

20. L.M. Chan, S. Lowes, and B.H. Hirst. The ABCs of drug transport in intestine and liver: efflux proteins limiting drug absorption and bioavailability. European journal of pharmaceutical sciences : official journal of the European Federation for Pharmaceutical Sciences. 21:25-51 (2004).

21. F. Qian, D. Wei, J. Liu, and S. Yang. Molecular model and ATPase activity of carboxyl-terminal nucleotide binding domain from human P-glycoprotein. Biochemistry Biokhimiia. 71 Suppl 1:S18-24, 11-12 (2006).

22. J.E. Kim, H.J. Cho, J.S. Kim, C.K. Shim, S.J. Chung, M.H. Oak, I.S. Yoon, and D.D. Kim. The limited intestinal absorption via paracellular pathway is responsible for the low oral bioavailability of doxorubicin. Xenobiotica; the fate of foreign compounds in biological systems. 43:579-591 (2013).

23. K.N. Prasad. Multiple dietary antioxidants enhance the efficacy of standard and experimental cancer therapies and decrease their toxicity. Integrative cancer therapies. 3:310-322 (2004).

24. G.M. D'Andrea. Use of antioxidants during chemotherapy and radiotherapy should be avoided. CA: a cancer journal for clinicians. 55:319-321 (2005).

25. R.I. Salganik. The benefits and hazards of antioxidants: controlling apoptosis and other protective mechanisms in cancer patients and the human population. Journal of the American College of Nutrition. 20:464S-472S; discussion 473S-475S (2001).

26. G. Minotti, P. Menna, E. Salvatorelli, G. Cairo, and L. Gianni. Anthracyclines: molecular advances and pharmacologic developments in antitumor activity and cardiotoxicity. Pharmacological reviews. 56:185-229 (2004).

27. P. Venditti, M. Balestrieri, T. De Leo, and S. Di Meo. Free radical involvement in doxorubicin-induced electrophysiological alterations in rat papillary muscle fibres. Cardiovascular research. 38:695-702 (1998).

28. P. Spallarossa, S. Garibaldi, P. Altieri, P. Fabbi, V. Manca, S. Nasti, P. Rossettin, G. Ghigliotti, A. Ballestrero, F. Patrone, A. Barsotti, and C. Brunelli. Carvedilol

prevents doxorubicin-induced free radical release and apoptosis in cardiomyocytes in vitro. Journal of molecular and cellular cardiology. 37:837-846 (2004).

29. Z. Akanand A.I. Garip. Antioxidants May Protect Cancer Cells from Apoptosis Signals and Enhance Cell Viability. Asian Pacific journal of cancer prevention : APJCP. 14:4611-4614 (2013).

Chapter 6

Development of a HPLC Method for Separation of Highly Active Compounds from Degraded Alternol

6.1 Introduction

Naturally occurring compounds, such as herbal extracts and fermentation products, could serve as complimentary medications to improve treatment in many cancer patients with minimal side effects (1, 2). Paclitaxel, a mitotic inhibitor used in anticancer chemotherapy, was isolated from the bark of the Pacific yew tree, *Taxus brevifolia,* in 1971 (3). Harvesting the drug from the tree bark required killing the tree, which had uncertain population, slow growth and unknown future demand. Therefore, an alternative and sustainable source was preferred.

A fermentation technology was developed to produce paclitaxel, using a specific Taxus plant cell line in aqueous medium with *Penicillum raistrickii*, an endophytic fungus. This fermentation technology also eliminated the use of hazardous chemicals needed in the total synthesis and semi-synthesis of the molecule. In response to the success of the *Taxus brevifolia* bark extract, researchers are still looking for unique anti-cancer agents from the yew tree.

Alternol (Fig. 1A) is a novel fermentation compound from a microorganism called *Alternaria alternate* var. *monosporus*, which was isolated from the bark of the yew tree. Alternol showed anti-proliferating effects and induced apoptosis in mouse leukemia cells (4), human gastric carcinoma cells (5) and prostate cancer cells (6). The expression level of caspase-3, an apoptosis-related cysteine peptidase, was found up-regulated after alternol treatment (7). In addition, alternol showed selective anti-cancer effects through modulations of the AMP-activated protein kinase signaling pathway (6).

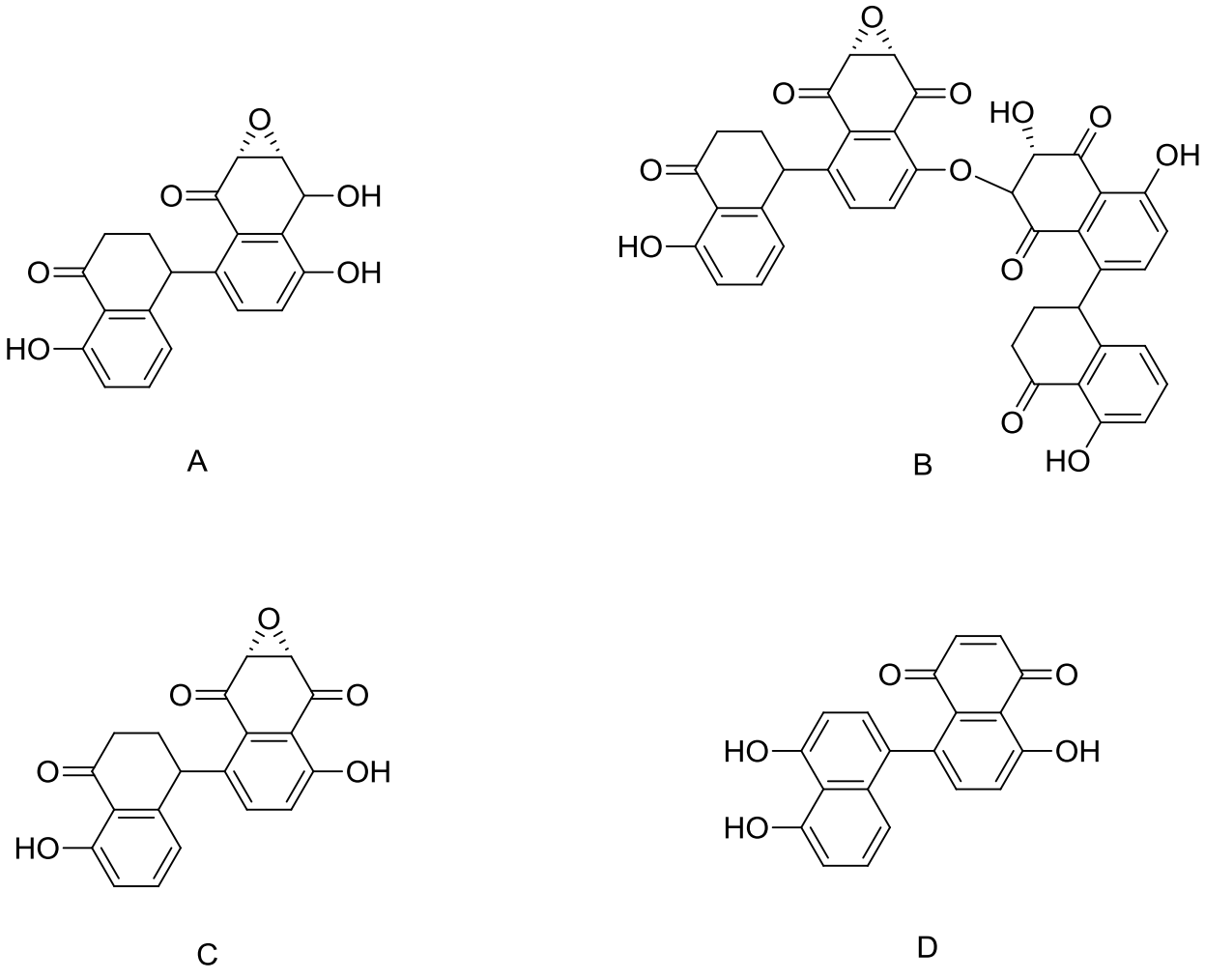

Fig.1: (A) Structure of alternol; (B) degradation compound #1 (MW: 700); (C) degradation compound #2 (MW: 350); (D) degradation compound #3 (MW: 332).

The preparation of alternol from a fermentation process was reported in the patent, application US No. 2009/0203775 A1. The cultured microorganism medium was extracted with organic solvent twice. The compound from second extraction was purified by a chromatography process. To crystalize the product, the desired compound was dissolved in ethyl acetate and precipitated in cold petroleum ether.

The purified alternol from a provider showed multiple peaks on HPLC alluding to degradation of the alternol. In this study, a HPLC method was developed to separate the active compound(s) from the mixture.

6.2 Materials and Methods

6.2.1 Materials

Alternol was obtained from Strand Biotech Co. Ltd. (Shantou, China). All the solvents, of the highest grade, were purchased from Fisher Scientific (Lenexa, KS) or Sigma Aldrich (St. Louis, MO) and were used as received. Mass spectra were obtained by electrospray ionization mass spectrometry (ESI-MS).

6.2.2 HPLC Method Development

A Shimadzu LC-2010CHT system (Shimadzu Scientific Instruments, Columbia, MD) with a reversed phase column and UV detection at 260 nm was used.

6.2.2.1 The effects of different organic phases gradients, flow rates and column temperatures

The mobile phases were A of 100 % ddH_2O and B of 100 % MeOH. The reverse phase column, TSK-GEL® ODS-100Z (Tosho Bioscience LLC, King of Prussia, CA) was used. The gradient was i) 5 min with 10 % solvent B; ii) a liner gradient from 10 % to 85 % or 75 % solvent B over 5 min; iii) 10 min with 85 % or

75 % solvent B; iv) 10 min with 10 % solvent B. The chromatograms are shown in Fig. 1. The column temperatures were set at 35 °C.

The difference between acetonitrile (ACN) and MeOH was studied. The mobile phases were A of 100 % ddH_2O and B of 100 % ACN. The gradient was i) 5 min with 10 % solvent B; ii) a liner gradient from 10 % to 65 % solvent B over 5 min; iii) 10 min with 65 % solvent B; iv) 10 min with 10 % solvent B. The chromatograms are shown in Fig. 2. The column temperature was set at 35 or 50 °C. The flow rates were 0.6 mL/min.

6.2.2.2 The effects of column factors

The mobile phases were A of 100 % ddH_2O and B of 100 % MeOH. The gradient was i) 5 min with 10 % solvent B; ii) a liner gradient from 10 % to 50 % solvent B over 5 min; iii) 10 min with 50 % solvent B; iv) 10 min with 10 % solvent B. Three additional columns were used: Jupiter® 5 µm C5 300A 150 × 4.6 mm (Phenomenex, Torrance, CA); Phenyl Hypersil NCI 2404 (Fisher Scientific, Lenexa, KS); Thermo Scientific Hyoersil CPS-2 (Cyano) (Fisher Scientific, Lenexa, KS).

6.2.2.3 The effects of acidic mobile phase modifier

The mobile phases were A of 0.1 % (v/v) formic acid in ddH_2O and B of 0.1 % (v/v) formic acid in MeOH. The C18 reverse phase column was a TSK-Gel® ODS-100Z. The gradient was i) 5 min with 10 % solvent B; ii) a liner gradient from 10 % to 75 % or 65 % solvent B over 5 min; iii) 10 min with 75 % or 65 % solvent B; iv) 10 min with 10 % solvent B. The chromatograms were shown in Fig. 4. The column temperature was set at 50 °C. The flow rate was 0.5 mL/min.

6.2.2.4 The effects of basic mobile phase modifier

The mobile phase were A of 0.1 % (v/v) TEA and B of 0.1 % (v/v) TEA in MeOH. The gradient was i) a liner gradient from 10 % to 90 % over 20 min; ii) 1 min with 90 % solvent B; iii) 10 min with 10 % solvent B. The flow rate was 0.6 mL/min.

6.2.3 Selectivity and Resolution

Selectivity of the two peaks was calculated as following:

$$\alpha = (t_{R2}-t_0)/(t_{R1}-t_0) \quad (1)$$

The fundamental resolution equation was calculated as:

$$R_s = (t_{R2}-t_{R1})/((0.5\times(w_1+w_2)) \quad (2)$$

where t_{R1} and t_{R2} are the retention times of two adjacent peaks and w_1 and w_2 are their corresponding baseline peak widths.

Rs also can be calculated using widths at half of the peak height with following equation:

$$Rs = (t_{R2} - t_{R1})/((1.7 \times 0.5 \times (w_{0.5,1} + w_{0.5,2})) \quad (3)$$

6.2.4 Cytotoxicity

Prostate cancer cell line, PC3, was used to test the cytotoxicities of the three degraded compounds. Cells were plated in 96-well plate overnight. Then, the cells were treated with the purified active components for additional 48 h. The proliferation rates of the cells were analyzed by MTT assay using the Cell Proliferation kit I (Roche Molecular Biochemicals, Indianapolis, IN).

6.3 Results

6.3.1 The effects of organic solvent contents, flow rates and column temperatures.

Alternol was separated by a C18 TSK-GEL® ODS-100Z column using MeOH and ddH_2O as the mobile phases with different conditions as shown in Fig. 2. Even though lowering the organic phase gradient and reducing mobile phase flow rate gave better separation, complete separation could not be achieved by using such optimization.

Acetonitrile (ACN) generated a shorter retention time compared to MeOH (Fig. 3). With the same gradient, the retention time was around 16 min using MeOH as the organic phase with a flow rate of 0.8 mL/min (Fig. 2B), which was approximately the same as using ACN with a flow rate of 0.6 mL/min (Fig. 3A). This is consistent with ACN's higher elution strength compared to MeOH.

By increasing the column temperature from 35 °C to 50 °C, the retention time was shorted by approximately 2 min. However, there was no significant difference on separation ability.

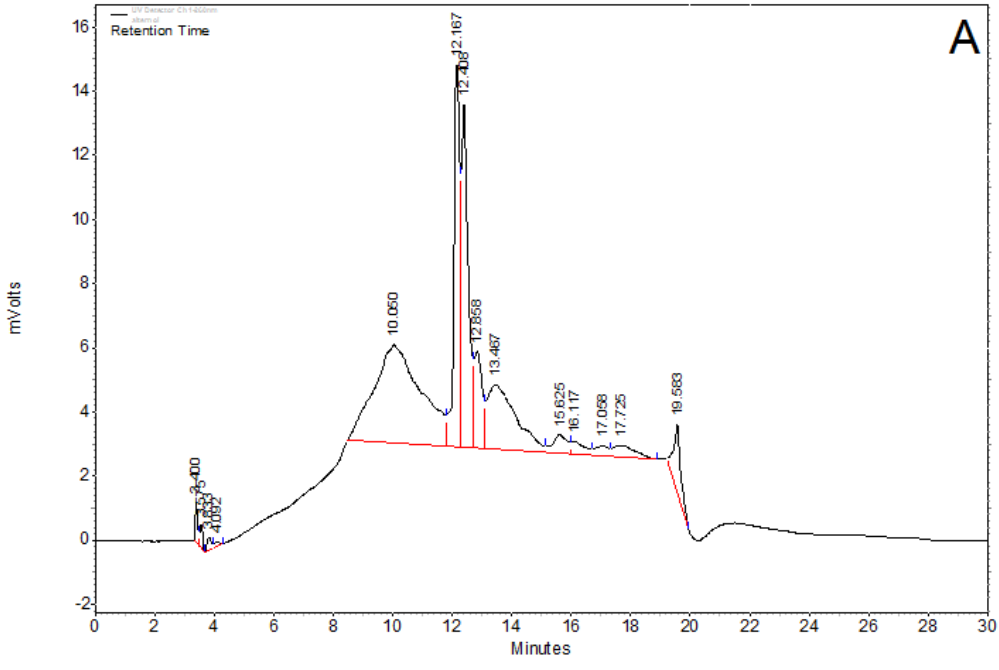
A
Retention Time
mVolts
Minutes
10.050
12.167
12.408
12.858
13.467
15.625
16.117
17.058
17.725
19.583

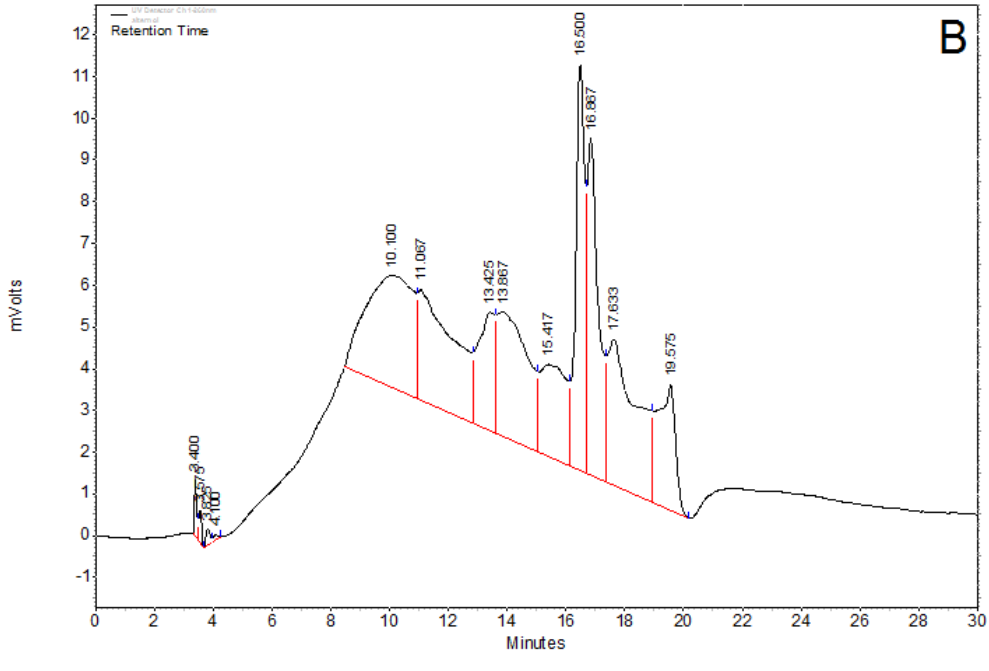
B
Retention Time
mVolts
Minutes
10.100
11.067
13.425
13.867
15.417
16.500
16.867
17.633
19.575

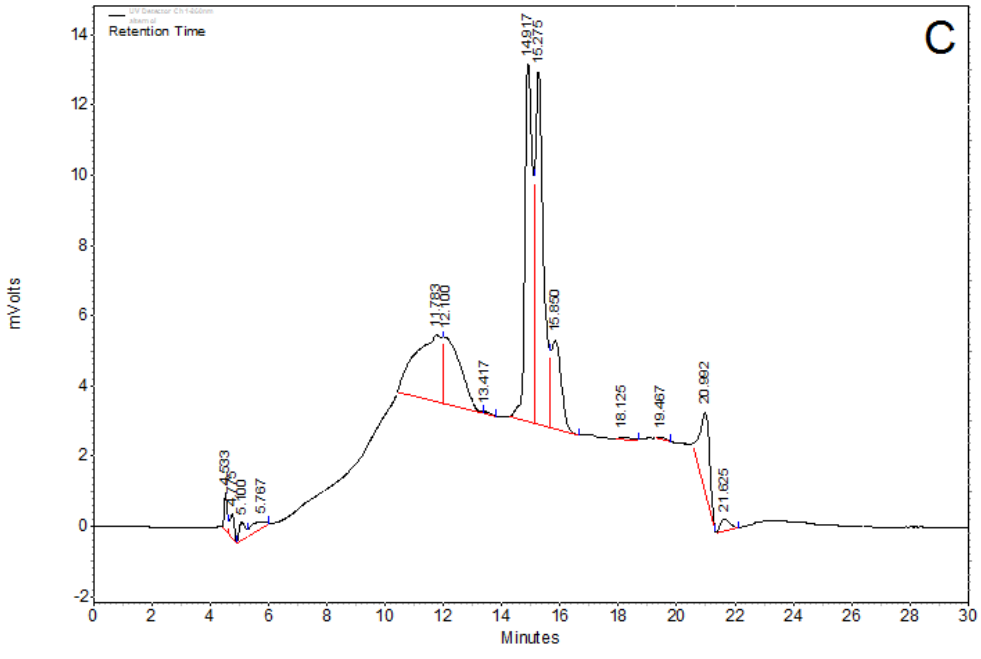

Fig. 2: (A) Alternol separation using ddH_2O/MeOH as the mobile phase. Chromatogram condition: flow rate 0.8 mL/min; gradient MeOH 85 % at plateau. (B) Alternol separation using ddH_2O/MeOH as the mobile phase. Chromatogram condition: flow rate 0.8 mL/min; gradient MeOH 75 % at plateau. (C) Alternol separation using ddH_2O/MeOH as the mobile phase. Chromatogram condition: flow rate 0.6 mL/min; gradient MeOH 85 % at plateau.

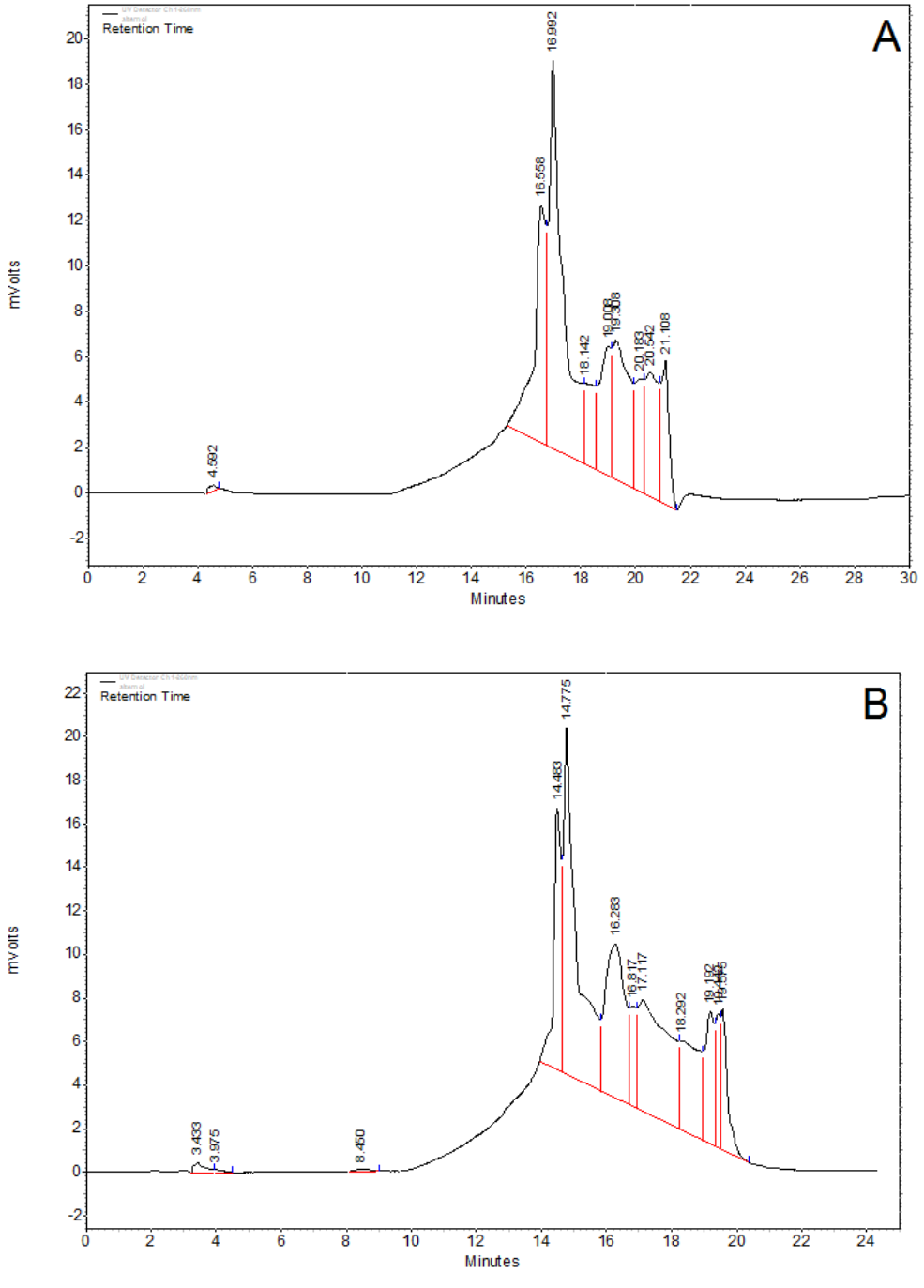

Fig. 3: (A) Alternol separation using ddH_2O/ACN as the mobile phase. Column temperature: 35 °C; (B) Alternol separation using ddH_2O/ACN as the mobile phase. Column temperature: 50 °C.

6.3.2 The effects of column factors

Different columns were used for compound separation. The retention time of the main peak using a Jupiter® 5 µm C5 300A 150 × 4.6 mm and Phenyl Hypersil NCI 2404 column were 10.108 and 14.992 min, respectively (Fig. 4). There was no separation of the three compounds and a tailing peak was observed. The peak was wider when using a phenol column compared to the C5 column. The retention time of using Hyoersil CPS-2 (Cyano) column was 9.125 min with an asymmetric peak shape (Fig. 4C).

6.3.3 The effects of acidic modifier

The major peaks had better separation when 0.1 % TFA was added to the mobile phases (Fig. 5). With a lower gradient, a longer retention time was observed and the peaks were further isolated. However, there still was not complete separation using this strategy.

6.3.4 The effects of basic modifier

The separation chromatograms of the compound mixture using ddH_2O and MeOH with 0.1 % TEA as the mobile phases are shown in Fig. 6. The three compounds were completely separated. Each peak was then re-injected into the HPLC. After re-injection, the first peak showed only one peak (Fig. 6B). The second peak generated three peaks again (Fig. 6C). The third peak gave two peaks, the first peak and the third peak (Fig. 6D).

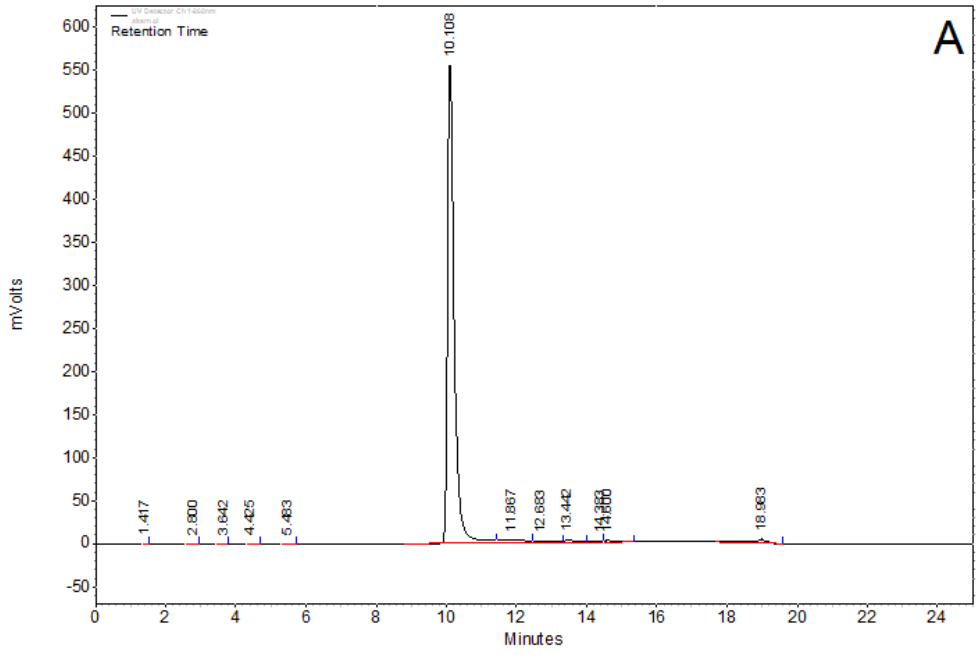
A
Retention Time
mVolts
Minutes
10.108
1.417
2.800
3.642
4.425
5.483
11.867
12.683
13.442
18.963

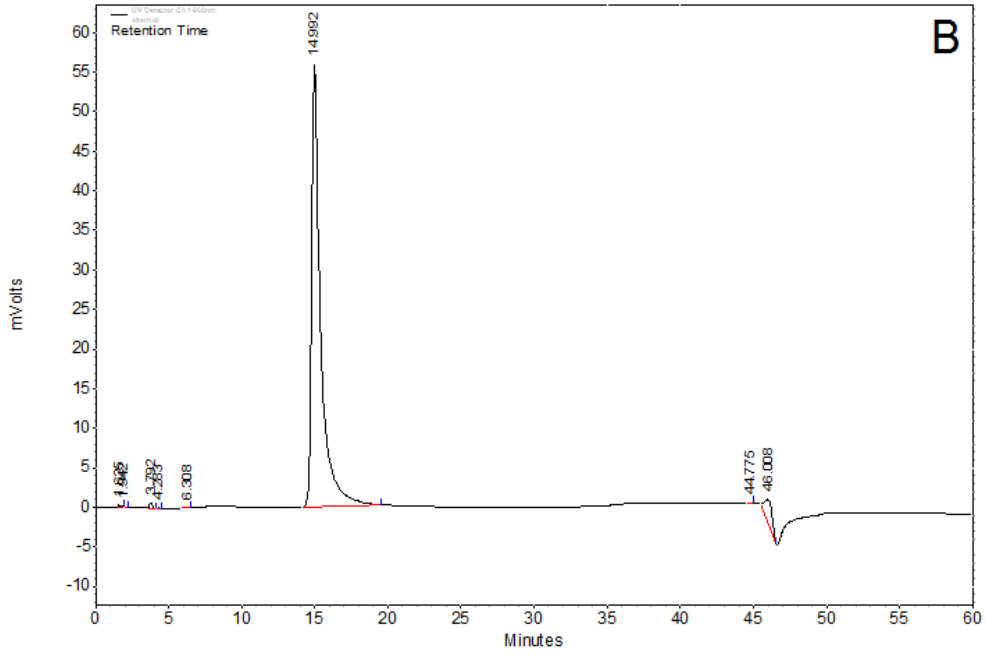
B
Retention Time
mVolts
Minutes
14.992
6.308
44.775
46.008

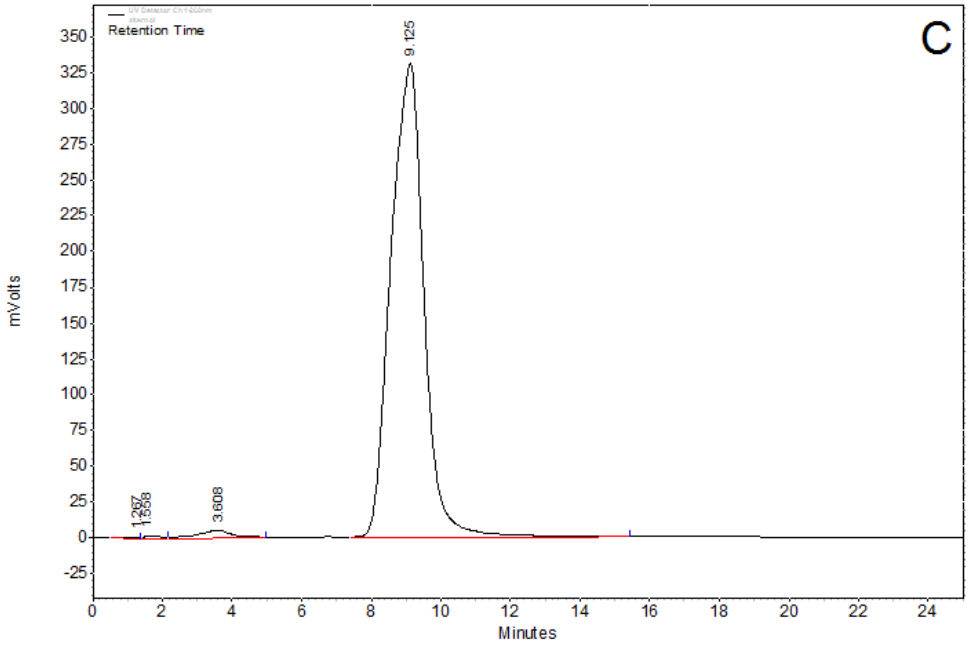

Fig. 4: (A) Alternol separation using a Jupiter® 5 µm C5 300A 150 × 4.6 mm column. Flow rate was 0.6 mL/min. (B) Alternol separation using Phenyl Hypersil NCI 2404 column. Flow rate was 0.5 mL/min. (C) Alternol separation using Thermo Scientific Hyoersil CPS-2 (Cyano) column. Flow rate was 0.2 mL/min.

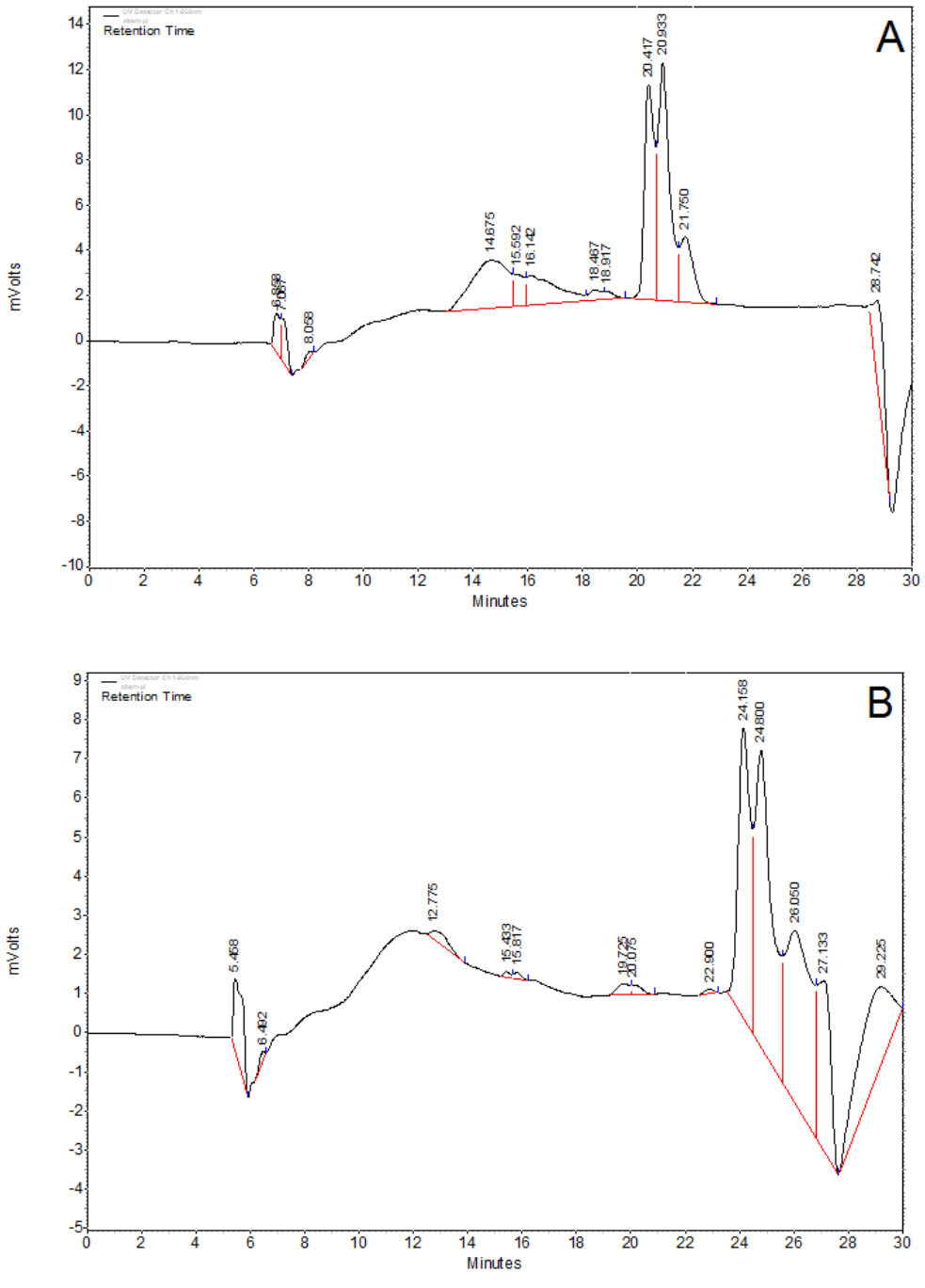

Fig. 5: (A) Alternol separation using ddH_2O/MeOH with 0.1 % TFA as the mobile phase. MeOH was 85 % at plateau; (B) Alternol separation using ddH_2O/MeOH with 0.1 % TFA as the mobile phase. MeOH was 75 % at plateau.

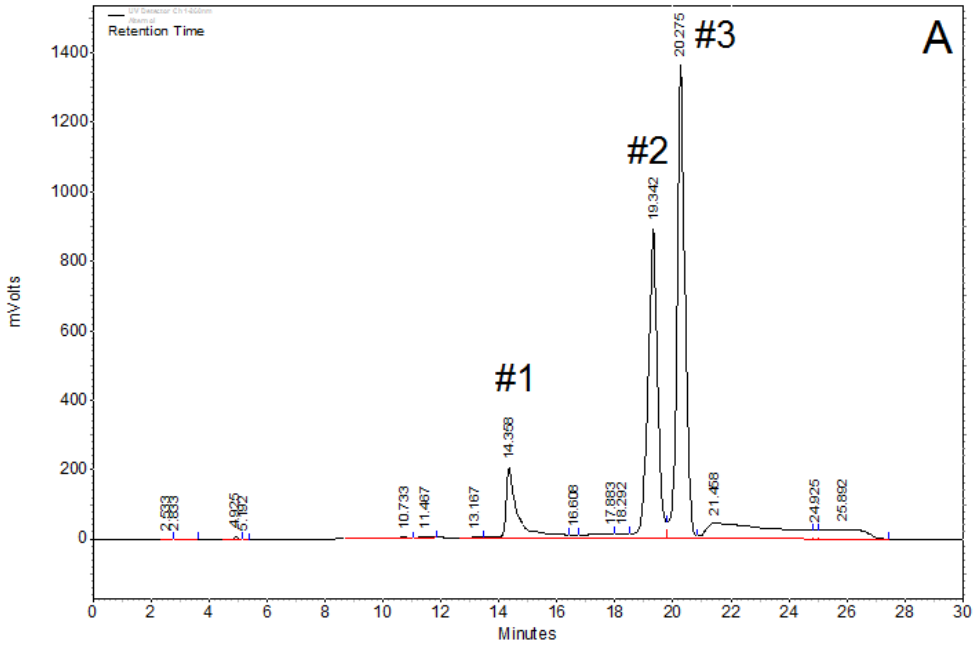
A
Retention Time
#1
#2
#3
14.358
19.342
20.275
mVolts
Minutes

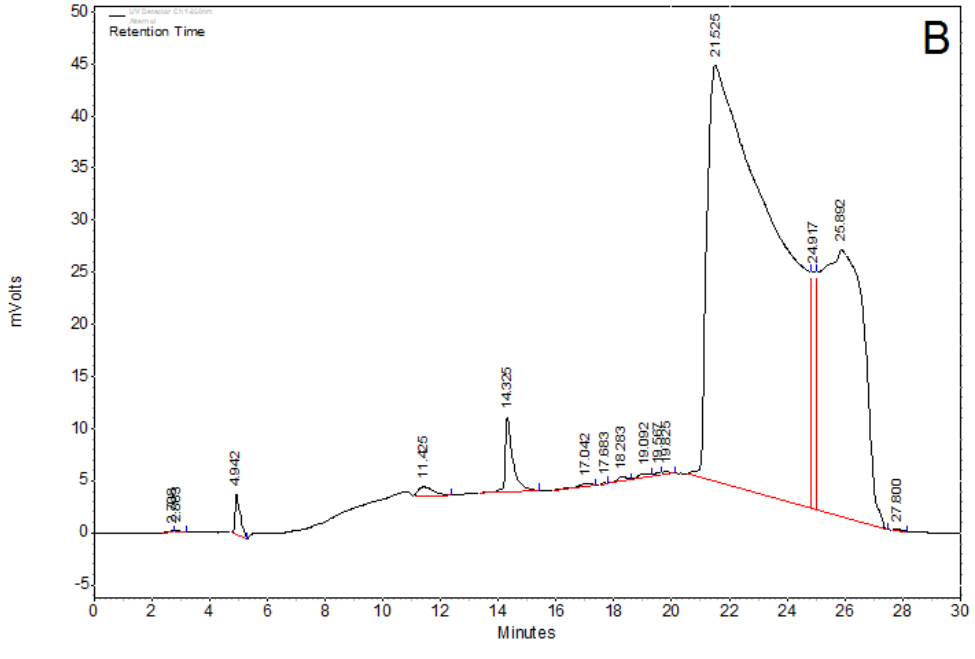
B
Retention Time
21.525
24.917
25.892
14.325
11.425
4.942
27.800
mVolts
Minutes

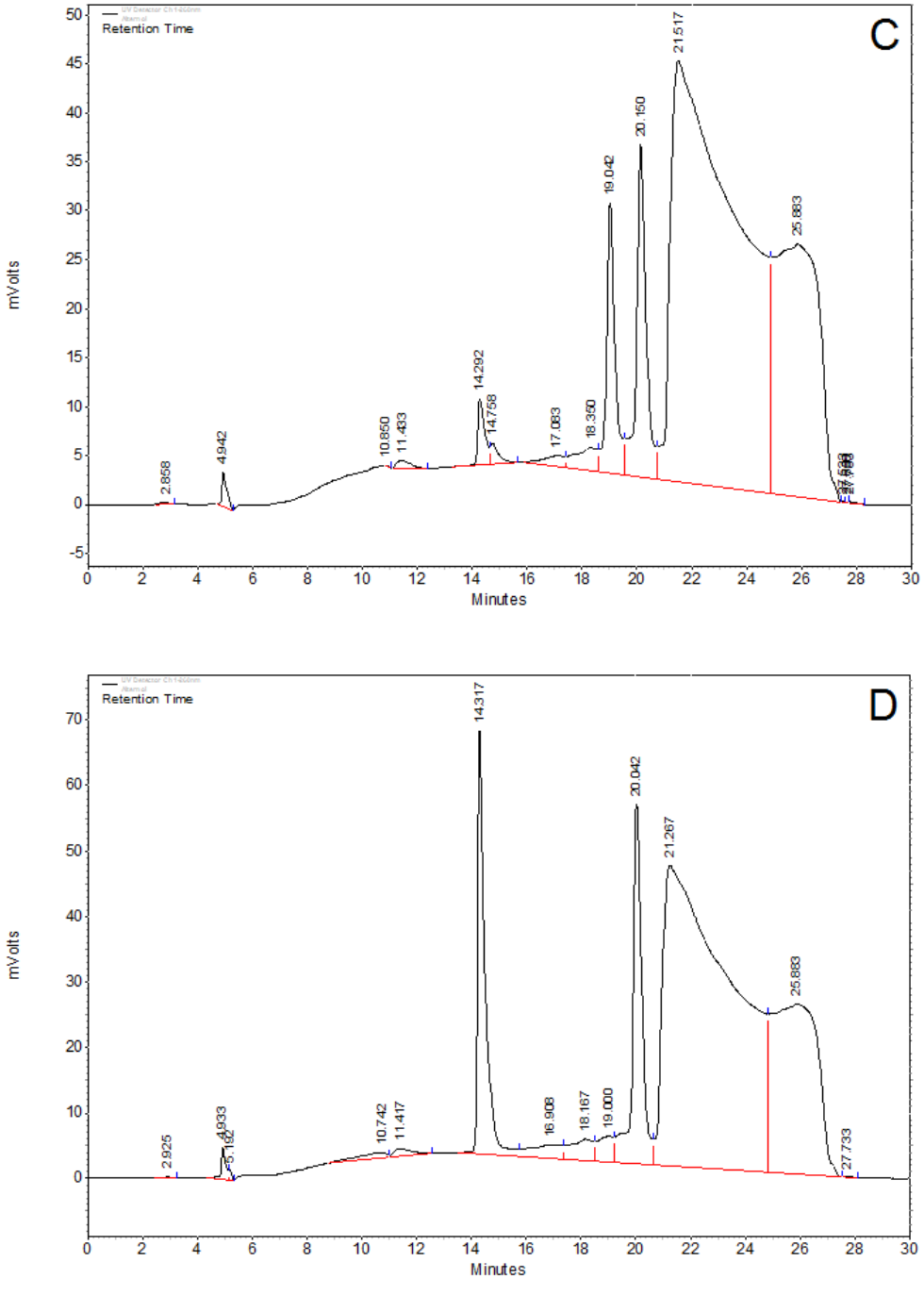

Fig. 6: (A) Alternol separation using 0.1 % TEA as the mobile phase modifier; (B) Peak #1 re-injection; (C) Peak #2 re-injection; (D) Peak #3 re-injection.

6.3.5 Selectivity and Resolution

The selectivity and resolution of the two major peaks of the compound mixture by different separation methods were calculated as shown in Table 1. Both α and Rs were improved by a basic mobile phase modifier. No improvement was observed between acid modified mobile phase and non-modified mobile phase.

6.3.6 Cytotoxicity

The cytotoxicities of the three components were studied in PC3 prostate cancer cells. The IC50s of compound #1, #2 and #3 were 10 μM, 10 μM and 3 μM, respectively. The dimer form showed highest activity among the three degradants.

Table 1: Calculation of selectivity and resolution parameters of the two major peaks.

Mobile Phase	Flow Rate (mL/min)	Organic Solvent (%)	α	Rs
ddH_2O/MeOH	0.8	85	1.027	0.428
	0.8	75	1.028	0.645
	0.6	85	1.034	0.651
ddH_2O/MeOH w/ 0.1% Formic Acid	0.5	85	1.038	0.647
	0.5	75	1.034	0.799
ddH_2O/MeOH w/ 0.1% TEA	0.6	90	1.079	1.231

6.4 Discussion

HPLC is an important analytic tool for drug monitoring and quality assurance. It is especially important in the field of pharmaceuticals and medical industries because it allows both qualitative and quantitative analysis (8). The U.S. Food and Drug Administration has established stringent regulations for HPLC tests in these industries. In addition, the application of HPLC method enables complex mixtures, such as herbal medicine plant extracts, to be separated into individual compounds (9).

The retention of the compound in HPLC can be controlled by the mobile phase gradient settings, flow rate and column temperature. Using a gradient with a slow increase in the non-polar mobile phase percentage gave a better separation of the molecules with similar polarity (Fig.1B). However, this led to a loss of signal intensity as the peak itself was wider. In contrast, a steep gradient improved signal intensity with a resulting loss of resolution (Fig. 1A). The mobile phase flow rate impacts HPLC system pressure, chromatographic quality and analysis time. An appropriate flow rate must be chosen for the HPLC system and the column. At a faster flow rate, the analyte may have insufficient time to interact with the stationary phase. In comparison, at a lower flow rate, it takes a longer time for the peak to appear at the detector (Fig. 1C). Column temperature is another factor that could affect the system pressure. Temperature also can increase the column efficiency. With elevated temperature, the eluent viscosity was decreased resulting in lower back pressure and also improved the diffusion coefficient giving narrower peaks (Fig. 2). The shorter retention time generated taller peaks and lowered the detection limits.

The most commonly used organic solvents as mobile phases in reverse phase chromatography are ACN and MeOH. LC grade ACN has lower absorbance, especially for shorter wavelengths (< 250 nm). LC grade ACN as the mobile phase results in less ghost peaking for gradient baselines and is best used for high sensitivity analysis at short UV wavelengths. With the same mix ratio of water, ACN generally has higher elution strength and less back pressure compared to MeOH. In addition, the separation selectivity is different between ACN and MeOH. This can be explained by that the chemical properties of the organic solvent molecules. MeOH is a protic solvent and can undergo polar-polar or ionic interactions with the solutes. ACN is an aprotic solvent and forms a binary mixture with water. The reported structure of alternol is a polyphenol molecule, and it has enhanced resonance for stabilization. The predicted pKas of the molecule are 8.3 and 10.5. At neutral pH, the molecules are pronated and positively charged. Therefore, the mixture should have a better separation with MeOH than ACN, which was observed.

HPLC separation is based on mechanisms of adsorption and partitioning, which depends on the type of stationary phase used. The stationary phase of the reverse phase column used was silica particles functionalized with straight chain alkyl groups, such as C18 and C5, or with an aromatic group, phenyl, or a cyano group. A C18 column was the most hydrophobic column used in this study. The C18 stationary phase provides weak H-bonding, no dipole-dipole interaction, no π- π interaction, no shape selectivity and moderate ionic interaction. Similar to the C18 column, the C5 column offers weak H-bonding, no dipole-dipole interaction, no π- π interaction and no shape selectivity. The C5 column also provides a strong hydrophobic interaction between the stationary phase and the solute, but it is less

hydrophobic than C18. In addition, the hydrophobic properties, the C18 reagents are bulky and can leave some silanols unreacted (ca. 50%). The C5 reagents are smaller than C18 and they have better silanol coverage. Therefore, at pH > 4, silanols on C18 column can ionize and add cation-exchange character to the column. We showed that with decreased hydrophobicity of the stationary phase, the retention of the mixture was reduced (Fig. 4A). In this case, the selectivity of a C5 column was also compromised.

Phenyl bonded stationary phase is less hydrophobic than straight chain alkyl columns. Phenyl is a Lewis base or an electron donation group. Due to the rigid nature of the aromatic ring, solute shape can dictate strong planar shape selectivity. It is a weak H-bonding acceptor with weak dipole-dipole attractions, strong donor of π- π interaction and weak ionic interaction. Since alternol has a multiple ring structure, a phenyl column was used to examine if the mixture could achieve better separation. We demonstrated that the mixture had retention on phenyl column; however, the selectivity of compounds was very low (Fig. 4B). This indicated that using π- π interaction and shape selectivity of the phenol group did not increase separation of the compounds mixture.

A cyano group has a large dipole moment that can interact with other dipole molecules in solution. Cyano groups have moderate hydrophobic character from alkyl ligands and provide a weak H-bonding acceptor, weak π- π interaction, no shape selectivity and strong ionic interaction. The degraded alternol did not have enough retention on cyano column, and furthermore, no separation of the mixture was observed. This illustrated that the dipole-dipole interaction between the

stationary phase and the solute was very weak and was not suitable for this compound purification.

In the reversed phase chromatography, the most polar molecule will be eluted first. This is due to polar compound's minimum interaction with the non-polar stationary phase. While increasing the polarity of the mobile phase, retention of highly retained molecules will increase. The retention time and selectivity of the solutes in HPLC also can be affected by pH and the type of organic modifiers. The pH of the mobile phase affects analyte ionization and solvation; therefore, interactions of the analytes with the stationary phase will be changed. The retention time of ionizable compounds at a certain pH is dependent on their ionization state. The hydrophobicity will be decreased with ionization and lead to a shorter HPLC retention times.

In HPLC method development, the most common pH adjustment method is to add acid modifiers because the stable pH range of most columns is from 2 to 8. We found that with 0.1 % TFA added in the mobile phase the peaks achieved better separation, but they still were not fully separated. This indicated that at acidic pH the polarities of the mixture compounds were not changed significantly and they may have similar chemical structures.

A basic modifier, 0.1 % TEA, was also added to the mobile phase. The pH stability of the column used in this study was from 2 to 12. We showed that the three compounds were fully separated at basic conditions. The pKa of TEA is 10.65, and the pH of 0.1 % TEA in the mobile phase was about 9.5. The improved separation is

probably because the mobile phase pH was between the 2 pKas of the molecule. The degrees of ionization were significantly different among the three compounds.

Selectivity is the retention time ratio of two adjacent peaks. It is an important parameter to determine how the compounds are separated. In general, if α equal to 1, separation efficiency will not improve with further column efficient. Based on the fundamental resolution equation, selectivity has a linear relationship with relative resolution. We showed that under similar conditions the selectivity was improved from 1.034 to 1.079, indicating a 2.32-fold improvement in relative resolution.

Unlike the selectivity, which is independent of the column efficiency, resolution evaluates compound separation based on the complete chromatographic system. In general, Rs equal to or more than 1 indicates complete separation. If Rs is less than 1, the compounds overlapped. By using basic a modifier, the resolution improved from 0.651 to 1.231, which is 1.89-fold.

The molecular weights of each peak were obtained by mass spectrometry in negative mode. The masses of the three peaks were 332.0799, 350.0922 and 700.1927, respectively. The third peak was a dimer of the second. The molecular weight of the second peak was 2 mass units off from the reported structure. After re-injection of each peak into the HPLC, we found that the first peak was the degradation product from the third peak and, the third peak was degraded from the second peak. The second peak was very close to the parent drug and there was no claimed compound found. Based on mass spec, the proposed structures of degradation compound #1, #2 and #3 are shown in Fig. 1. The proposed alternol

degradation mechanisms and formation mechanisms of compound #1, #2 and #3 are shown in Fig. 7.

Alternol can be easily oxidized when exposed to air (Fig. 7A). The degradation started from the loss of hydrogen atom of the hydroxyl group to form a radical intermediate. Then one of its α-Hs was captured by the formed radical spice resulting in the oxidized compound (compound #2) which was found at m/z 350 by ESI.

Compound #2, as soon as it was formed, was deprotonated by TEA. The formed anion then attacked the one of the carbon atom of the cyclopropane as a nucleophile producing the dimer (compound #3) which was found at m/z 700.

Compound #3 is not stable in the presence of TEA at the temperature of 40 ^{o}C. The two 8-hydroxy-3,4-dihydronaphthalen-1(2H)-one parts in the molecule were oxidized by air to form two naphthalene-1,8-diol partners in the intermediate, which was then hydrolyzed resulting in two molecules of compound #1 which appeared m/z 332 by ESI.

Fig. 7A

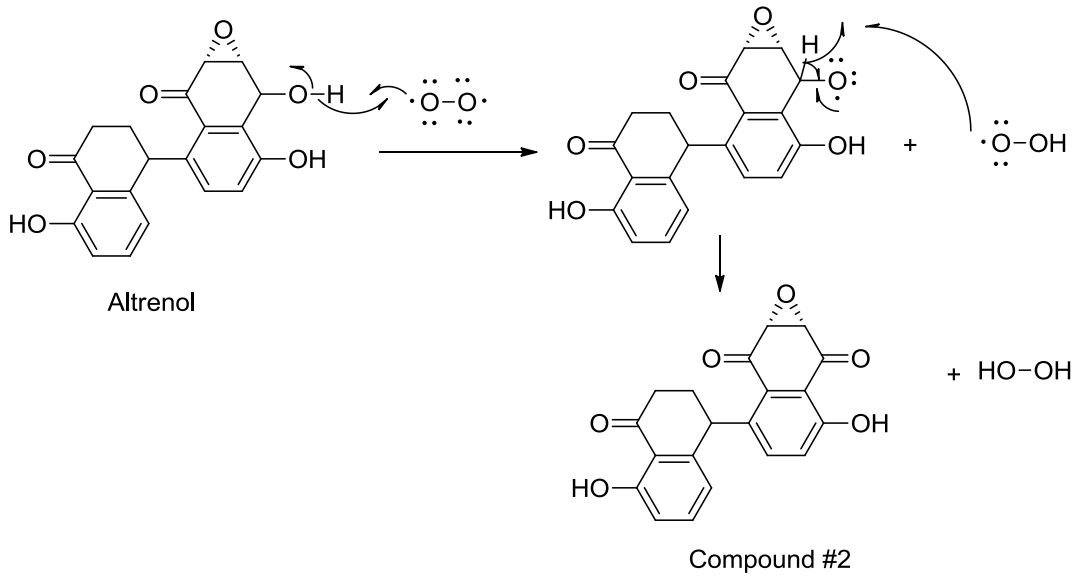

Fig. 7B

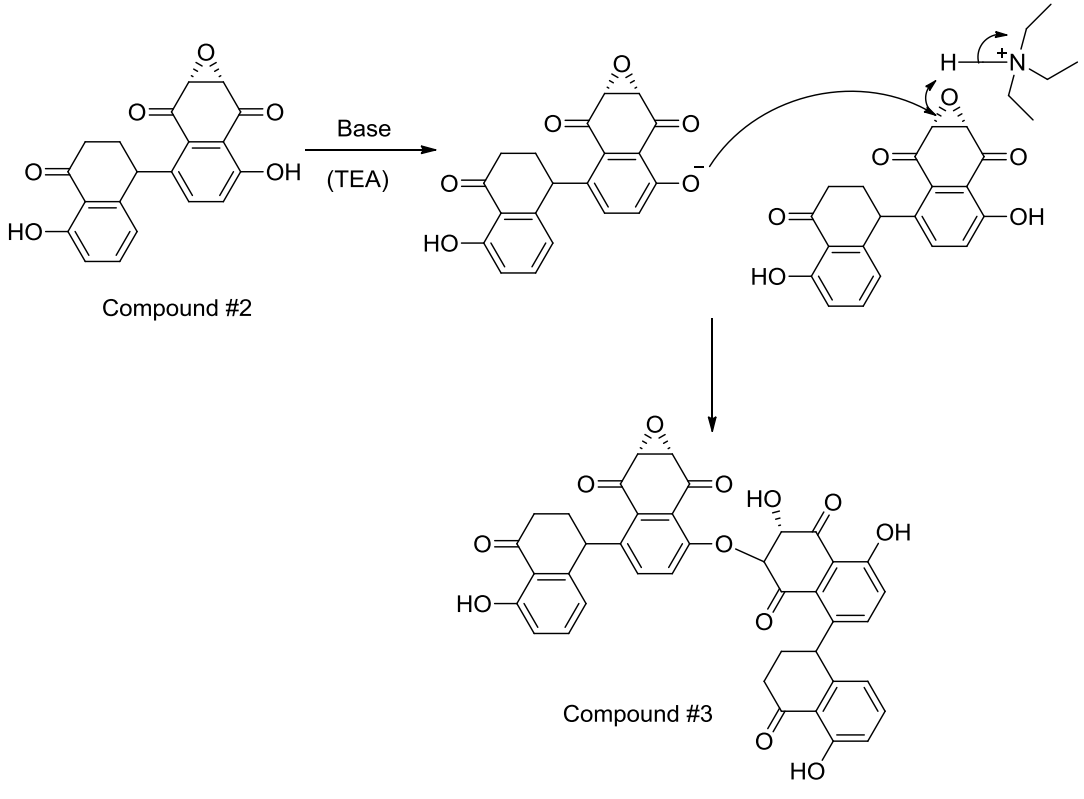

Fig. 7C

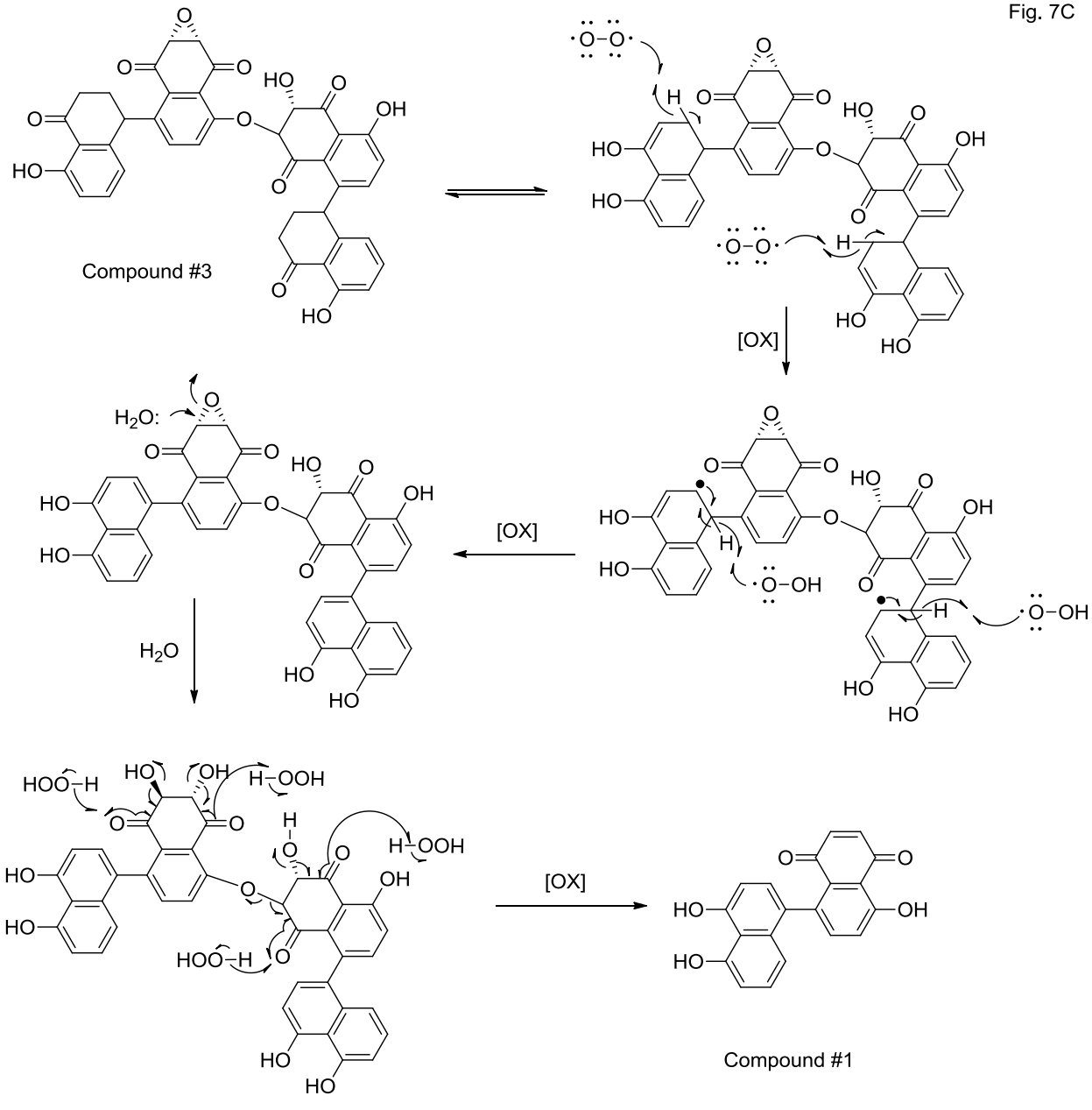

Fig. 7: Proposed alternol degradation mechanisms. (A) The formation of compound #2 (MW: 350); (B) The formation of compound #3 (MW: 700); (C) The formation of compound #1 (MW: 332).

6.5 Conclusions

Baseline separation of degraded alternol was achieved by a 0.1 % TEA modified mobile phases using a C18 column. At neutral and acidic conditions, the three mixtures were not fully separated. This indicated that pH adjustment played a key role in the alternol degraded compound mixture purification.

6.6 References

1. M.J. Wargovich, C. Woods, D.M. Hollis, and M.E. Zander. Herbals, cancer prevention and health. The Journal of nutrition. 131:3034S-3036S (2001).
2. J.W. Ho, Y.K. Leung, and C.P. Chan. Herbal medicine in the treatment of cancer. Current medicinal chemistry Anti-cancer agents. 2:209-214 (2002).
3. M.C. Wani, H.L. Taylor, M.E. Wall, P. Coggon, and A.T. McPhail. Plant antitumor agents. VI. The isolation and structure of taxol, a novel antileukemic and antitumor agent from Taxus brevifolia. Journal of the American Chemical Society. 93:2325-2327 (1971).
4. Z.Z. Liu, J.P. Chen, S.L. Zhao, and C.L. Li. [Apoptosis-inducing effect of alternol on mouse lymphocyte leukemia cells and its mechanism]. Yao xue xue bao = Acta pharmaceutica Sinica. 42:1259-1265 (2007).
5. X. Liu, J. Wang, B. Sun, Y. Zhang, J. Zhu, and C. Li. Cell growth inhibition, G2M cell cycle arrest, and apoptosis induced by the novel compound Alternol in human gastric carcinoma cell line MGC803. Investigational new drugs. 25:505-517 (2007).

6. E.D. Yeung, A. Morrison, D. Plumeri, J. Wang, C. Tong, X. Yan, and J. Li. Alternol exerts prostate-selective antitumor effects through modulations of the AMPK signaling pathway. The Prostate. 72:165-172 (2012).
7. Z.Z. Liu, J. Zhu, B. Sun, S. Liu, S. Geng, X. Liu, and C.L. Li. Alternol inhibits proliferation and induces apoptosis in mouse lymphocyte leukemia (L1210) cells. Molecular and cellular biochemistry. 306:115-122 (2007).
8. X.M. Liang, Y. Jin, Y.P. Wang, G.W. Jin, Q. Fu, and Y.S. Xiao. Qualitative and quantitative analysis in quality control of traditional Chinese medicines. Journal of chromatography A. 1216:2033-2044 (2009).
9. H.Y. Zhaoand J.G. Jiang. Application of chromatography technology in the separation of active components from nature derived drugs. Mini Rev Med Chem. 10:1223-1234 (2010).